

**UTILIZATION OF MASS SPECTROMETRY TO CHARACTERIZE,
IMAGE, AND QUANTIFY SMALL MOLECULES**

by
Hilary Brown

A Dissertation

*Submitted to the Faculty of Purdue University
In Partial Fulfillment of the Requirements for the degree of*

Doctor of Philosophy



Department of Chemistry
West Lafayette, Indiana
December 2019

**THE PURDUE UNIVERSITY GRADUATE SCHOOL
STATEMENT OF COMMITTEE APPROVAL**

Dr. Julia Laskin, Chair
Department of Chemistry

Dr. Hilikka Kenttämä
Department of Chemistry

Dr. Angeline Lyon
Department of Chemistry

Dr. Elizabeth Parkinson
Department of Chemistry

Approved by:
Dr. Christine A. Hrycyna

Dedicated to Kayla N. Holmberg, Kenny M. Stowers, T. Ann Hall, Margaret B. Stowers, Joan E. Brown, Robert W. Brown, Charlotte J. Drexler, and Dixie R. Brown

ACKNOWLEDGMENTS

The research detailed in *Chapter 2* was funded by NSF CHE-1308114 and NIH R01GM118484. The research described in *Chapter 3* was supported by grant U01 HL122703 from the National Heart Lung Blood Institute of NIH (LungMAP). The experimental work was performed in the Environmental Molecular Sciences Laboratory, a national scientific user facility sponsored by the U.S. Department of Energy and located at Pacific Northwest National Laboratory (PNNL) in Richland, WA. PNNL is a multi-program national laboratory operated by Battelle for the U.S. Department of Energy (DOE) under Contract DE-AC05-76RL01830. The research described in *Chapter 4* was supported by Merck & Co, Inc.

First, I would like to thank my family for supporting me through so many years of school and believing that I could finish. My father, Scott, and my mother, Cheryl, have provided unconditional support even though sometimes they have no idea what I am talking to them about. My sister, Michelle, and brother, Adam, always provide the laughs whether through FaceTime calls or the rare opportunities our schedules would align for family vacations. I would have also not made it through with my sanity if it wasn't for the truly unconditional love from my wonderful dog, Ms. Indy Windy.

Secondly, I want to thank all of my friends that have helped me through the toughest times and actually knew the day-to-day struggles that we went through to be here today. From all-nighters to crazy inside jokes from high school, my ride-or-dies from the beginning, thank you Dayrin Mendez, Shalomi Momin, Vaidehi Joshi, and the whole RMSST crew. We made it through high school and now we are all pursuing our dreams. Next up college! Florida was a great place for

undergrad and I met even more great people. Thank you, Jennifer Speer, Nikki Hannon, Robert Soares, and the UT chemistry crowd. We learned to love analytical chemistry from the best professors and did some pretty crazy research, lab minions forever. Now on to grad school. This is where the long hours, sleepless nights, and stressful days really maxed out, but the people I met made it all worth it. Thank you to the original crew, Patrick Fedick, Janny Dinh, Heather Siebert, Gary Prato, Samantha Ebner. Y'all left me too early but we all are going to make it out! And to my friends that I met later but it felt like we had been friends since the beginning, Ana Morales, Daniela Mesa Sanchez, Courtney Rupert, and Christopher West. Thank you to my Indiana family. You all were my home away from home. We celebrated the holidays together and you invited me into your lives, making Indiana feel like home. It's always nice to know the "townies" when moving to a new place. Thank you, Skyler Griffith, Alissa Fedick, Twila & Michael Smith, Amanda Haan & Josh Thomack, Rick & Dawn Haan, and Bentley Griffith.

Finally, thank you to all of my wonderful, supportive advisors that have taught me to be the independent scientist I am today. Dr. Kenyon Evans-Nguyen, thank you for showing me how fun research could be and encouraging me to apply to graduate school. Dr. Yu Xia, thank you for allowing me to join your research group and supporting me through the start of my graduate school career. Thank you, Dr. Julia Laskin, for accepting me into your group after a very turbulent third year and guiding me to the finish line!

TABLE OF CONTENTS

LIST OF TABLES	8
LIST OF FIGURES.....	9
LIST OF ABBREVIATIONS	12
ABSTRACT	14
CHAPTER 1. INTRODUCTION	17
1.1 Ambient Ionization	17
1.1.1 Nano Electrospray Ionization (nanoESI).....	17
1.1.2 Nanospray Desorption Electrospray Ionization (nano-DESI).....	18
1.2 Paternò-Büchi Reaction	19
1.3 Lipid Analysis.....	20
1.4 Lipid Extraction Methods	21
CHAPTER 2. UTILIZATION OF THE PATERNÒ-BÜCHI REACTION TO ANALYZE NEUTRAL LIPIDS BY MASS SPECTROMETRY	22
2.1 Abstract.....	22
2.2 Introduction.....	22
2.3 Experimental.....	25
2.3.1 Nomenclature.....	25
2.3.2 Materials	25
2.3.3 PB-MS ³ for TG analysis	26
2.4 Results and Discussion	26
2.4.1 Offline coupling of PB reaction and nanoESI for glycerolipid analysis	26
2.4.2 PB-MS/MS CID for MG and DG C=C location isomer analysis.....	28
2.4.3 PB-MS ³ CID for TG C=C location isomer analysis.....	29
2.4.4 Analysis of TG extract from human plasma.....	31
2.5 Conclusion	35
CHAPTER 3. UNDERSTANDING LIPID LOCALIZATION IN THE DEVELOPING LUNG USING NANO-DESI MASS SPECTROMETRY IMAGING.....	36
3.1 Abstract.....	36
3.2 Introduction.....	36
3.3 Experimental.....	38

3.3.1	Reagents.....	38
3.3.2	Tissue Collection and Handling	39
3.3.3	Lipidomics	40
3.3.4	Nano-DESI Imaging	40
3.3.5	Data Processing	41
3.4	Results and Discussion	41
3.5	Conclusion	50
CHAPTER 4. MASS SPECTROMETRY IMAGING OF DICLOFENAC AND ITS METABOLITES IN TISSUES USING NANO-DESI.....		51
4.1	Abstract.....	51
4.2	Introduction.....	51
4.3	Experimental.....	53
4.3.1	Reagents.....	53
4.3.2	Tissue Collection and Handling	53
4.3.3	LC-MS/MS	53
4.3.4	Nano-DESI Imaging	54
4.3.5	Data Processing	55
4.4	Results and Discussion	55
4.5	Conclusion	61
APPENDIX A. CHAPTER 3 SUPPLEMENTAL.....		63
APPENDIX B. CHAPTER 4 SUPPLEMENTAL		98
REFERENCES.....		102
VITA		112

LIST OF TABLES

Table 2.1 Structural Composition of abundant TAG species in Human Plasma extract	34
Table 2.2 continued: Structural Composition of abundant TAG species in Human Plasma extract	35
Table 4.1 Concentrations of diclofenac and its major metabolites in kidney (DK) and liver (DL) tissue from LC-MS/MS quantitative method. Dosed tissue samples (DK 4-6, DL 4-6) and control tissues (DL 1-3, DK 1-3) were ran in triplicate. Hydroxydiclofenac was not stable in kidney tissue homogenate and could not be accurately quantified but significant amount was observed (N/A). BLQ: Below limit of quantitation.	60

LIST OF FIGURES

Figure 1.1 NanoESI setup	17
Figure 1.2 Nano-DESI setup	18
Figure 1.3 General PB-reaction scheme ¹⁹	19
Figure 1.4 PB-MS3 CID strategy for the determination of C=C location within fatty acyl chains of MG/DG/TGs.....	19
Figure 2.1 Structural characteristics and nomenclature of triglycerides.....	23
Figure 2.2 Offline PB reaction of glycerolipid standards 5μM in 1:4:0.5 chloroform/methanol/water containing 1.11mM sodium acetate. NanoESI MS1 spectra before reaction in positive ion mode: (a) MG 18:1(9Z)/0:0/0:0, (b) DG 18:1(9Z)/18:1(9Z)/0:0, and (c) TG 18:1(9Z)/18:1(9Z)/18:1(9Z). NanoESI MS ¹ spectra after offline PB reaction in positive ion mode: (d) MG, (e) DG, and (f) TG. (g) Offline reaction setup with tephlon tubing and nanoESI setup. (h) Optimized reaction kinetics (reaction time 1.5 min). (i) PB reaction of TG 18:1/18:1/18:1 in nanoESI tip.....	27
Figure 2.3 CID spectra of MG 18:1(9Z)/0:0/0:0 sodium adduct (a) before reaction and (b) MG PB product after reaction. CID spectra of DG 18:1(9Z)/18:1(9Z)/0:0 sodium adduct (c) before reaction and (d) DG PB product after reaction. CID spectra of DG lithium adduct (e) before reaction and (f) DG PB product after reaction. CID spectra of DG ammonium adduct (g) before reaction and (h) DG PB product after reaction.	29
Figure 2.4 PB-MS ³ of TG 16:0/18:1(9Z)/18:2(9Z,12Z) 10 μM in 1:4:0.5 chloroform/methanol/water containing 1.11 mM sodium acetate. NanoESI MS1 spectra in positive mode: (a) before reaction and (b) after offline PB reaction. MS ² beam-type CID of (c) [TG+Na] ⁺ at m/z 879.7 and (d) the PB product [TG+Na+58] ⁺ at m/z 937.7. MS ³ CID of (e) [18:2+Na+58] ⁺ (m/z 363.2) and (f) [18:1+Na+58] ⁺ (m/z 363.2).	31
Figure 2.5 Structural identification of abundant unsaturated TG species from human plasma. MS1 profile of TG species in human plasma (a) before reaction and (b) after reaction. MS2 beam type CID of (c) m/z 939.7 and (d) m/z 911.7. MS ³ CID of (e) 939→[18:1+Na+58] ⁺ m/z 363.2, (f) 939→[18:2+Na+58] ⁺ m/z 361.2, (g) 911→[16:1+Na+58] ⁺ m/z 335.2, and (h) 911→[18:1+Na+58] ⁺ m/z 363.	33
Figure 3.1 a) Average positive mode nano-DESI mass spectra of lipid profiles from E18.5 (black trace shown as positive signal) and PND7 samples (red trace shown as negative signal). Profile represents an average spectrum over the entire tissue section with signal intensity normalized to the signal of the internal standard, LPC 19:0. b) Selected lipids labeled in 1a are identified in the table along with z-scores calculated from acquired lipidomics data. Enriched lipid species are represented by a positive z-score (red) whereas, a negative z-score (blue) indicates lipid depletion.	42
Figure 3.2 Optical and nano-DESI images of selected PC and PG species known to be abundant in pulmonary surfactant. These lipids are localized to alveoli across all three developmental stages. Specifically, for PC 34:1 in E18:5, this lipid is also located in the surrounding tissue, not just the	

lung. PC species were analyzed in positive mode as sodium adducts $[M+Na]^+$ and PG species were detected in negative mode as $[M-H]^-$. Scale bar indicates 1 mm. Intensity scale (0% black, 100% white) represents signal intensity of individual peaks normalized to the maximum value in each image. Positive mode ion images were normalized to LPC 19:0 and negative mode ion images were normalized to TIC..... 44

Figure 3.3 Optical and nano-DESI images of PC species from PND28 samples are arranged here by carbon number (C36 top row, C38 bottom row) and degree of unsaturation. Lipids with lower degrees of unsaturation have alveolar localization. Meanwhile, more unsaturated lipids localize around the airways and blood vessels of the lungs. Scale bar indicates 1 mm. Intensity scale (0% black, 100% white) represents signal intensity of individual peaks normalized to the maximum value in each image. Positive mode ion images were normalized to LPC 19:0. 46

Figure 3.4 Nano-DESI images showing that lipid localization also depends on the head group of the lipid species and lung developmental stage. PUFA-containing lipids with different head groups observed in PND7 and PND28 samples are compared in the figure. For PC species, localization around airways can be seen in both stages of development. Ion images of PI species in PND7 show some very faint bright spots indicating some localization to airways but the localization is far more prominent in PND28 samples. Other lipid classes are localized to alveoli. Several PS and PG species were observed with very low abundance. Scale bar indicates 1 mm. Intensity scale (0% black, 100% white) represents signal intensity of individual peaks normalized to the maximum value in each image. Positive mode ion images were normalized to LPC 19:0 and negative mode ion images were normalized to TIC. 48

Figure 3.5 Other lipid species that were analyzed were MG, LPC, and FA. PND7 and PND28 samples were compared and biologically relevant lipid chains were selected. For MG and FA lipids in both developmental stages the lipids are alveolar localized regardless of degree of unsaturation. LPC species, however follow the PC trend seen earlier. LPC lipids with a higher degree of unsaturation localize around airways whereas lower degrees of unsaturation, the lipids are alveolar localized. Scale bar indicates 1 mm. Intensity scale (0% black, 100% white) represents signal intensity of individual peaks normalized to the maximum value in each image. Positive mode ion images were normalized to LPC 19:0 and negative mode ion images were normalized to TIC. . 50

Figure 4.1 (A) Schematic drawing of the nano-DESI system positioned in front of a mass spectrometer inlet showing the nano-DESI probe comprised of two fused silica capillaries for solvent delivery and ESI, and a shear force capillary for maintaining constant distance between the sample and probe. (B) Negative ion mode mass spectrum of diclofenac dosed mouse kidney tissue in the m/z 150-500 range. (C) Expanded view of the m/z 290-315 range. Diclofenac (red, m/z 294), diclofenac-d4 (green, m/z 298), 4'- and 5-hydroxydiclofenac (blue, m/z 310) are present. The inset structure corresponds to diclofenac (red) with additional modifications for 4'-hydroxydiclofenac (blue, 4' carbon -OH group) and 5-hydroxydiclofenac (black, 5 carbon -OH group). (D) Expanded view of the m/z 460-480 range. The structure of the acyl glucuronide metabolite (red, m/z 470) is shown in inset..... 56

Figure 4.2 H&E, optical, and nano-DESI ion images of diclofenac dosed mouse kidney tissue. Relevant regions of H&E stained kidney section are annotated for comparison with ion images. Ion images of diclofenac (D), acyl glucuronide (AG), and hydroxydiclofenac (HD) are shown for both left and right kidney to demonstrate the reproducibility of nano-DESI MSI. Ion images are self-normalized to the internal standard, diclofenac-d4. Scale bar represents 1 mm. Intensity scale ranges from 0% intensity (black) to 100% (white). 58

Figure 4.3 Optical and nano-DESI ion images of diclofenac dosed mouse liver tissue. Ion images of diclofenac (D), acyl glucuronide (AG), and hydroxydiclofenac (HD) are shown for two different liver sections. Ion images are self-normalized to internal standard, diclofenac-d4. Scale bar represents 1 mm. Intensity scale ranges from 0% intensity (black) to 100% (white)..... 59

Figure 4.4 Optical and nano-DESI SIM mode ion images of dosed kidney and liver tissue. Ion images of diclofenac (D; center m/z 294, width 10), acyl glucuronide (AG; center m/z 470, width 10), and hydroxydiclofenac (HD; center m/z 310, width 10) were collected using SIM windows centered on respective m/z values. Ion images are self-normalized. Scale bar represents 1 mm. Intensity scale ranges from 0% intensity (black) to 100% (white). 61

LIST OF ABBREVIATIONS

C=C	<u>C</u> arbon- <u>C</u> arbon double bond
CE	<u>C</u> holesterol <u>E</u> ster
Cer	<u>C</u> eramide
CID	<u>C</u> ollisional <u>I</u> nduced <u>D</u> issociation
CMC	<u>C</u> arboxy <u>m</u> ethyl <u>c</u> ellulose
Da	<u>D</u> alton
DAG or DG	<u>D</u> iacylglycerol
DPPC	<u>D</u> ipalmitoyl <u>P</u> hosphatidyl <u>ch</u> oline
E	<u>E</u> mbryonic
EID	<u>E</u> lectron <u>I</u> nduced <u>D</u> issociation
ESI	<u>E</u> lectrospray <u>I</u> onization
FA	<u>F</u> atty <u>A</u> cid
GalCer	<u>G</u> alactosyl <u>c</u> eramide
GC	<u>G</u> as <u>C</u> hromatography
GL	<u>G</u> lycerol <u>i</u> pid
HCD	<u>H</u> igher-energy <u>C</u> ollision <u>D</u> issociation
HPLC	<u>H</u> igh <u>P</u> ressure <u>L</u> iquid <u>C</u> hromatography
LC	<u>L</u> iquid <u>C</u> hromatography
LIQUID	<u>L</u> ipid <u>I</u> nformed <u>Q</u> uantitation and <u>I</u> dentification
LPC	<u>L</u> ysophosphatidyl <u>ch</u> oline
MAG or MG	<u>M</u> onoacylglycerol
MALDI	<u>M</u> atrix <u>A</u> ssisted <u>L</u> aser <u>D</u> esorption <u>I</u> onization
MRM	<u>M</u> ultiple <u>R</u> eaction <u>M</u> onitoring
MS	<u>M</u> ass <u>S</u> pectrometry

MS ² or MS/MS	Tandem <u>M</u> ass <u>S</u> pectrometry
MSI	<u>M</u> ass <u>S</u> pectrometry <u>I</u> maging
Nano-DESI	<u>N</u> anospray <u>D</u> esorption <u>E</u> lectrospray <u>I</u> onization
nanoESI	<u>N</u> ano <u>E</u> lectrospray <u>I</u> onization
PB	<u>P</u> aternò- <u>B</u> üchi
PC	<u>P</u> hosphatidyl <u>ch</u> oline
PE	<u>P</u> hosphatidyl <u>e</u> thanolamine
PG	<u>P</u> hosphatidyl <u>g</u> lycerol
PI	<u>P</u> hosphatidyl <u>i</u> nositol
PND	<u>P</u> ostnatal <u>D</u> ay
PS	<u>P</u> hosphatidyl <u>s</u> erine
PUFA	<u>P</u> oly- <u>u</u> nsaturated <u>F</u> atty <u>A</u> cid
QWBA	Quantitative Whole-Body Autoradiography
SM	<u>S</u> phingom <u>y</u> elin
SPE	<u>S</u> olid <u>P</u> hase <u>E</u> xtraction
TAG or TG	<u>T</u> riacyl <u>g</u> lycerol
TIC	<u>T</u> otal <u>I</u> on <u>C</u> urrent
UGT	<u>U</u> ridine Diphosphate <u>G</u> lucuronosyl <u>T</u> ransferase
UPLC	<u>U</u> ltra High- <u>P</u> erformance <u>L</u> iquid <u>C</u> hromatography
Δ	Delta (double bond position)

ABSTRACT

Ambient ionization techniques, such as nanoDESI and nanoESI, allow for the direct analysis of complex samples under atmospheric pressure with no sample pretreatment. These ionization techniques are utilized for a variety of applications, including lipidomics, online reactions and imaging of small molecules. Nanoelectrospray ionization (nanoESI) is an ionization technique that is similar to electrospray ionization (ESI) but uses smaller sample volumes. NanoESI can be used for complex biological sample analysis and when coupled with online photochemical reactions, such as the Paternò-Büchi (PB) reaction, structural information about lipids can be determined. Likewise, nanoDESI is another ambient ionization technique that employs the ESI mechanism but incorporates online liquid extraction of analytes. This technique is easily incorporated to mass spectrometry imaging (MSI) to provide spatial localization of biomolecules in tissues. Additionally, nanoDESI allows for tunable solvent extraction and online derivatization reactions. These techniques were used to determine structural information of neutral lipids, to image lipids from different developmental stages of lung tissue, and to image and quantify small molecule drugs and metabolites in tissue.

Chapter 2: Utilizing the Paternò-Büchi Reaction to Analyze Neutral Lipids by Mass Spectrometry

Glycerolipids (GLs), such as mono-, di- and tri-substituted glycerols, are biologically important due to their role in long term energy storage in mammalian tissues. GLs are commonly analyzed using electrospray ionization (ESI) after the formation of an adduct ion, $[M+\text{adduct}]^+$. Currently, ESI-tandem mass spectrometry (MS/MS) allows determination of acyl chain information including carbon number and degree of unsaturation. However, the exact location of a carbon-carbon double bond (C=C) is difficult to obtain from low energy collisional-induced dissociation (CID). In this work, the PB reaction coupled with nanoESI-MS³ method was developed to determine structural information of unsaturated GLs from human plasma. The PB reaction involves a ketone being activated under UV light to attach to a structure containing a double bond to form a stable product. Specifically, this reaction was used to determine double bond location in lipids, where the PB product formed is the lipid species plus acetone. CID of the reaction product leads to typical glycerolipid fragmentation corresponding to the loss of each individual acyl chain. CID also reveals unique fragment ions that correspond to each unsaturated fatty acyl chain plus

sodium and acetone $[FA+Na+58]^+$. This fragment peak can be isolated in MS³ and fragmented again to form the diagnostic ion pairs that indicated the double bond position.

Chapter 3: Understanding Lipid Localization in the Developing Lung using Nano-DESI Mass Spectrometry Imaging

Mouse lung development occurs in four stages from embryonic (E) day 9.5 to postnatal day (PND) 30. Pulmonary surfactant, composed mainly of lipids, is produced in the lungs by type II alveolar cells to help reduce surface tension during breathing. Phosphatidylcholines are the most common lipids in lung surfactant (70-80%) with PC(16:0/16:0) being the dominant species. Understanding the localization and role of lipids in different stages of lung development provides important insights into normal lung progression. Identification of lipids in tissues can be obtained using a standard lipid extraction method coupled with LC-MS/MS; MSI provides additional information on their localization within the tissue sample. Herein, nanoDESI-MSI was used for label-free imaging of lipids in both embryonic and postnatal mouse lung tissues. The images produced from nanoDESI-MSI experiments are compared with optical images and H&E stained images to identify lung structures (e.g. airways, bronchi, alveolar regions, etc). Embryonic stage lipids are typically shorter chain species either saturated or with a low degree of unsaturation. These lipids are mostly consistent with highly abundant surfactant lipids. In addition to surfactant lipids, the postnatal lung samples (PND7&28) contained longer chain lipids (e.g.C20) with higher degree of unsaturation and larger head group diversity. Lipids that are more unsaturated (e.g. PC36:4 and PC38:6) tend to localize around airways, as compared to lipids that are saturated or have a lesser degree of unsaturation. Embryonic lung tissue shows no localization since surfactant lipids are the most prevalent species. As the lung matures, lipids with more diversity (head group, chain length, degree of unsaturation) begin to localize and play more important roles in lung's response to inflammation and as precursors to lipid mediators.

Chapter 4: Quantitative Mass Spectrometry Imaging of Diclofenac and its Metabolites in Tissues Using Nanospray Desorption Electrospray Ionization Mass Spectrometry

Diclofenac is a widely used nonsteroidal anti-inflammatory drug (NSAID). It is most commonly taken orally for pain, migraines, and arthritis. Glucuronidation is a common metabolic process for drugs and xenobiotics to increase their solubility for excretion. Acyl-glucuronides (glucuronides of carboxylic acids) present concerns of toxicity as they have been implicated in drug-induced

hypersensitivity and hepatic failure. Glucuronides can be analyzed using soft ionization mass spectrometry techniques by a neutral loss of 176 corresponding to the loss of the sugar moiety. Identification and quantification of drugs and their metabolites in tissues can be obtained using LC-MS/MS, however, MSI provides additional information about their localization within the tissue sections. NanoDESI-MSI was used for imaging of diclofenac and its major metabolites, acyl-glucuronide and hydroxydiclofenac, in both liver and kidney tissues. NanoDESI allows for label-free imaging with high spatial resolution but offers the advantage of no sample pre-treatment and shotgun-like quantification. Quantitation capabilities of nanoDESI were evaluated using both a mimetic tissue model and inclusion of internal standards in the spray solvent. Tissue sections from the liver and kidney of diclofenac-dosed mice were obtained from Merck. Using nanoDESI-MSI, ion images for diclofenac and its major metabolites were produced. The acyl-glucuronide is localized to the inner medulla and hydroxydiclofenac is localized to the cortex. These distributions observed for both metabolites are consistent with the body's normal metabolism and preparing the drug for excretion.

CHAPTER 1. INTRODUCTION

1.1 Ambient Ionization

Ambient ionization is a technique that allows ions to be created outside the mass spectrometer (MS) under ambient conditions. Samples can be analyzed in their original state with minimal sample preparation.¹⁻⁷ This idea started with Desorption Electrospray Ionization (DESI) from the Cooks group at Purdue in 2004 and was followed shortly by Direct Analysis in Real Time (DART).¹⁻³ Ambient ionization techniques can be divided into Direct Analysis and Pure Ambient techniques. Where direct analysis techniques, such as nanoESI, usually require some offline sample preparation. For pure ambient, such as DESI and nano-DESI, samples are directly analyzed with no sample pretreatment. Pure ambient ionization techniques can be further divided into liquid extraction, thermal desorption, and laser ablation techniques.^{3,8}

1.1.1 Nano Electrospray Ionization (nanoESI)

Nano Electrospray Ionization or nanoESI is an ambient ionization technique that mimics ESI but on a smaller scale. Glass or quartz capillaries are pulled to a fine tip, roughly on the order of 1 μm .⁹ A tip puller is used to pull capillaries to the desired width.¹⁰ Voltage is then applied to a conductive wire inserted into the solution to create the electrospray.^{9,10} The tip is placed in front of the MS inlet, approximately 0.5 – 2 mm away.¹⁰ Figure 1.1 shows an example of a typical nanoESI setup. One advantage of nanoESI is that smaller sample volumes (1-2 μL) are used compared to ESI.^{9,10} Of particular interest for this thesis, nanoESI was used to ionize lipid solutions and couple with photochemical reactions to allow for structural elucidation. The borosilicate glass capillary used as the nanoESI emitter is UV transparent and allowed the UV light to pass through to react with the lipids in solution.

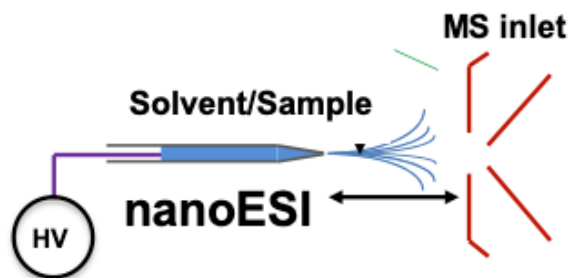


Figure 1.1 NanoESI setup

1.1.2 Nanospray Desorption Electrospray Ionization (nano-DESI)

Nanospray Desorption Electrospray Ionization or nano-DESI is an ambient ionization technique that is characterized as a direct liquid extraction method.¹¹ Nano-DESI is comprised of two fused silica capillaries that align to form a liquid bridge of solvent on a sample surface. The primary capillary supplies solvent to the liquid bridge and the secondary transports solvent and extracted analytes to the mass spectrometer.¹² This allows for continuous liquid extraction and simultaneous ionization of analyte molecules.¹¹ The typical nano-DESI setup is shown in Figure 1.2. The solvent applied to the sample is typically 9:1 MeOH/H₂O but can be adjusted for better extraction. Internal standards can also be added for “shotgun-like” quantitation.^{13,14} One major application of nano-DESI is mass spectrometry imaging (MSI). No sample preparation is needed for nano-DESI, therefore, tissue sections can be imaged directly.¹⁵ With pulled capillaries, nanoDESI can achieve a spatial resolution of 10 μm . A third pulled capillary, known as the shear force probe, can be added to the setup to allow for the distance between the probe and the sample to remain constant.^{16,17}

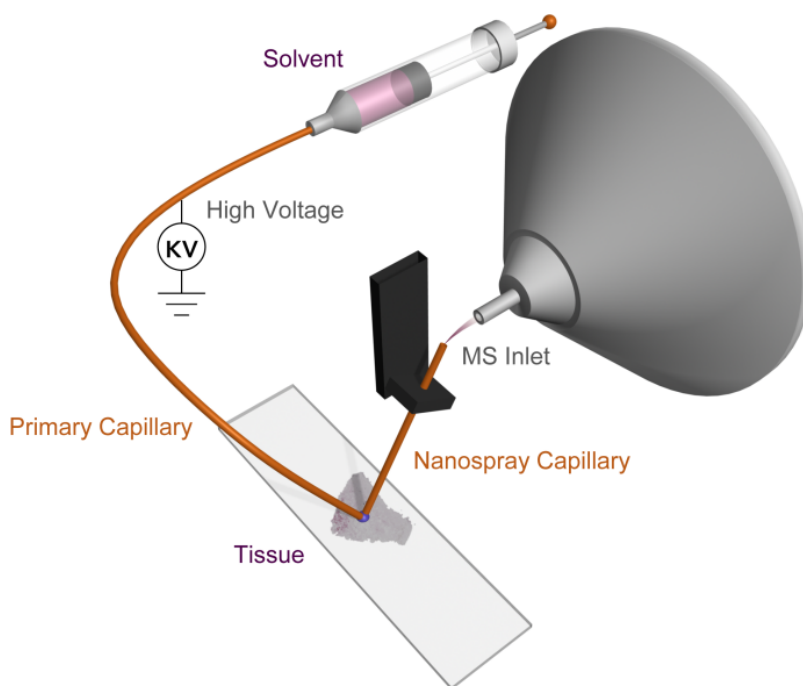


Figure 1.2 Nano-DESI setup

1.2 Paternò-Büchi Reaction

The Paternò-Büchi (PB) reaction is a photo-induced [2+2] cycloaddition of unsaturated compounds. A four-membered cyclic ether or oxetane ring is formed. Briefly, the carbonyl compound (acetone) is irradiated (254 nm UV lamp) and electronically excited. The excited carbonyl group then attacks the carbon-carbon double bond and the cycloaddition occurs.¹⁸ Previous work from the Xia group has detailed the development of the PB-reaction method and demonstrated its application toward pinpointing double bond locations of unsaturated fatty acids¹⁹ and lipid double bond location isomers.²⁰ Figure 1.3 shows a general reaction scheme for the PB-reaction. Figure 1.4 shows the PB reaction scheme specifically for a TAG molecule.

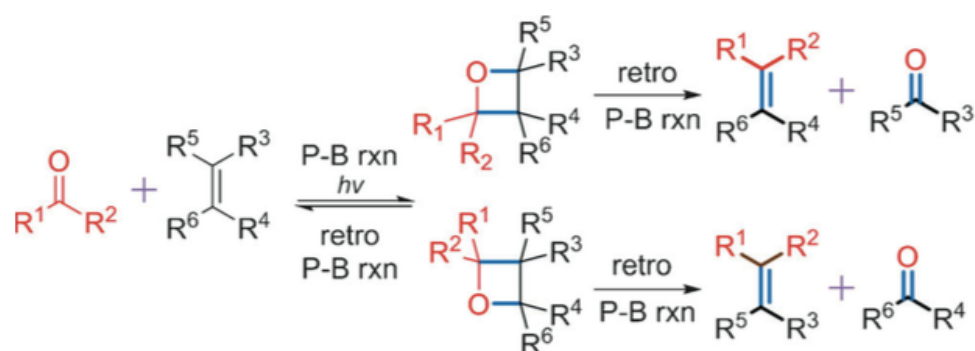


Figure 1.3 General PB-reaction scheme¹⁹

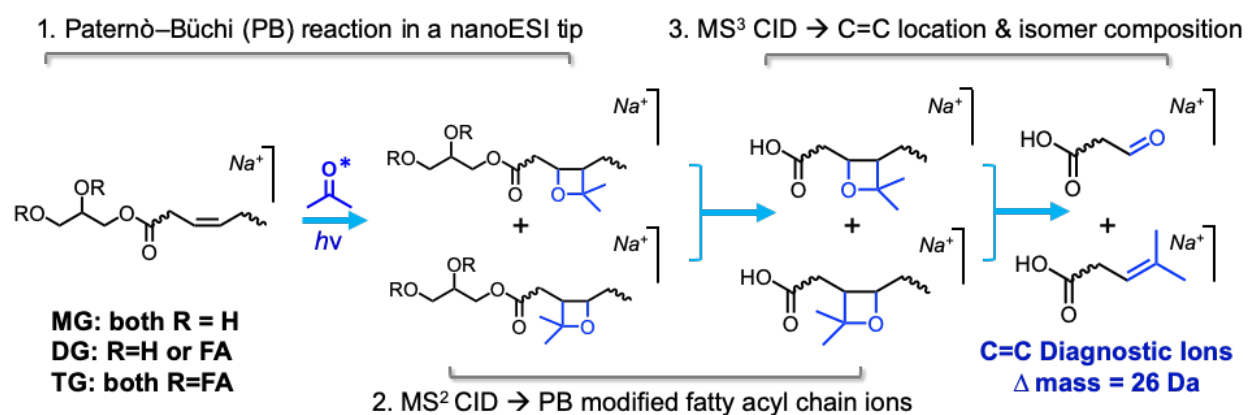


Figure 1.4 PB-MS³ CID strategy for the determination of C=C location within fatty acyl chains of MG/DG/TGs

1.3 Lipid Analysis

Lipidomics is the study of the cellular lipidome by identifying the lipid species present in the lipid profile and investigating the dynamic changes in lipid composition from certain disease states.²¹⁻

²³ Lipidomic studies focus on five areas including (1) identification of new lipid classes, (2) quantitative methods for lipid analysis in biological samples, (3) lipid pathway and biomarker analysis for diagnostics, (4) tissue imaging of altered lipid distribution, and (5) bioinformatics approaches for automated and high-throughput lipid analysis.²¹

Lipids can be analyzed for identification and quantitation by a variety of analytical methods including thin layer chromatography, gas chromatography, liquid chromatography, nuclear magnetic resonance, and mass spectrometry (MS). Of these techniques, mass spectrometry is most widely used because of its advanced capabilities including high sensitivity, specificity, throughput and accuracy.²³ A mass spectrometer has three essential components: (1) an ionization source, (2) a mass analyzer, and (3) a detector.²⁴

Electrospray Ionization (ESI) is the most widely used ionization source in lipidomics^{22,24} most likely due to the availability of ESI with commercial instruments, and ESI has a higher ionization efficiency for lipids compared to other traditional ion sources.²⁵ ESI is a “soft” ionization technique that provides a protonated ion $[M+H]^+$ or an adduct ion $[M+adduct]^+$, with little or no fragmentation from the ionization process.^{22,24,25} The term “shotgun” lipidomics refers to the direct infusion of crude lipid sample into the MS compared to LC-MS lipidomics which is the infusion of lipid sample after LC separation.^{21,22} A major advantage of shotgun lipidomics is the continuous spray of constant lipid concentration. This allows researchers time to optimize signal and MS parameters and perform tandem MS experiments.²¹ The shotgun approach has is an easy and fast way to assess a lipid profile but can often cause ion suppression and bias towards more abundant and more easily ionized lipids.²² Typically, a chromatographic separation is utilized to help separate lipid classes, reduce ion suppression, and increase sensitivity.²²

A variety of mass analyzers (quadrupole, ion trap, time of flight, orbitrap) can be used for lipid analysis. Each one has their own advantages and disadvantages. Triple quadrupole mass analyzers are popular due to their versatility in tandem MS experiments. A variety of detection modes can be utilized to help characterize lipids such as precursors ion scan and neutral loss scan.^{21,23,24} A

triple quadrupole mass analyzer provides high selectivity, sensitivity, and accuracy when using the tandem MS modes. Ion trap mass analyzers allow for multiple stages of tandem mass spec (MSⁿ).²⁴

1.4 Lipid Extraction Methods

In order to analyze lipids from biological samples (cells, tissue, biological fluids), a lipid extraction is usually performed.²³ Organic solvent extractions are typically used and the extraction process relies heavily on the solubility of lipids in the particular solvent used. Alkane solvents are typically more well-suited for the extraction of non-polar lipids such as TAGs.²²

The Folch method is the most commonly used total lipid extraction method. This method uses a 2:1 ratio of chloroform and methanol as an extraction solvent. The Folch method has the highest reported extraction efficiency compared to other extraction methods. Another widely used extraction method is a modified Folch method known as the Bligh and Dyer method. This method incorporates water into the extraction solvent mixture. Comparing the two methods, Folch is better for extracting lipids from solid tissues, whereas, the Bligh and Dyer method is better for biological fluids.²²

The Folch and Bligh/Dyer methods both use varying ratios of chloroform as the extraction solvent which will result in the organic layer being on bottom of the extraction mixture due the high density of chloroform. This can make collecting the lipid-containing organic layer difficult. Another extraction method that can be utilized is the MTBE method. Methyl tert-butyl ether (MTBE) and methanol are used as an extraction solvent. MTBE has a low density resulting in the organic layer being the top layer of the extraction mixture. The advantage of the lipid-containing layer being on top is that non-lipid components of the sample can now be removed from the collection layer by centrifugation. The MTBE method yields similar extraction recoveries when compared to the Folch and Bligh/Dyer methods.²²

Solid Phase Extraction (SPE) protocols can also be used to separate lipid classes after a total lipid extraction protocol described above has been performed. Solid phase extraction columns are similar to liquid chromatography columns.²²

CHAPTER 2. UTILIZATION OF THE PATERNÒ-BÜCHI REACTION TO ANALYZE NEUTRAL LIPIDS BY MASS SPECTROMETRY

2.1 Abstract

Glycerolipids (GLs), such as mono-, di- and tri-substituted glycerols, are biologically important due to their role in long term energy storage in mammalian tissues. GLs are commonly analyzed using electrospray ionization (ESI) after the formation of an adduct ion, $[M+\text{adduct}]^+$. Currently, ESI-tandem mass spectrometry (MS/MS) allows determination of acyl chain information including carbon number and degree of unsaturation. However, the exact location of a carbon-carbon double bond (C=C) is difficult to obtain from low energy collisional-induced dissociation (CID). In this work, an offline PB reaction coupled with nanoESI-PB-MS³ method was developed to determine structural information of unsaturated GLs from human plasma. CID of the reaction product leads to a predictable glycerolipid fragmentation, such as the loss of each individual acyl chain. CID also reveals product ions that correspond to the free acyl chain that was lost from the glycerolipid species plus sodium and acetone. For example, when TG 18:1/18:1/18:1 is analyzed, a peak corresponding to $[18:1+\text{Na}+58]^+$ is observed. This peak can then be isolated and further CID (MS³) reveals diagnostic ions that can then be used to determine C=C location of the acyl chain being lost. After development, this method was applied to TG extract from human plasma. Double bond locations were determined for 16:1, 18:1, 18:2 and 20:4 fatty acyl species. C=C location isomers were identified in TGs containing fatty acyl 18:1 with C=C at $\Delta 9$ and 11 positions.

2.2 Introduction

Triacylglycerols (TAG, TG) are glycerolipids that consist of three fatty acyl chains esterified to a glycerol backbone.²⁶ For TAG identification, TAG molecules contain several structural characteristics that need to be considered. The overall molecule has a specific molecular weight, total number of carbons, and degree of unsaturation; the glycerol backbone contains a chiral location indicating a *sn*- position; and the fatty acyl chains that are attached to the backbone can be inherently different as well with varying lengths, double bond location, and position of attachment to the glycerol backbone.²⁷ Figure 2.1 shows the variety of structural characteristics.

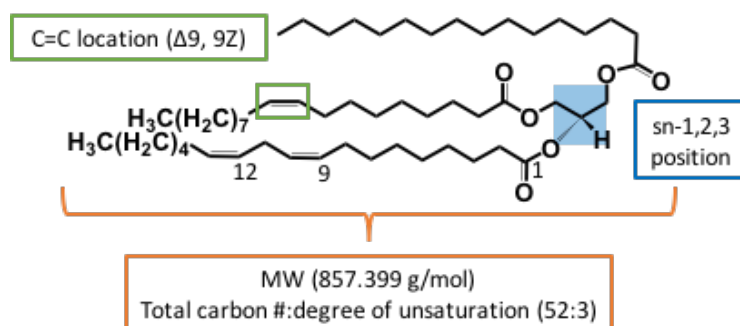


Figure 2.1 Structural characteristics and nomenclature of triglycerides.

Triacylglycerols are present in all cells but in varying amounts. TAGs are used as an energy source and energy storage system.^{26,28,29} Adipocytes contain the largest quantity of TAGs because adipocytes are specialized cells dedicated to the storage of TAGs.²⁶ Due to their nonpolar nature, TAGs are stored in lipoproteins (chylomicrons, very low-density lipoproteins, and low-density lipoproteins) when they are being transported throughout the body.^{26,28,29} TAGs, along with cholesterol esters, are some of the most abundant lipids in the blood present in mM concentrations.^{29,30}

Triacylglycerol molecules are also precursors for phospholipid biosynthesis. TAGs can be hydrolyzed to form diacylglycerol (DAG) and a free fatty acid. DAG molecules are then precursors for synthesizing other major phospholipids. The resulting DAG molecule can be further modified through phosphorylation to form phosphatidic acid, a precursor for even more lipid species.²⁸ Lipidomics is the study of the cellular lipidome by identifying the lipid species present in the lipid profile and investigating the dynamic changes in lipid composition from certain disease states.^{21–23} Lipids can be analyzed for identification and quantitation by a variety of analytical methods including thin layer chromatography, gas chromatography, liquid chromatography, nuclear magnetic resonance, and mass spectrometry (MS). Of these techniques, mass spectrometry is most widely used because of its advanced capabilities including high sensitivity, specificity, throughput and accuracy.²³ Previously, GC-MS was used to analyze TG species after being converted to fatty acid methyl esters. Using GC-MS as an analysis method can provide some structural information including: carbon number, MW, fatty acyl composition, degree of unsaturation, and double bond location. It does not provide information about how the acyl chains are attached to the glycerol backbone as an intact TAG molecule.²⁹

ESI can also be used to analyze TG species, but due to their nonpolar nature, ammonium or alkali-metal solutions need to be added into the spray solvent to form adduct ions with triacylglycerol. The most commonly used adduct ions are NH_4^+ , Na^+ and Li^+ .²⁴ Low energy CID activation of the $[\text{TG} + \text{NH}_4]^+$ adduct ion results in an $[\text{M} + \text{H}]^+$ peak from the loss of ammonia, and three prominent peaks $[\text{M} - \text{FA} + \text{NH}_3]^+$ resulting from the loss of individual acyl chains (if all fatty acid chains are different).³¹ If higher energy CID or another stage of tandem MS is used, then monoacylglycerol ions can be observed and carbon-carbon double bond cleavage can occur. Double-bond location cannot be ascertained from the double bond cleavage due to the migration of the double bond upon fragmentation.²⁴ Lithium adduct fragmentation shows more promise in revealing more structural information. Upon activation of the $[\text{TG} + \text{Li}]^+$ ion, diacylglycerol ions form resulting from the loss of one fatty acyl chain. Further activation reveals ions corresponding to $[\text{FA} + \text{Li}]^+$.³² A similar fragmentation pattern can be seen when using the sodium adduct.

Fragmentation patterns for both lithium³²⁻³⁴ and ammonium^{35,36} TG adducts have been well documented. Hsu and Turk have also reported a mechanism for the CID fragmentation pathway of the TG sodium adduct.³⁴ Blanksby and coworkers have determined TG double bond location isomers in standards using ozone induced dissociation (OzID).^{37,38} They have also combined sequential CID and OzID to determine *sn*- position of acyl chains esterified to the glycerol backbone.³⁹

The Paternò-Büchi (PB) reaction is a photo-induced [2+2] cycloaddition of unsaturated compounds. A four-membered cyclic ether or oxetane ring is formed. Briefly, the carbonyl compound (acetone) is irradiated (254 nm UV lamp) and electronically excited. The excited carbonyl group then attacks the carbon-carbon double bond and the cycloaddition occurs.¹⁸ Previous work from the Xia group has detailed the development of the PB-reaction method and demonstrated its application toward pinpointing double bond locations of unsaturated fatty acids¹⁹ lipid double bond location isomers²⁰ and cholesterol esters.⁴⁰

2.3 Experimental

2.3.1 Nomenclature

Lipid Maps defines glycerolipids as lipids that can only be hydrolyzed into glycerol, fatty acids, a sugar group, and/or alkyl variants. This includes mono-, di-, and triacylglycerols.⁴¹ Shorthand notation used for MGs, DGs, and TGs is outlined by Lipid Maps.⁴² For example, TG 16:0/18:1(9Z)/18:2(9Z,12Z) is shorthand for the triacylglycerol species that has three different fatty acyl chains 16:0, 18:1, and 18:2, denoting 16 or 18 carbons and 0, 1, or 2 degrees of unsaturation. The location of the double bond is in parentheses at position 9 for 18:1 and positions 9 and 12 for 18:2. The *cis*- or *trans* configuration of the double bond is denoted by the letter Z (*cis*) or E (*trans*). For standards, the *sn*- position is known so a / separator is used. If the *sn*- position is unknown, then a “_” separator is used.

2.3.2 Materials

Monolein (MG 18:1(9Z)/0:0/0:0) and TG 16:0/18:1/18:2 standards were purchased from Sigma Aldrich (St. Louis, MO). Di- and triacylglycerol standards, including DG 16:1(9Z)/16:1(9Z)/0:0, 18:1(9Z)/18:1(9Z)/0:0, 18:2(9Z,12Z)/18:2(9Z,12Z)/0:0, TG 16:1(9Z)/16:1(9Z)/16:1(9Z), 18:1(9Z)/18:1(9Z)/18:1(9Z), and 18:2(9Z,12Z)/18:2(9Z,12Z)/18:2(9Z,12Z), were obtained from Nu-Chek Prep (Elysian, MN). Standards were dissolved in chloroform and stored in -20°C freezer. Pooled human plasma (Lithium heparin anticoagulant) was obtained from Innovative Research Inc. (Novi, MI). Organic solvents were LC grade and DI-water was obtained from a water purification system at 0.03 μS cm.

A modified Folch method was used for total lipid extraction followed by a solid phase extraction (SPE) protocol for TG separation.⁴³ Briefly, plasma (100 μL) was added to 3 mL of 2:1 CHCl₃/MeOH and shaken for 2 minutes. The sample was then centrifuged (2000g, 10 min). Distilled water (750 μL) was added to the mixture. The sample was centrifuged again. The bottom chloroform layer was transferred to another tube and evaporated to dryness. The SPE protocol used the dried total lipid extraction from above. An Isolute SPE aminopropyl silica column (Biotage, Charlotte, NC) was conditioned with 0.6 mL of 7:1 acetone-water then washed with 2x1mL portions of hexane. The dried total lipid extract is reconstituted in 200 μL of 100:3:0.3 hexane/MTBE/acetic acid and applied to the column. Cholesterol esters are released from the

column first using 1 mL of hexane. TGs are eluted from the column using 100:5:5 hexane/CHCl₃/ethyl acetate. The TG fraction is collected, dried under N₂, and reconstituted in the spray solvent 1:4:0.5 CHCl₃/MeOH/H₂O (Na⁺, 1.11mM).

2.3.3 PB-MS³ for TG analysis

All experiments were performed on a 4000 Qtrap mass spectrometer (Sciex; Toronto, Canada), a triple quadrupole/linear ion trap hybrid MS in positive mode, equipped with a home-built nano electrospray ionization (nanoESI) source. A low-pressure mercury lamp (254 nm) from BHK Inc. (Ontario, Canada) was used to initiate the PB-reaction in an offline setup depicted in Figure 2.2(g). MG, DG, and TG (5-10 μM) standards were dissolved in 50:50 Acetone/Dichloromethane reaction solution. The reaction solution was pumped through 7.5cm of Teflon tubing (ID 0.02in) at 10.13 μL/min while being irradiated by UV light to initiate the PB reaction. The solution was collected then dried under N₂ and reconstituted in the spray solvent 1:4:0.5 CHCl₃/MeOH/H₂O (Na⁺, 1.11mM). MS² beam-type CID and MS³ CID were utilized for MG, DG, and TG analysis. The MS parameters used for this experiment include: spray voltage 1600V, curtain gas 0 psi, and declustering potential 20V. Analyst 1.5 was used for data collection, processing, and instrument control.

2.4 Results and Discussion

2.4.1 Offline coupling of PB reaction and nanoESI for glycerolipid analysis

An offline reaction setup using a syringe pump and Teflon tubing coiled around a UV lamp was used to initiate the PB reaction of a TG standard dissolved in 50:50 acetone/dichloromethane. This was found to be an ideal solvent condition for the offline reaction; DCM to dissolve the TG species and acetone as the ketone for the reaction. The reaction solution flowed through the tubing and was allowed to react for 1.5 minutes. After collection of the PB product, the reaction solution was dried and reconstituted in 1:4:0.5 chloroform/methanol/water (1.11mM Na⁺) spray solution. The spray solution was adapted from the ideal spray condition for TG ionization.^{32,34} Figure 2.2(g) shows the setup for the offline reaction.

MG, DG, and TG standards (5 μ M) were sprayed in MS¹ positive mode. The MG, DG, and TG sodium adduct peaks can be seen in Figure 2.2 (a), (b), and (c) respectively. The MS¹ spectra of the MG, DG, and TG standards after the PB reaction can be seen in Figure 2.2 (d), (e), and (f) respectively. The PB product is the addition of acetone (+58 Da) to the sodium adduct. The amount of product formed using the offline reaction is drastically increased compared to the amount of product formed when performing the PB reaction in the nanospray tip (Figure 2.2(i)). The reaction time was optimized using TG 18:1(9Z)/18:1(9Z)/18:1(9Z). The optimal reaction time was 1.5 minutes at using a 10.13 μ L/min flow rate. The reaction time was optimized for high product yield and low side reactions.

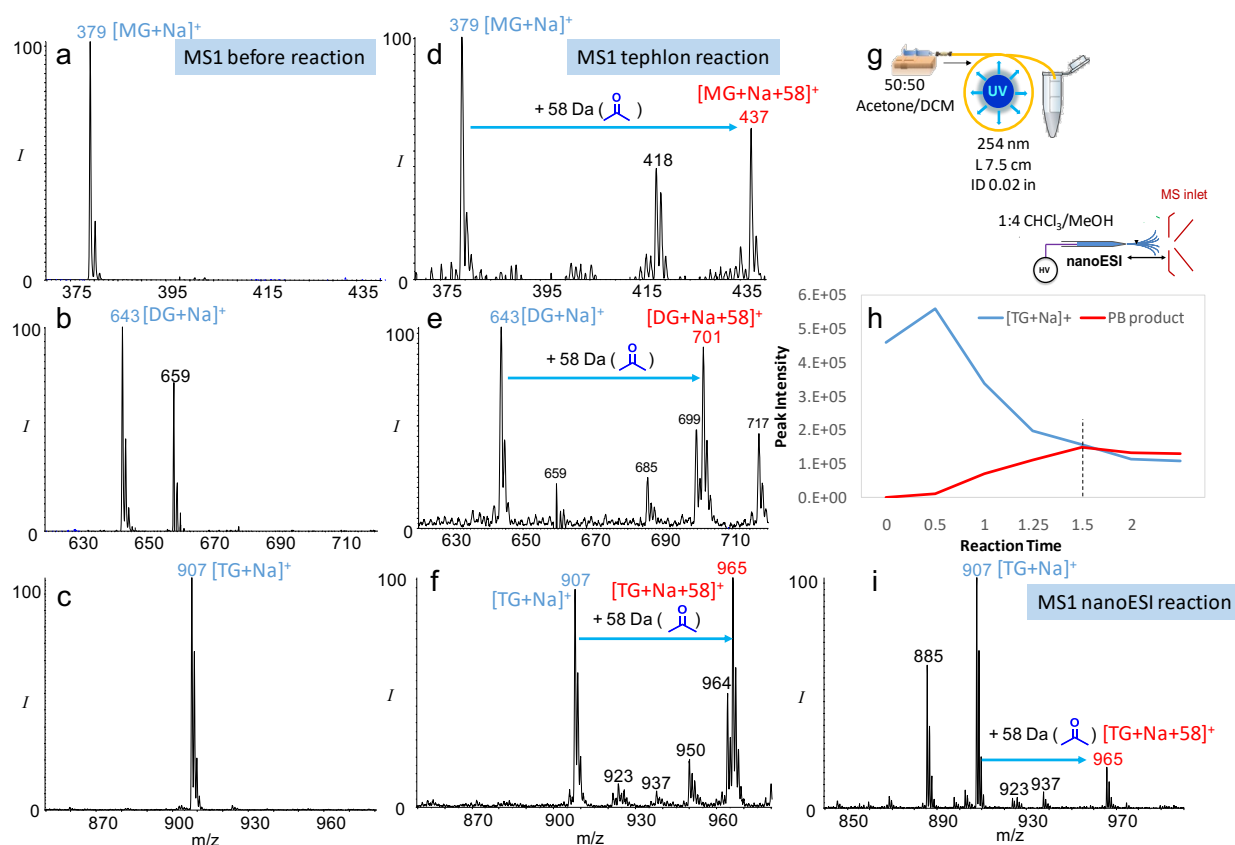


Figure 2.2 Offline PB reaction of glycerolipid standards 5 μ M in 1:4:0.5 chloroform/methanol/water containing 1.1mM sodium acetate. NanoESI MS¹ spectra before reaction in positive ion mode: (a) MG 18:1(9Z)/0/0/0, (b) DG 18:1(9Z)/18:1(9Z)/0/0, and (c) TG 18:1(9Z)/18:1(9Z)/18:1(9Z). NanoESI MS¹ spectra after offline PB reaction in positive ion mode: (d) MG, (e) DG, and (f) TG. (g) Offline reaction setup with tephlon tubing and nanoESI setup. (h) Optimized reaction kinetics (reaction time 1.5 min). (i) PB reaction of TG 18:1/18:1/18:1 in nanoESI tip.

2.4.2 PB-MS/MS CID for MG and DG C=C location isomer analysis

CID fragmentation of intact adduct species reveals structural information about acyl chain composition in both MG and DG species (Figure 2.3 (a), (c), (e), and (g)). When CID is performed on the PB product after the reaction, characteristic diagnostic ions are observed which indicate double bond location. In Figure 2.3(b), CID of the $[MG+Na]^+$ PB product (m/z 437) reveals fragment ions at m/z 269 and 295 indicating a Δ^9 C=C. For MG species, MS^2 CID is sufficient to obtain structural information about C=C location.

For DG, MS^2 CID is also sufficient to obtain structural information about C=C location but interestingly if the adduct being used is changed then different fragments appear. For both Na and Li DG adducts, a fragment corresponding to the $[FA+adduct]^+$ (Figure 2.3 (c) and (e)) and $[FA+adduct+58]^+$ (Figure 2.3 (d) and (f)) can be observed before and after reaction, respectively. Whereas, if the more popular ammonium adduct (Figure 2.3 (g) and (h)) is used these fragments are not observed. The importance of observing these peaks is crucial to structural identification in TG. The $[FA+adduct+58]^+$ peak can be isolated and MS^3 performed to determine C=C location. Moving forward, both the Na and Li adduct produce the fatty acyl adduct peak, but overall the Na adduct was chosen since this method was to be applied to biological samples where more sodium is present.

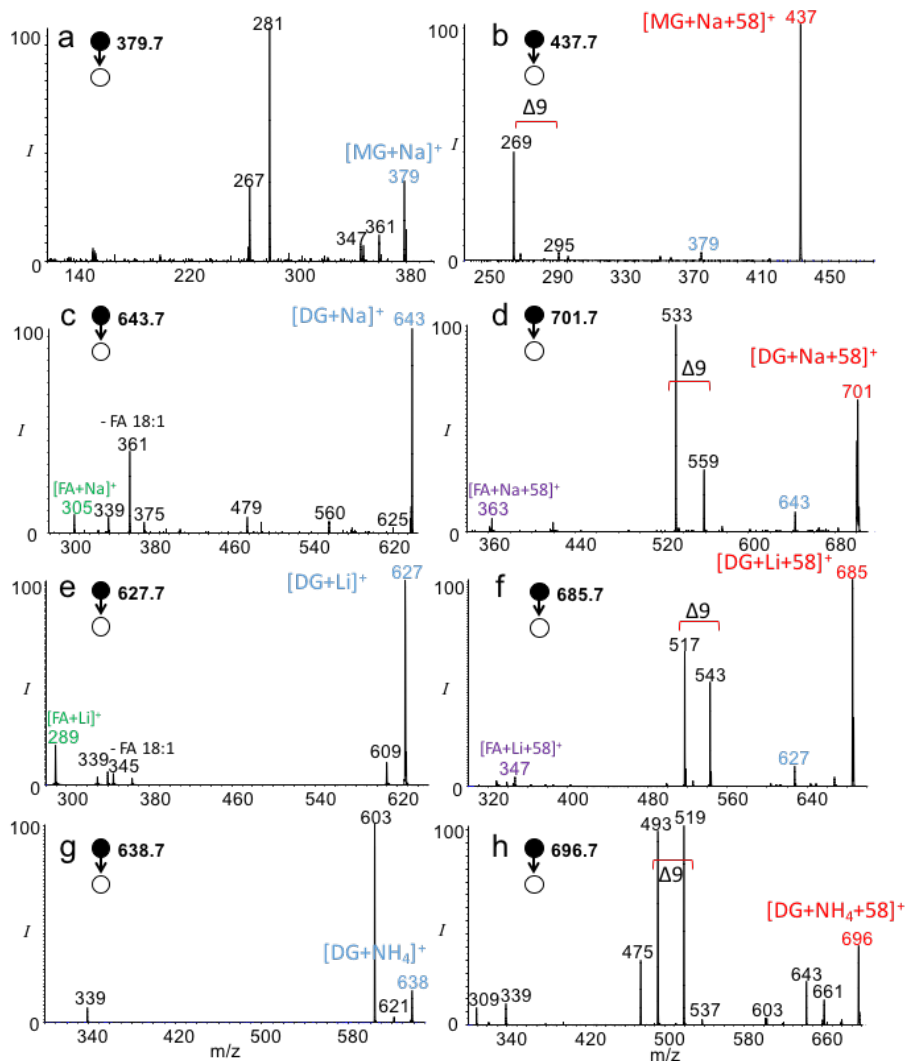


Figure 2.3 CID spectra of MG 18:1(9Z)/0:0/0:0 sodium adduct (a) before reaction and (b) MG PB product after reaction. CID spectra of DG 18:1(9Z)/18:1(9Z)/0:0 sodium adduct (c) before reaction and (d) DG PB product after reaction. CID spectra of DG lithium adduct (e) before reaction and (f) DG PB product after reaction. CID spectra of DG ammonium adduct (g) before reaction and (h) DG PB product after reaction.

2.4.3 PB-MS³ CID for TG C=C location isomer analysis

TG structural identification and C=C location required MS³ analysis. A MS¹ spectra of the [TG+Na]⁺ (m/z 879) and [TG+Na+58]⁺ PB product (m/z 937) before and after reaction can be seen in Figure 2.4 (a) and (b) respectively. The CID spectrum of [TG+Na]⁺ (m/z 879) reveals three peaks corresponding to the neutral loss of each of the fatty acyl chains (Figure 2.4(c)). CID of the [TG+Na+58]⁺ (m/z 937) reveals even more structural information (Figure 2.4(d)). The peaks corresponding to one acyl chain loss that are also observed in before reaction CID can be seen in

the after-reaction CID spectrum as well. The yellow highlighted region corresponds to regions of diagnostic ions for the intact TG species and diagnostic ions for the TG species after the loss of one acyl chain. Although these peaks are diagnostic ions, the peaks tend to overlap when the TG species become more complex. These peaks could not be used for C=C location. However, similar to the DG fragmentation, a $[FA+Na+58]^+$ peak is observed.

For standard TG 16:0/18:1(9Z)/18:2(9Z), a $[18:1+Na+58]^+$ peak (m/z 363) and a $[18:2+Na+58]^+$ peak (m/z 361) can both be formed after CID of the PB product (m/z 937) and isolated in MS³. Isolation of the $[18:2+Na+58]^+$ peak (m/z 361) reveals diagnostic ion pairs at m/z 195, 221 and m/z 235, 261 indicating the C=C location at $\Delta 9$ and $\Delta 12$, respectively (Figure 2.4(e)). Isolation of the $[18:1+Na+58]^+$ peak (m/z 363) reveals a diagnostic ion at m/z 195 indicating the C=C location at $\Delta 9$ (Figure 2.4(f)). The second diagnostic ion, m/z 221, is very low in abundance. The aldehyde diagnostic ion was drastically higher than the other diagnostic ion; this was observed in MG, DG, and TG species.

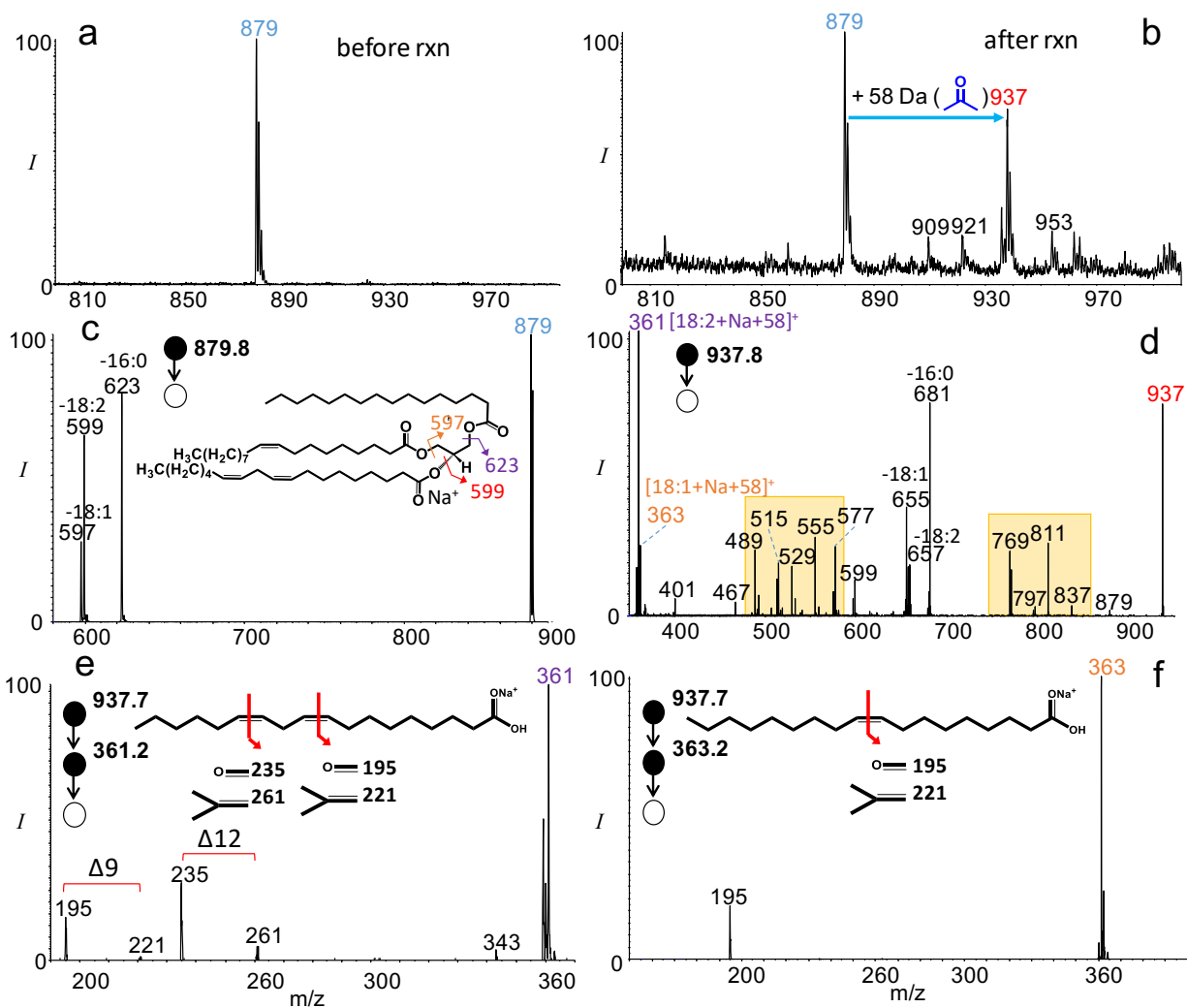


Figure 2.4 PB-MS³ of TG 16:0/18:1(9Z)/18:2(9Z,12Z) 10 μ M in 1:4:0.5 chloroform/methanol/water containing 1.11 mM sodium acetate. NanoESI MS¹ spectra in positive mode: (a) before reaction and (b) after offline PB reaction. MS² beam-type CID of (c) [TG+Na]⁺ at m/z 879.7 and (d) the PB product [TG+Na+58]⁺ at m/z 937.7. MS³ CID of (e) [18:2+Na+58]⁺ (m/z 363.2) and (f) [18:1+Na+58]⁺ (m/z 363.2).

2.4.4 Analysis of TG extract from human plasma

After developing the offline PB reaction method for MG, DG, and TG, it was applied to a biological sample. TGs and CEs are among the most abundant lipids present in the blood ranging from μ M to mM concentrations.^{29,30} A neutral lipid extraction protocol was used to extract TGs from human plasma. The MS¹ TG profile before and after reaction is shown in Figure 2.5 (a) and (b) respectively. CID of isolated PB product m/z 939 reveals neutral losses for acyl chains 16:0 and 18:1. Peaks corresponding to [16:1+Na+58]⁺ (m/z 335), [18:1+Na+58]⁺ (m/z 363), and

$[18:2+\text{Na}+58]^+$ (m/z 361) are also present (Figure 2.5(c)). When isolated in MS^3 , $939 \rightarrow 363$ reveals C=C location isomers at $\Delta 9$ (195, 221) and $\Delta 11$ (223, 249) for the 18:1 fatty acyl chain (Figure 5e). Again, the second ion of the diagnostic pair is very low in abundance compared to the aldehyde diagnostic ion. When isolated in MS^3 , $939 \rightarrow 361$ reveals C=C location at $\Delta 9$ (195, 221) and $\Delta 12$ (235, 261) for the 18:2 fatty acyl chain (Figure 2.5(f)). Table 1 summarizes the structural identification for each PB product peak isolated. MS^2 provides acyl chain composition and MS^3 reveals C=C location for unsaturated acyl chains. *Sn*- position is unknown so “_” is used to separate acyl chains.

PB product m/z 911 was also isolated and both MS^2 and MS^3 CID were performed to structurally identify abundant species. Neutral losses for acyl chains 14:0, 16:0, 16:1, and 18:1 are observed in CID of the PB product. Peaks corresponding to $[16:1+\text{Na}+58]^+$ (m/z 335), $[18:1+\text{Na}+58]^+$ (m/z 363), and $[18:2+\text{Na}+58]^+$ (m/z 361) are also present (Figure 2.5(d)). When isolated in MS^3 , $911 \rightarrow 335$ reveals C=C location at $\Delta 9$ (195, 221) for the 16:1 fatty acyl chain (Figure 2.5g). When isolated in MS^3 , $911 \rightarrow 361$ reveals C=C location at $\Delta 9$ (195, 221) and $\Delta 12$ (235, 261) for the 18:2 fatty acyl chain (Figure 2.5(h)).

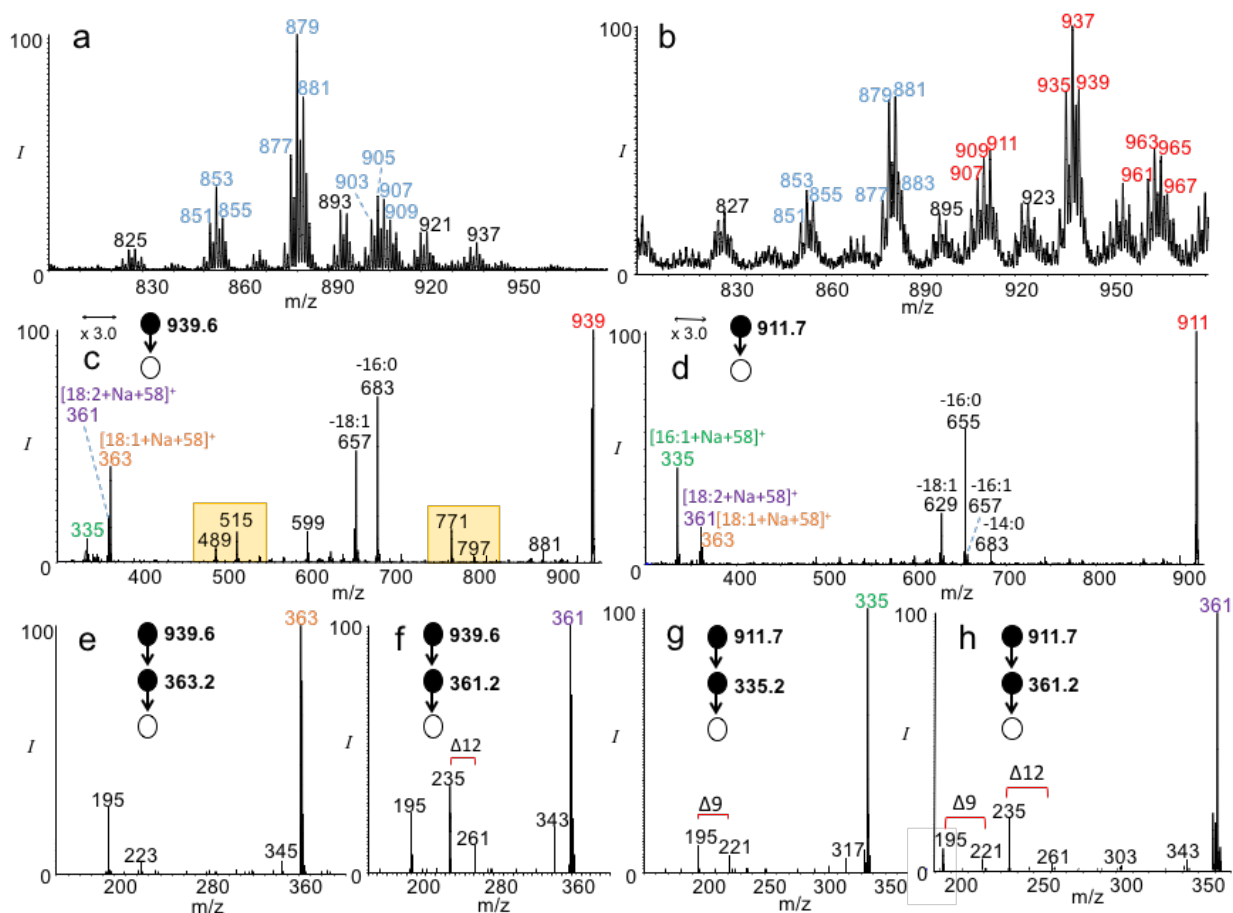


Figure 2.5 Structural identification of abundant unsaturated TG species from human plasma. MS1 profile of TG species in human plasma (a) before reaction and (b) after reaction. MS2 beam type CID of (c) m/z 939.7 and (d) m/z 911.7. MS³ CID of (e) 939→[18:1+Na+58]⁺ m/z 363.2, (f) 939→[18:2+Na+58]⁺ m/z 361.2, (g) 911→[16:1+Na+58]⁺ m/z 335.2, and (h) 911→[18:1+Na+58]⁺ m/z 363.

Table 2.1 Structural Composition of abundant TAG species in Human Plasma extract

TG	Mass	MS ¹		MS ²				MS ³	
		Na adduct	PB product	Abundant Composition	Fragment acyl chain loss (neutral loss)	FA chains	FA+Na+PB	MS ³ D-ions	C=C Position
50:2	830.736	853.726	911.726	14:0_18:1_18:1 16:1_18:1_16:0 16:0_18:2_16:0	655 (256)	16:0	-	-	-
					683 (228)	14:0	-	-	-
						16:1	335	195, 221	9
					629 (282)	18:1	363	195	9
						18:2	361	195 235, 261	9, 12
50:3	828.721	851.711	909.711	14:0_18:2_18:1 16:1_18:1_16:1 16:0_18:2_16:1	653 (256)	16:0	-	-	-
					681 (228)	14:0	-	-	-
					655 (254)	16:1	335	195, 221	9
					627 (282)	18:1	363	195	9
					629 (280)	18:2	361	195 235, 261	9, 12
52:2	858.768	881.758	939.758	16:0_18:1_18:1 16:0_18:0_18:2 16:1_18:1_18:0	683 (256)	16:0	-	-	-
					655 (284)	18:0	-	-	-
					16:1	16:1	335	195, 221	9
					18:2	18:2	361	195 235	9, 12
					657 (282)	18:1	363	195 223	9 11
52:3	856.752	879.742	937.742	16:0_18:2_18:1 16:1_18:1_18:1	681 (256)	16:0	-	-	-
					683 (254)	16:1	335	195, 221	9
					657 (280)	18:2	361	195 235, 261	9, 12
					655 (282)	18:1	363	195 223	9 11
52:4	854.736	877.726	935.726	16:0_18:2_18:2 16:1_18:2_18:1	679 (256)	16:0	-	-	-
					681 (254)	16:1	335	195, 221	9
					655 (280)	18:2	361	195 235, 261	9, 12
					653 (282)	18:1	363	195	9
54:2	886.799	909.789	967.789	18:1_18:1_18:0 20:1_18:1_16:0 20:0_18:2_16:0 22:0_16:1_16:1 20:0_18:1_16:1	711(256)	16:0	-	-	-
						16:1	335	195, 221	9
					683 (284)	18:0	-	-	-
					685 (282)	18:1	363	195 223	9 11
					687 (280)	18:2	361	195 235, 261	9, 12
					655 (312)	20:0	-	-	-
					657 (310)	20:1	391	223	11
					627 (340)	22:0	-	-	-
54:3	884.783	907.773	965.773	18:1_18:1_18:1 18:0_18:1_18:2	685 (280)	18:2	363	195	9
					681 (284)	18:0	-	-	-
								195	9
					683 (282)	18:1	361	223	11

Table 2.2 continued: Structural Composition of abundant TAG species in Human Plasma extract

TG	Mass	MS ¹		MS ²				MS ³	
		Na adduct	PB product	Abundant Composition	Fragment acyl chain loss (neutral loss)	FA chains	FA+Na+PB	MS ³ D-ions	C=C Position
54:4	882.768	905.757	963.757	18:2_18:2_18:0 18:2_18:1_18:1	679 (284)	18:0	-	-	-
					681 (282)	18:1	363	195	9
					683 (280)	18:2	361	195 235	9,12
54:5	880.752	903.742	961.742	18:2_18:2_18:1 20:4_16:0_18:1	705 (256)	16:0	-	-	-
					681(280)	18:2	361	195 235	9,12
					679 (282)	18:1	363	195	9
								-	
						20:4	385	179 219, 245 259, 285	5,8,11,14

2.5 Conclusion

An offline PB reaction method was developed to determine the C=C location of MG, DG, and TG species. This method was then applied to a complex sample, human plasma. The reaction was performed in a Teflon tubing coil and the reaction product was collected and analyzed by MS. Structural identification and C=C location of MG and DG species was carried out through MS² of the [GL+Na]⁺ and [GL+Na+58]⁺ peaks. For TG species, MS² CID reveal structural information and further MS³ CID is required to determine C=C location and reveal C=C location isomers if any. The most abundant TG species from the human plasma extract were identified for acyl chain composition and for the unsaturated species, the C=C location was determined. Most 18:1 species were Δ 9 C=C location but some contained the Δ 11 isomer. All 18:2 species had C=C location at Δ 9, Δ 12. Species containing 16:1 had C=C location at Δ 9.

CHAPTER 3. UNDERSTANDING LIPID LOCALIZATION IN THE DEVELOPING LUNG USING NANO-DESI MASS SPECTROMETRY IMAGING

3.1 Abstract

Understanding the localization and role of lipids in different stages of lung development provides important insights into normal lung progression. Herein, we use nanospray desorption electrospray ionization mass spectrometry imaging (nano-DESI MSI) for label-free spatial localization of lipids in both embryonic and postnatal mouse lung tissues. The images produced from nano-DESI/MSI experiments are compared with optical images to identify distinct anatomical features (e.g. airways, bronchi, alveolar regions, etc). Embryonic stage lipids are typically PC species with <18 carbon chains and lower degrees of unsaturation. These lipids are mostly consistent with highly abundant surfactant lipids. In addition to surfactant lipids, the postnatal (day 7 and 28) lung samples contain longer chain lipids (e.g.C20) with higher degree of unsaturation and larger head group variety. Embryonic lung tissue shows no localization to airways since surfactant lipids are the most prevalent species. As the lung matures, lipids with more diversity in head group, chain length, and degree of unsaturation begin to localize to airways consistent with their role in lung's response to inflammation and as precursors to lipid mediators.

3.2 Introduction

Molecular signatures of specific cell types at different stages of lung development are critically important to understanding and mitigating impaired lung function. Although little is known about cellular processes associated with lung maturation,⁴⁴ several studies have provided insights into the overall changes of the proteome^{45,46} and lipidome^{47,48} at different developmental stages. A concerted effort dedicated to establishing detailed molecular signatures of developing mouse and human lungs has already generated a substantial amount of molecular information available to the scientific community (www.lungmap.net).⁴⁴ Mouse lungs have been systematically investigated to establish the foundation for studying more precious human lung samples.

Mouse lung development involves four major stages: (1) pseudoglandular, (2) canalicular, (3) saccular, and (4) alveolar. During stage 1, branching morphogenesis occurs throughout embryonic

day 9.5-16.5 (E9.5-16.5). This involves the formation of major airways and the bronchial tree structure which is the basis for further development. In stage 2 (E16.5-17.5), capillaries are formed, vascularization begins, and both type I and II alveolar cells emerge. Stage 3 starts around embryonic day 17.5 and continues after birth (E17.5-PND5). During this time, airspaces and capillary networks expand, and alveolar sacs start to form. This stage also involves pulmonary surfactant production. The final postnatal stage (PND5-30) is more commonly referred to as alveolarization. This is the process in which the previously formed airspaces divide to form alveoli - lung structures that increase surface area for gas exchange. Most of the alveolarization process occurs before PND15.⁴⁹⁻⁵¹

Pulmonary surfactant in mammalian lungs reduces surface tension and prevents alveolar collapse.^{52,53} Surfactant is produced by alveolar type II cells and stored in specific organelles called lamellar bodies.^{52,54,55} Lipids make up 90% of the surfactant composition and the remaining 10% is proteins.^{52,53} Phosphatidylcholine (PC) is the most common class of surfactant lipids, which accounts for ~70-80% lipid mass. Within this class, dipalmitoyl phosphatidylcholine, DPPC or PC 16:0/16:0 is the most abundant species present in the pulmonary surfactant.⁵²⁻⁵⁶ Unsaturated PC species account for ~17% of the total PC content.⁵⁴ The saturated structure of DPPC and its ability to be tightly compressed against other DPPC molecules^{55,57} helps reduce surface tension in the airways. Other PC species are also abundant in the surfactant including: PC 16:0/14:0, PC 16:0/16:1, PC 16:0/18:1, and PC 16:0/18:2.⁵⁵ Other lipid classes present in the pulmonary surfactant include PG (7-8%), PE (5%), PI (2-3%), PS, LPC and SM (2%).⁵²⁻⁵⁵

Lipids play important roles in lung diseases, the lung's response to inflammation, and as precursors to lipid mediators. The role of these molecules in lung diseases has been extensively studied, but relatively little is known about their role in the normal lung development. A recent lipidomics study identified 924 lipid species from 21 lipid subclasses in mouse lung tissue from post-natal samples using ultra performance liquid chromatography mass spectrometry (UPLC-MS).⁴⁷ Pronounced changes in abundances of lipids involved in apoptosis, inflammation, and energy storage have been observed at different stages of lung development. For example, pro-apoptotic sphingolipids are dramatically enhanced in the lungs of young (PND7) mice. Meanwhile, glycerophospholipids containing long chain polyunsaturated fatty acids (PUFA) often associated with inflammation processes are most abundant in the lungs of adult mice. Karnati et al. analyzed

and quantified lipid species using electrospray ionization tandem MS (ESI-MS/MS) from postnatal mice (PND1, PND15, and PND84). Lung tissue from newborn mice (PND1) contained lipids that were monounsaturated and mostly related to surfactant, whereas, lung tissues from adult mice (PND84) were enriched with polyunsaturated species.⁵⁸ Herein, we use an imaging approach to examine the localization of lipids in the developing murine lung and incorporate lipidomics data that includes lung tissue from the embryonic stage, furthering this previous study.

Mass spectrometry imaging (MSI) allows for label-free imaging of samples and provides spatial localization of biomolecules in tissues.^{11,13,14,59–63} Ambient ionization techniques^{1,11,64–67} enable imaging of biological samples without special sample pretreatment.^{13,16,62,68} In this study, we used nanospray desorption electrospray ionization (nano-DESI) MSI⁶⁸ to image lipids present in mouse lung tissues at different stages of lung development. Nano-DESI is an ambient ionization technique that utilizes gentle liquid extraction of analytes from the surface of the sample into a liquid bridge formed between two fused-silica capillaries.¹² The extracted analyte molecules are transferred to a mass spectrometer inlet and ionized by ESI.^{11,13,14,68} It has been demonstrated that nano-DESI MSI provides excellent coverage of lipids (up to 50% in comparison with Folch extraction whole lung lipidomics) and metabolites in mouse lung tissues.⁶⁹ Herein, lipids in tissue samples from embryonic mice day 18.5 (E18.5), postnatal mice from day 7 (PND7) and adult mice postnatal day 28 (PND28) were identified using LC-MS/MS and imaged using nano-DESI MSI. From previous literature findings, we expect samples from an early developmental stage should mostly be saturated and monounsaturated species related to surfactant, with PC 16:0/16:0 being most prominent. Whereas later developmental stages should contain glycerophospholipids with PUFAs. This study combines imaging and lipidomics data to provide more insights into the localization of lipids in mouse lung tissue during normal lung development.

3.3 Experimental

3.3.1 Reagents

Acetylcholine-1,1,2,2-d4 (CDN isotopes), LPC 19:0, PC (12:0/13:0), PE (15:0/15:0), PG (15:0/15:0), PI (16:0/16:0), PS (17:0/17:0) (Avanti Polar Lipids), Oleic acid-d17 (Cayman Chemical) and arachidonic acid-d8 (Sigma Aldrich) were used as internal standards for either positive or negative mode nano-DESI MSI experiments. Carboxymethyl cellulose (CMC) was

purchased from Sigma-Aldrich (St. Louis, MO) and used as received. The CMC embedding medium was prepared as follows. First, 450 mL of deionized water was heated in a 500 mL bottle with cap to 70°C in a dry shaking incubator. Next, 10 g (2%w/v) of carboxymethyl cellulose was added into the bottle and the solution was incubated overnight at 70°C with shaking. Finally, the solution volume was brought to 500 mL by adding water and stirred until fully mixed. The CMC solution was refrigerated until use.

3.3.2 Tissue Collection and Handling

The mice used in these experiments were supplied by the Cincinnati Children's Hospital Medical Center Animal Care Facility. While at the Facility, the mice were treated following the National Institutes of Health and institutional guidelines for the use of laboratory animals. All the experimental protocols were reviewed and approved by the Cincinnati Children's Hospital Research Foundation Institutional Animal Care and Use Committee. For postnatal samples, C57BL/6 JAX mice (Jackson Laboratory, Bar Harbor, ME) were sacrificed at embryonic day 18.5, postnatal day 7 and 28 by CO₂ asphyxiation. The lungs were removed, perfused with 10 mL of ice-cold PBS, and inflated by filling with ice cold CMC. The trachea was subsequently tied with a ligature maintaining the inflation of the lobe and the lung was washed in a weigh boat partially filled with ice cold PBS to remove any residual blood or debris. To embed separate lobes, the main left and right bronchus were ligated with a suture before separating from trachea, the lung was placed in a plastic mold filled with ice cold CMC on dry ice. CMC was added as needed to cover the tissue. Embryonic samples were obtained by harvesting mouse embryos on gestational day 18.5. Dams were exsanguinated by CO₂ inhalation and fetuses obtained by hysterectomy. The pups were extracted from the uterus and placed in individual small weigh boats on ice. Extra-fetal membranes were removed, the samples were transferred into plastic outer molds, the molds were filled with CMC, and frozen on dry ice. CMC was added as needed to cover the tissue. The embedded tissue was stored in a -80°C freezer. Lung tissues were sectioned using a ThermoCryostar NX70 cryostat microtome (Thermo Scientific, Waltham, MA). Sections were thaw-mounted onto glass slides for the imaging experiments and stored in a -80°C freezer until ready for analysis.

3.3.3 Lipidomics

Lipidomics experiments were performed as described previously. Briefly, tissue samples were homogenized using a Qiagen TissueLyser II with a 2x24 adapter (chilled to -20°C) and subjected to a modified Folch extraction procedure.⁷⁰ The organic layer of the Folch extraction was reconstituted in MeOH and analyzed using LC-ESI-MS/MS on a Waters NanoAquity UPLC system (Waters column, HSS T3 1.0 mm x 150 mm x 1.8 µm particle size) interfaced with a Velos-ETD Orbitrap mass spectrometer (Thermo Scientific, San Jose, CA). LC utilized a 90 min gradient elution (mobile phase A: ACN/H₂O (40:60) containing 10 mM ammonium acetate; mobile phase B: ACN/IPA (10:90) containing 10 mM ammonium acetate) at a flow rate of 30 µl/min. MS/MS experiments were performed using both higher-energy collision dissociation (HCD) and collision-induced dissociation (CID). The samples were analyzed in triplicates. Data analysis was performed using LIQUID (Lipid Informed Quantitation and Identification) as described in our previous study.⁴⁷ Peak apex intensities were exported for statistical analysis.

3.3.4 Nano-DESI Imaging

A custom nano-DESI source⁶⁸ with shear force microscopy¹⁶ capability was interfaced to a LTQ Orbitrap XL and Q-Exactive MS (Thermo Fisher Scientific, Waltham, MA). The nano-DESI probe consisted of two 150µm OD x 50µm ID fused silica capillaries. The primary capillary delivers the extraction solvent (9:1 methanol/water) to the sample and a secondary capillary transfers the extracted molecules to the MS inlet. A third capillary is used as the shear force probe that maintains a constant distance between the nano-DESI probe and the sample.¹⁷ The shear force capillary (800µm OD x 200µm ID) was pulled to a 20µm OD tip using a P-2000 micropipette puller system (Sutter Instruments, Novato, CA). All capillaries were positioned using high-resolution micromanipulators (XYZ 500MIM, Quater Research and Development, Bend, OR) and monitored using two Dino-Lite digital microscopes (AnMo Electronics Corporation, Sanchong, New Taipei, Taiwan). The 9:1 methanol/water extraction solvent contained internal standards for both positive and negative ionization modes. Positive mode internal standards include Acetylcholine-1,1,2,2-d₄, LPC 19:0, and PC (12:0/13:0). In negative mode, oleic acid-d₁₇, arachidonic acid-d₈, PE (15:0/15:0), PG (15:0/15:0), PI (16:0/16:0) and PS (17:0/17:0) were used as internal standards.

Embryonic samples were analyzed using the Q-Exactive instrument. In these experiments, the solvent was delivered through the primary capillary at a flow rate of 400 nL/min with an applied

voltage of 2.3 kV. For the postnatal samples analyzed using the LTQ Orbitrap XL, the solvent flow rate was 500 nL/min with a voltage of 3.5 kV. The capillary inlet was heated to 250°C and held at 30 V. Imaging experiments were performed by scanning each sample line by line under the shear force/nano-DESI probe at constant velocity while collecting high-resolution mass spectra (mass resolution 60,000). The embryonic samples were analyzed by moving the sample under the probe at 60 $\mu\text{m/s}$ and the spatial resolution was 10 μm . The postnatal samples were analyzed using a scan rate of 70 $\mu\text{m/s}$ and the spatial resolution of 100 μm .

3.3.5 Data Processing

Lipids and small molecules observed in the MSI experiments were identified based on the accurate mass measurement and comparison with LC-MS/MS data obtained for the same developmental stages. Raw data was collected using Xcalibur software (Thermo Scientific) and subsequently processed using MSI Quickview⁶⁸ (PNNL, Richland, WA) and Peak-by-Peak (SpectroSwiss, Lausanne, Switzerland).

3.4 Results and Discussion

In this study, we examined the spatial localization of lipids and metabolites in mouse lungs at different stages of lung development. Lipidomic analysis was performed to provide in-depth information on the lipid composition at different developmental stages to complement the imaging data. Representative nano-DESI mass spectra showing lipid profiles obtained for E18.5 and PND7 samples are presented in Figure 3.1a. Several abundant lipids labeled in the spectra are listed Figure 3.1b. We note that the embryonic samples were analyzed using a different instrument. Therefore, a direct comparison of signal intensities cannot be performed but general trends can be inferred. The black trace represents the average positive mode spectrum for E18.5 samples. The abundant lipids present in the spectrum are mostly saturated or monounsaturated PC species with <34 carbons. Little to no signal intensity is observed for PC species with higher degree of unsaturation compared to the red trace that represents the average positive mode spectrum for PND7 samples.

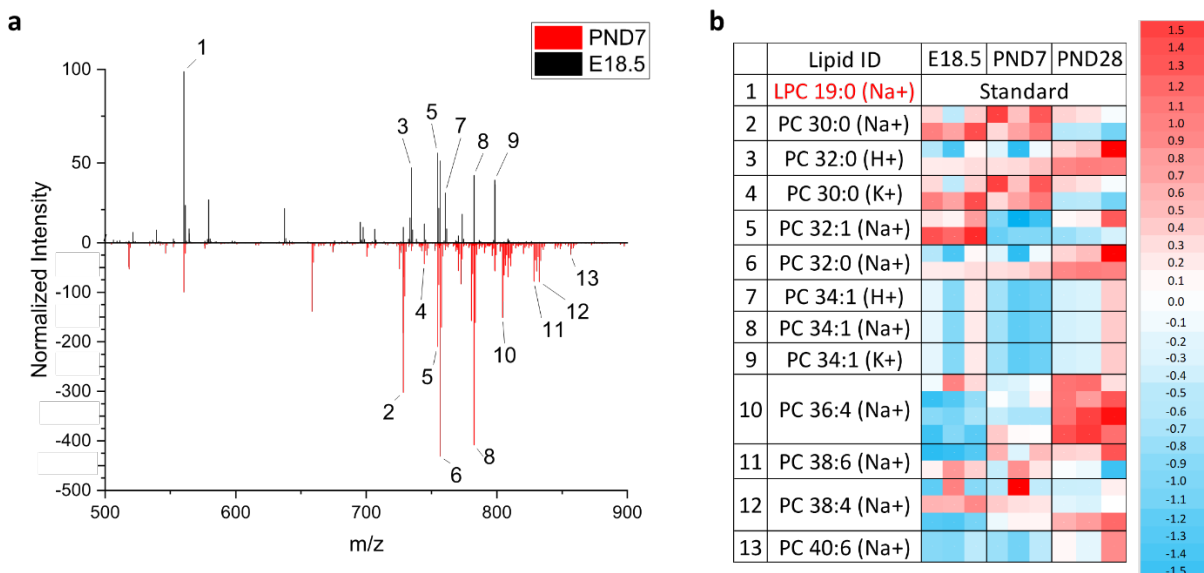


Figure 3.1 a) Average positive mode nano-DESI mass spectra of lipid profiles from E18.5 (black trace shown as positive signal) and PND7 samples (red trace shown as negative signal). Profile represents an average spectrum over the entire tissue section with signal intensity normalized to the signal of the internal standard, LPC 19:0. b) Selected lipids labeled in 1a are identified in the table along with z-scores calculated from acquired lipidomics data. Enriched lipid species are represented by a positive z-score (red) whereas, a negative z-score (blue) indicates lipid depletion.

Lipidomics data for selected lipid species are presented in Figure 3.1b. Lipidomics analysis of lung tissues from E16.5, E18.5, PND7, and PND28 identified 102 phosphatidylcholine (PC), 86 triacylglycerol (TG), 20 diacylglycerol (DG), 17 sphingomyelin (SM), 12 ceramide (Cer), 5 phosphatidylserine (PS), and 3 galactosylceramide (GalCer) species in positive mode. In negative mode, 67 phosphatidylethanolamine (PE), 23 phosphatidylglycerol (PG), 16 Cer, 15 phosphatidylinositol (PI), 9 PS, 9 cardiolipin (CL), 4 GalCer, and 2 ganglioside GM3 species were identified. Z-scores calculated from the lipidomics data indicate variations in the average abundance of each lipid species at different developmental stages. A positive z-score (red) represents lipids that are enriched in a specific sample, whereas, a negative z-score (blue) indicates lipid depletion. Overall, the results of the lipidomics and nano-DESI MSI analysis show a consistent trend in the lipid composition. Specifically, monounsaturated PC species (1-9) that are related to surfactant are the most abundant lipids present in embryonic lung tissues (E18.5). Meanwhile, polyunsaturated species (10-13) are fairly abundant in the postnatal, PND7, samples. A similar comparison for PND7 and PND28 samples is shown in Figure A1a with the corresponding z-scores listed in Figure A1b. The lipid species with lower degrees of unsaturation

most likely present in surfactant are still the most abundant species in both postnatal samples. However, both PND7 and PND28 samples contain an increased abundance of the polyunsaturated species compared to the embryonic stage, as indicated by the positive z-scores.

Figure 3.2 shows ion images obtained for abundant surfactant lipids across the three developmental stages in both positive and negative mode, including abundant PC and PG species. The corresponding optical images are shown in the figure. The images are normalized to the signal of the sodium adduct of the internal standard, LPC 19:0. It has been demonstrated that normalization to the standard helps compensate for matrix effects in MSI experiments.⁶⁰ Matrix effects originate from differences in lipid composition or changes in alkali metal concentrations across the sample.⁶⁰ In order to assess the importance of matrix effects in lung tissue imaging, we compared ion images of the protonated $[M+H]^+$ species and sodium, $[M+Na]^+$, and potassium, $[M+K]^+$ adducts of PC 32:0 normalized to the internal standard, LPC 19:0, and to the total ion current (TIC) as shown in Figure A2. Similar ion images normalized to the TIC were obtained for sodium and potassium adducts of PC 32:0. However, the ion image of the $[M+H]^+$ species normalized to the TIC shows signal enhancement on the left edge of the tissue. This enhancement, which is likely attributed to the lower abundance of Na^+ and K^+ in this region, is absent in the ion image normalized to the standard. The slightly different distributions obtained for $[M+H]^+$ species after normalization to the standard may be attributed to the lower abundance of these species in the mass spectra. Since similar ion images were obtained for sodium and potassium adducts of lipids in lung tissue images normalized to LPC 19:0, only sodium adduct distributions observed in positive mode data will be discussed throughout this paper. For negative mode experiments, ion images of $[M-H]^-$ species normalized to the TIC will be presented.

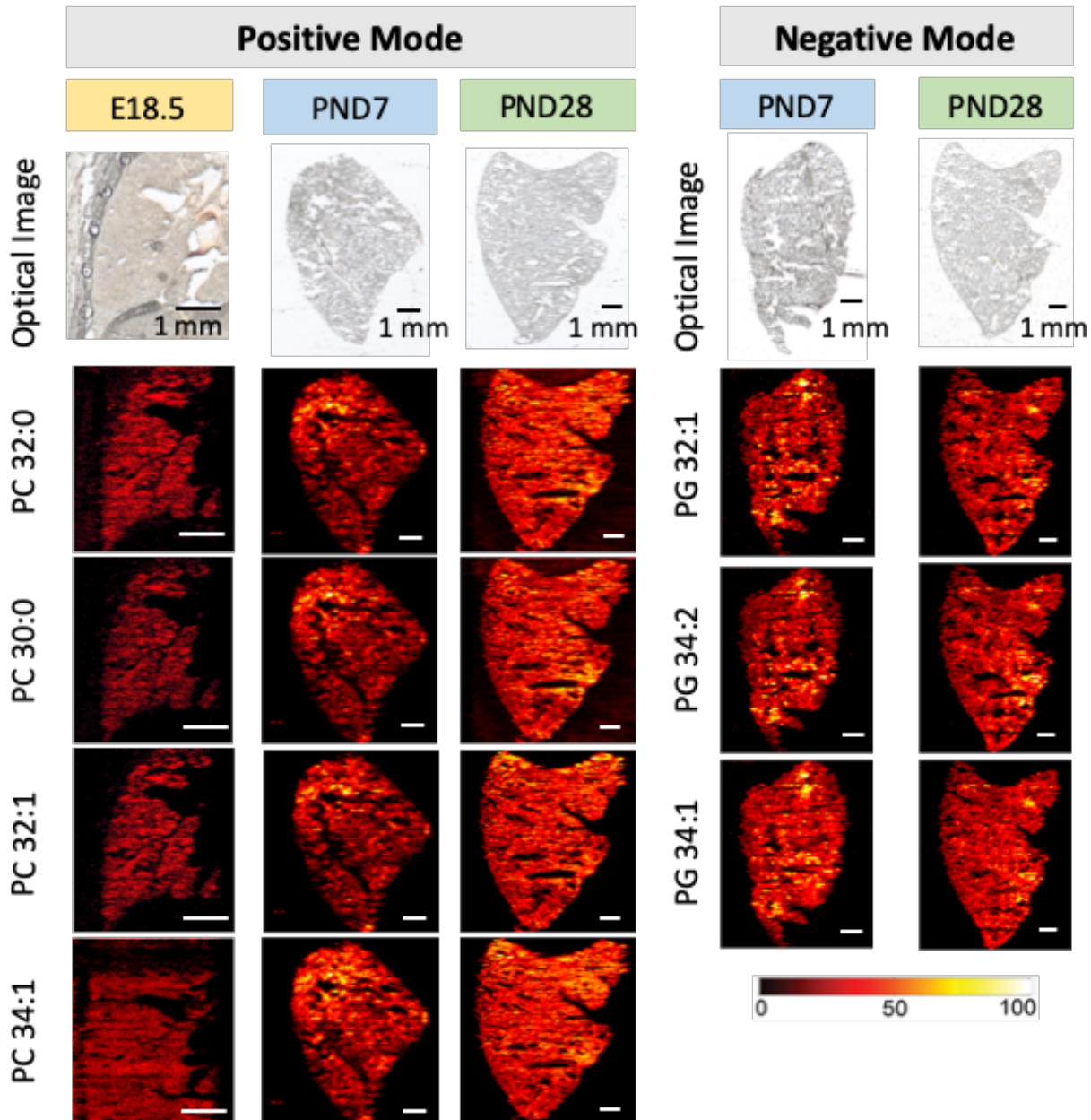


Figure 3.2 Optical and nano-DESI images of selected PC and PG species known to be abundant in pulmonary surfactant. These lipids are localized to alveoli across all three developmental stages. Specifically, for PC 34:1 in E18:5, this lipid is also located in the surrounding tissue, not just the lung. PC species were analyzed in positive mode as sodium adducts $[M+Na]^+$ and PG species were detected in negative mode as $[M-H]^-$. Scale bar indicates 1 mm. Intensity scale (0% black, 100% white) represents signal intensity of individual peaks normalized to the maximum value in each image. Positive mode ion images were normalized to LPC 19:0 and negative mode ion images were normalized to TIC.

Ion signals of PC and PG species shown in Figure 3.2 are evenly distributed throughout the lung indicating alveolar localization. We note that for E18.5 samples, whole body sections were used for imaging. As a result, some phospholipids in these images are observed outside the lung tissue. Specifically, several lipids including PC 32:0, PC 30:0, PC 32:1 known to be abundant in lung surfactant are localized to the lung tissue. In contrast, PC 34:1 is also present in the tissue surrounding the lung. These observations are consistent with the composition and role of surfactant in lungs. Surfactant is a lipoprotein fluid produced in the lungs to help reduce surface tension while breathing. PC (16:0/16:0) is the most abundant (58%) lipid in surfactant followed by PC (16:0/16:1) (13%), PC (16:0/18:1) (7.2%), and PC (14:0/16:0) (4.7%).^{57,71} PG lipids are the second most abundant species present in surfactant.⁵⁷ In most mammals the abundant PGs are present as PG (16:0/16:1), PG (16:0/18:1), and PG (16:0/18:2).⁷¹ To prepare the lungs for birth, Type II cells begin producing and storing surfactant inside the lamellar bodies during the third stage of lung development at E17.5, therefore, we expected to observe common surfactant lipids in E18.5 samples. Furthermore, the distribution of surfactant lipids is expected to correlate with the localization of the type II alveolar cells, which are present throughout the lung. These assertions are consistent with the imaging data presented in Figure 3.2.

Localization of lipids in tissues is dependent on the head group, degree of unsaturation, and carbon length. In positive mode PND28 samples, as the degree of unsaturation increases, lipids transition from alveolar to airway localization. Ion images of selected PC species shown in Figure 3.3 highlight this trend. The first series of PCs shown in Figure 3.3a contain 36 carbons with different degree of unsaturation (1 to 4). More saturated species show a more even distribution across the lung indicating alveolar localization. However, as unsaturation increases, localization around airways can be observed. This pattern holds true for other lipid series e.g. carbon 38, degree of unsaturation 2 to 6 shown in Figure 3.3b.

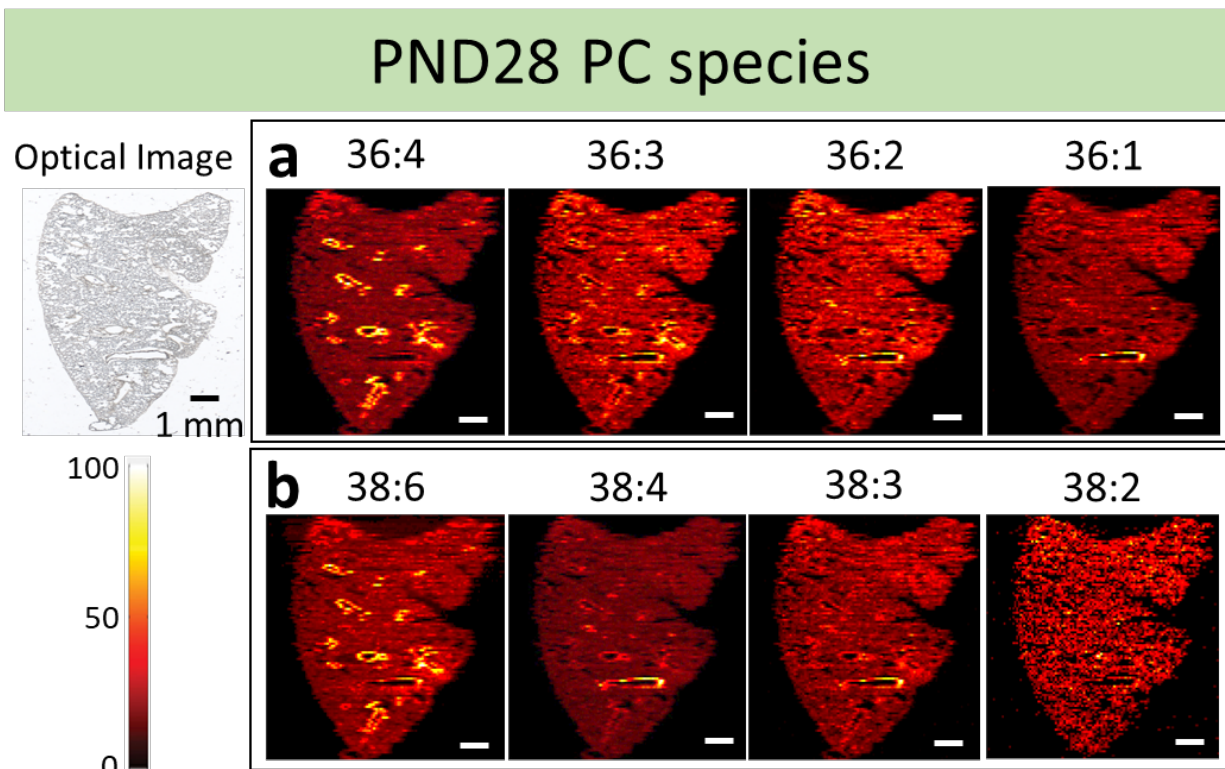


Figure 3.3 Optical and nano-DESI images of PC species from PND28 samples are arranged here by carbon number (C36 top row, C38 bottom row) and degree of unsaturation. Lipids with lower degrees of unsaturation have alveolar localization. Meanwhile, more unsaturated lipids localize around the airways and blood vessels of the lungs. Scale bar indicates 1 mm. Intensity scale (0% black, 100% white) represents signal intensity of individual peaks normalized to the maximum value in each image. Positive mode ion images were normalized to LPC 19:0.

For postnatal samples, lipids that vary only by the head group often exhibit very different localization patterns. Figure 3.4 shows representative images of unsaturated lipid species with different head groups observed in PND7 and PND28 samples, including PS, PI, PE, and PG in negative mode and PC and DG in positive mode. Localization around airways is observed in both developmental stages for unsaturated PC lipids i.e. PC 36:4, 38:4 and 40:6. Meanwhile, the unsaturated PI and PE species with the same acyl chains show mostly alveolar localization during early developmental stages (PND7) but as the lung matures, airway localization of these species is observed (PND28). In the ion images obtained for PI species in PND7 samples, several bright spots are observed corresponding to airways. These bright spots could be a possible indicator that as the lungs matures, they develop into a more defined localization that is seen in PND28 samples. Consistent with MALDI imaging of lung tissue reported by Murphy et al,⁷¹ unsaturated PC, PI,

and PE phospholipids are present only in low abundance in the surfactant but are enhanced along the airways of the mouse lung tissue as the lung develops. In contrast, DG species show an even distribution in the alveolar parenchyma in both PND7 and PND28 samples consistent with being cellular membrane components, precursor for glycerophospholipids, and highly regulated messenger lipids.⁷² DG lipids play a central role in many signaling pathways therefore they are highly regulated in order to maintain constant and controlled availability⁷³. Although some of the PG and PS species are not very abundant, the ion images observed for these species show alveolar localization, which is consistent with PG and PS species being cell related. Specifically, PG lipids are a component of surfactant produced in type II alveolar cells and PS lipids are structurally important in cell membranes.

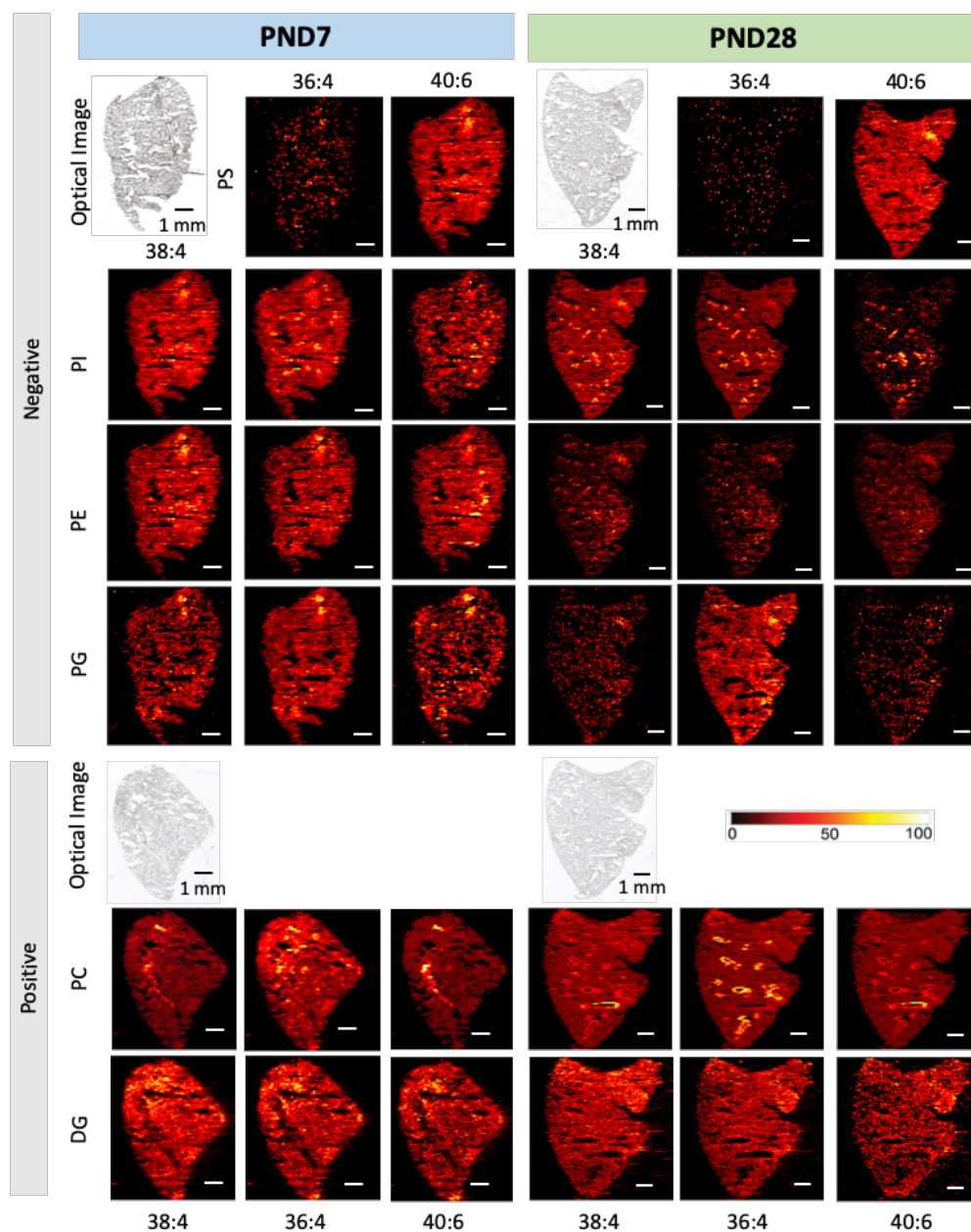


Figure 3.4 Nano-DESI images showing that lipid localization also depends on the head group of the lipid species and lung developmental stage. PUFA-containing lipids with different head groups observed in PND7 and PND28 samples are compared in the figure. For PC species, localization around airways can be seen in both stages of development. Ion images of PI species in PND7 show some very faint bright spots indicating some localization to airways but the localization is far more prominent in PND28 samples. Other lipid classes are localized to alveoli. Several PS and PG species were observed with very low abundance. Scale bar indicates 1 mm. Intensity scale (0% black, 100% white) represents signal intensity of individual peaks normalized to the maximum value in each image. Positive mode ion images were normalized to LPC 19:0 and negative mode ion images were normalized to TIC.

To better understand the origin of the observed differences in lipid distribution in lung tissues, we compared them with the spatial localization of fatty acids (FA) and other single-chain lipids including monoacylglycerols (MG) and LPC. In negative mode, FA species were observed in both the PND7 and PND28 samples (Figure 3.5). Biologically relevant FA species such as arachidonic acid (20:4), docosahexaenoic acid (22:6), linoleic acid (18:2), and palmitic acid (16:0) were identified and are present throughout the tissue. The alveolar localization pattern for FA species is consistent with their biological relevance. FA 16:0 is a major fatty acid that can be incorporated into PC 16:0/16:0, the major component in surfactant. FA 20:4 and DHA are precursors to lipid mediators that are important in the maintenance of lung homeostasis and inflammatory response.⁷⁴ FA 18:2 is an essential fatty acid; it cannot be produced by mammals only obtained from their diet.⁷⁵ For LPC species, localization to airways is evident in the ion images of lipid species with a higher degree of unsaturation comparable to the localization patterns of similar PC species indicating further the role the headgroup plays in localization. MG species reflect similar distribution patterns as DG species and are evenly distributed throughout the tissue. These results indicate that FA distributions are not correlated with the distributions of unsaturated lipids localized to airways.

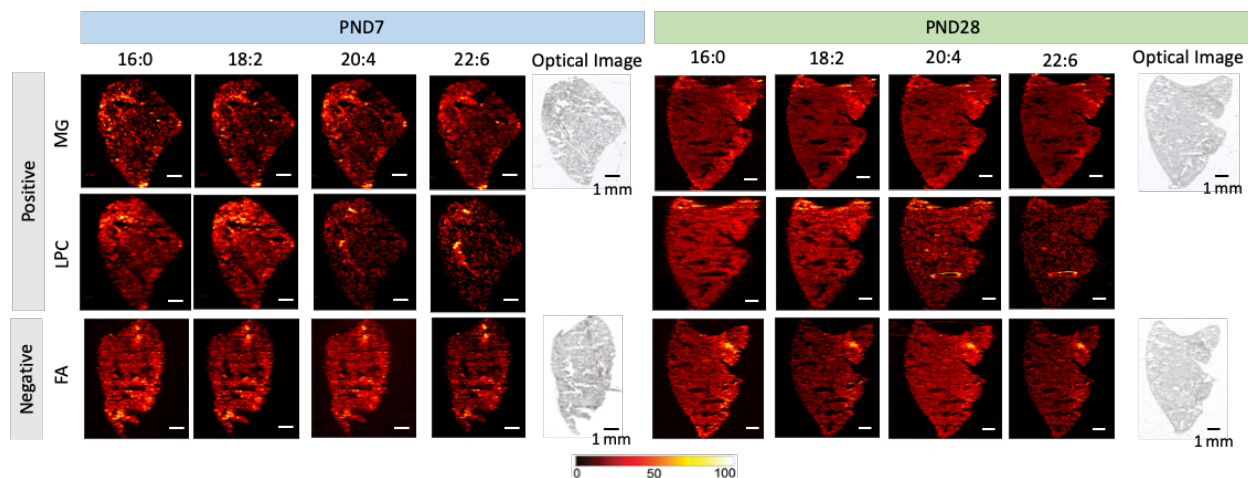


Figure 3.5 Other lipid species that were analyzed were MG, LPC, and FA. PND7 and PND28 samples were compared and biologically relevant lipid chains were selected. For MG and FA lipids in both developmental stages the lipids are alveolar localized regardless of degree of unsaturation. LPC species, however follow the PC trend seen earlier. LPC lipids with a higher degree of unsaturation localize around airways whereas lower degrees of unsaturation, the lipids are alveolar localized. Scale bar indicates 1 mm. Intensity scale (0% black, 100% white) represents signal intensity of individual peaks normalized to the maximum value in each image. Positive mode ion images were normalized to LPC 19:0 and negative mode ion images were normalized to TIC.

3.5 Conclusion

We used nano-DESI MSI to examine localization patterns of lipids in mouse lung tissues at different stages of lung development. Embryonic lung tissue samples (E18.5) contain structurally important or surfactant-related lipids, mostly corresponding to PC species with shorter acyl chain length (~C18) and lower degree of unsaturation (0-2), that are distributed evenly throughout the lung. Consistent with the timeline of lung maturation, during E18.5, surfactant has been produced but not until after birth do the airways expand and alveolarization occurs. After birth, breathing begins and the lung matures further. As the postnatal lung matures, lipids with longer acyl chains (>C20), higher degree of unsaturation (>4), and a variety of headgroups become as abundant as surfactant phospholipids. The phospholipid species that contain PUFAs are present in the alveolar regions of the lungs consistent with being structural lipids. However, a substantial enhancement of unsaturated PC, PI, and PE species along the airways indicate their important role in anti-inflammatory response of maturing lungs. As the lung matures, the lipid composition changes to sustain functionality. In preparation for birth, surfactant production and storage occur in later embryonic stages, and postnatal development results in more lipids associated with immune response due to breathing.

CHAPTER 4. MASS SPECTROMETRY IMAGING OF DICLOFENAC AND ITS METABOLITES IN TISSUES USING NANO-DESI

4.1 Abstract

Glucuronidation is a common metabolic process for drugs and xenobiotics to increase their solubility for excretion. Acyl-glucuronides (glucuronides of carboxylic acids) present concerns of toxicity as they have been implicated in gastrointestinal toxicity and hepatic failure. Despite the substantial success in the bulk analysis of these species, little is known about their localization in tissues. Herein, we used mass spectrometry imaging (MSI) to examine the localization of diclofenac, a widely used nonsteroidal anti-inflammatory drug, and its metabolites in mouse kidney and liver tissues. In particular, Nanospray desorption electrospray Ionization MSI (nano-DESI-MSI) was used for imaging of diclofenac, acyl-glucuronide, and hydroxydiclofenac, in both liver and kidney tissues of mice dosed with diclofenac. Nano-DESI allows for label-free imaging with high spatial resolution and sensitivity without special sample pretreatment. Using nano-DESI-MSI, ion images for diclofenac and its major metabolites were produced. In the kidney, acyl-glucuronide is localized to the inner medulla and hydroxydiclofenac is localized to the cortex. The distributions observed for both metabolites are consistent with the body's normal metabolism and preparing the drug for excretion. The localization patterns align with the presence of enzymes that process diclofenac into its respective metabolites. Full MS images of liver reveal a uniform distribution of diclofenac, but very low signal is observed for the metabolites. Selected ion monitoring (SIM) scan filters were applied during imaging experiments to focus on ions of interest. SIM imaging of liver reveals the acyl-glucuronide metabolite that is evenly distributed throughout the liver tissue.

4.2 Introduction

Diclofenac is a nonsteroidal anti-inflammatory drug typically used to treat pain and inflammation.⁷⁶⁻⁸³ The three major metabolites of diclofenac are 4'-hydroxydiclofenac, 5-hydroxydiclofenac, and the acyl glucuronide.⁷⁶⁻⁸⁰ Diclofenac is metabolized by a class of cytochrome P450 enzymes to produce both hydroxydiclofenac metabolites. The acyl glucuronide is produced from the metabolism of diclofenac by a phase II metabolism uridine diphosphate glucuronosyl transferase (UGT).^{78,84-86} These bio-transformations are necessary in order to

expedite drug elimination through bile and urine by increasing their water solubility.^{87,88} However, the quinone-imine intermediates of the hydroxy metabolites and acyl glucuronide have been linked to hepatotoxicity and gastrointestinal toxicity in humans and rats.^{77,78,80,82–86,89}

Concentrations of diclofenac and its metabolites in plasma^{79,90,91} and urine^{7,15} have been determined by liquid chromatography tandem mass spectrometry (LC-MS/MS) previously. With LC analysis, the isomeric 4'- and 5-hydroxy metabolites have been separated.^{79,82} Furthermore, direct infusion followed by electron-induced dissociation (EID) has recently been used to identify both isomers based on the diagnostic fragments.⁸⁰ Glucuronide metabolites have been analyzed using LC-MS/MS and quantified using the characteristic neutral loss of 176, corresponding to the loss of the sugar moiety^{87,93}. Although LC-MS/MS enables the identification and quantification of diclofenac and its metabolites in tissues it cannot be used for examining their localization within the tissue sections.

Quantitative whole-body autoradiography (QWBA) is the standard method for determining the distribution of drugs in tissues.^{94–98} However, QWBA requires radio-labeling of the compound of interest and this technique does not provide molecular information. Therefore, the metabolites or possible degradation products cannot be distinguished from the precursor compound. If the radiolabel was lost during the metabolism process, these metabolites cannot be detected.^{94,95,98} A QWBA study was done to determine the distribution of [¹⁴C]diclofenac in rats. The highest concentration of radio-labelled drug after 1 hour was located in the bile, followed by the esophagus, kidney, and liver.⁸¹

To overcome the limitations of QWBA imaging, mass spectrometry imaging (MSI) has been implemented to determine drug and metabolite distributions in tissues.^{94,98–100} MSI is a label-free technique that enables spatial localization of hundreds of molecules in tissues.^{101–104} Matrix assisted laser desorption ionization (MALDI) and desorption electrospray ionization (DESI) are by far the most commonly used ionization techniques in MSI experiments.^{98–100,103} Both MALDI and DESI have been used for imaging of drugs in tissue sections.^{99,105–110} However, some drugs including diclofenac have presented a challenge to MALDI MSI.¹¹¹

We have developed nanospray desorption electrospray ionization¹² (nano-DESI), a sensitive ambient ionization technique for MSI.¹⁵ Similar to DESI, this is a soft ionization technique that does not require sample pretreatment. In nano-DESI, the sample is probed using a liquid bridge formed between two capillaries and the extracted molecules are transferred to a mass spectrometer for analysis.^{15,68} The solvent supplied is typically 9:1 MeOH/H₂O but can be changed in order to increase extraction efficiency.¹¹² Furthermore, quantitative imaging has been demonstrated by adding internal standards to the solvent. With pulled capillaries, a spatial resolution of ~10 μm can be achieved.^{17,113} Herein, we explore the capabilities of nano-DESI MSI for imaging of diclofenac and its metabolites in both kidney and liver tissues of dosed mice.

4.3 Experimental

4.3.1 Reagents

Diclofenac was purchased from Sigma (St. Louis, MO). Diclofenac-d₄ (Cayman Chemical, Ann Arbor, MI) and arachidonic acid-d₈ (Sigma) were used as internal standards for negative mode nano-DESI MSI experiments. HPLC grade methanol and water for nano-DESI analysis and HPLC grade water and acetonitrile with 0.1% formic acid for LC analysis were purchased from Fisher Scientific (Hampton, NH).

4.3.2 Tissue Collection and Handling

Female C57BL/6 JAX mice were orally dosed with 15 mg/kg of diclofenac. Diclofenac dosage solution was prepared by dissolving 2 mg/mL of diclofenac in water. Mice were sacrificed after 30 minutes by CO₂ asphyxiation. All animal experiments were performed according to the institutional guidelines of Merck & Co., Inc. Liver and kidney were snap frozen in hexane/dry ice bath, stored in -80 freezer. Tissues were sectioned (thickness = 12 μm) using a Leica CM3050 S cryostat (Leica Biosystems, Buffalo Grove, IL). Sections were thaw-mounted onto glass slides for the imaging experiments and stored in a -80°C freezer until the analysis

4.3.3 LC-MS/MS

Stock solutions diclofenac, hydroxydiclofenac, and acyl-glucuronide were diluted with 50/50 ACN/H₂O with 0.1% formic acid to create calibration standards ranging from 5 μM to 1 nM (Table

B1). Diclofenac-d4 (50 nM) was used as an internal standard for quantitation and added to each tissue section before extraction. C57/B6 mice liver and kidney tissue were extracted in a 2.0 mL Protein LoBind Tube (Eppendorf, Hamburg, Germany) using 50/50 ACN/H₂O with 0.1% formic acid plus x1 protease inhibitor at the ratio of tissue:extraction buffer (w/v as 1:10; e.g. 200 mg tissue:2000 μ L extraction buffer). The tissue and extraction buffer mixture were sonicated in a water bath at 37°C for 30 minutes followed by centrifugation (10,000 RPM for 10 minutes at 4°C). The supernatant was transferred to a clean vial to be analyzed via LC-MS/MS.

LC-MS/MS analyses were conducted using a Transcend LX2 UPLC (Thermo Fisher Scientific, Waltham, MA) system coupled to a QTRAP tandem mass spectrometer (Sciex, Framingham, MA). Ions were produced using electrospray ionization (ESI) on the QTRAP operated in positive mode. The chromatographic separation was achieved using an HSS T3 (2.1 x 50 mm, 2.5 μ m) column (Waters, Milford, MA). The mobile phases consisted of 0.1% formic acid in water (mobile phase A) and 0.1% formic acid in methanol (mobile phase B). Gradient elution was as follows: 0-0.25 min 95% A, 5% B; 0.25–1.75 min linear gradient to 5% A, 95% B; 1.75–2.25 min 5% A, 95% B; 2.25–2.5 min equilibrate with 95% A, 5% B and then hold for 0.5 min at 95% A, 5% B. In each experiment, 5 μ L of a sample was injected at a flow rate of 0.75 mL/min. The multiple reaction monitoring (MRM) transitions for diclofenac, hydroxy metabolite, acyl glucuronide metabolite, and diclofenac-d4 (internal standard) are listed in Table B2.

4.3.4 Nano-DESI Imaging

A custom nano-DESI source⁶⁸ with shear force microscopy¹⁶ capability was interfaced to a Q-Exactive HF-X MS (Thermo Fisher Scientific, Waltham, MA). The nano-DESI probe consisted of two 150 μ m OD x 50 μ m ID fused silica capillaries. The primary capillary delivers the extraction solvent (9:1 methanol/water) to the sample and a secondary capillary transfers the extracted molecules to the MS inlet. A third capillary is used as the shear force probe that maintains a constant distance between the nano-DESI probe and the sample.¹⁷ The shear force capillary (800 μ m OD x 200 μ m ID) was pulled to a 20 μ m OD tip using a P-2000 micropipette puller system (Sutter Instruments, Novato, CA). All capillaries were positioned using high-resolution micromanipulators (XYZ 500MIM, Quater Research and Development, Bend, OR) and monitored using two Dino-Lite digital microscopes (AnMo Electronics Corporation, Sanchong, New Taipei, Taiwan). The 9:1 methanol/water extraction solvent contained internal standards for negative

ionization mode. Negative mode internal standards include arachidonic acid-d8 and diclofenac-d4 (0.5 μ M). The solvent flow rate was 500 nL/min with a voltage of 3.2 kV. The capillary inlet was heated to 250°C. The funnel RF level was optimized to minimize in-source fragmentation and set to 20. Imaging experiments were performed by scanning each sample line by line under the shear force/nano-DESI probe at a constant velocity of 40 μ m/s while collecting high-resolution mass spectra ($m/\Delta m$ of 60,000) at a rate of 7 Hz; The spacing between the lines was 150 μ m setting the upper limit of the spatial resolution to 150 μ m. We note that because the pixel size in the x-dimension is much smaller (\sim 10 μ m), the spatial resolution achieved in these experiments is better than 150 μ m.

4.3.5 Data Processing

Diclofenac and its metabolites observed in the MSI experiments were identified based on the accurate mass measurement and MS/MS. Raw data were collected using Xcalibur software (Thermo Scientific) and subsequently processed using Peak-by-Peak (SpectroSwiss, Lausanne, Switzerland).

4.4 Results and Discussion

In this study, the spatial localization of diclofenac and its major metabolites in kidney and liver tissue were examined. The nano-DESI MSI setup is shown schematically in Figure 4.1A. The primary and secondary capillary are positioned close to each other to generate a stable liquid bridge. The primary capillary supplies solvent to the liquid bridge at a constant rate. Analytes extracted into the liquid bridge are transferred through the secondary capillary to a mass spectrometer inlet and ionized by ESI. The shear force probe maintains a constant distance between the sample and the nano-DESI probe. The inset image shows a photograph of the probe placed on kidney tissue. Figure 4.1B shows the mass spectrum of the dosed kidney tissue. in the m/z 150-500 range. This m/z range encompasses diclofenac, its major metabolites, and endogenous fatty acids from the tissue. Figures 4.1C and 4.1D highlight two m/z ranges (m/z 290-315 and m/z 460-480) containing diclofenac ($[M-H]^-$, m/z 294.0098), diclofenac-d4 ($[M-H]^-$ m/z 298.0348), hydroxydiclofenac ($[M-H]^-$ m/z 310.0048) and the acyl glucuronide metabolite ($[M-H]^-$ m/z 470.0424).

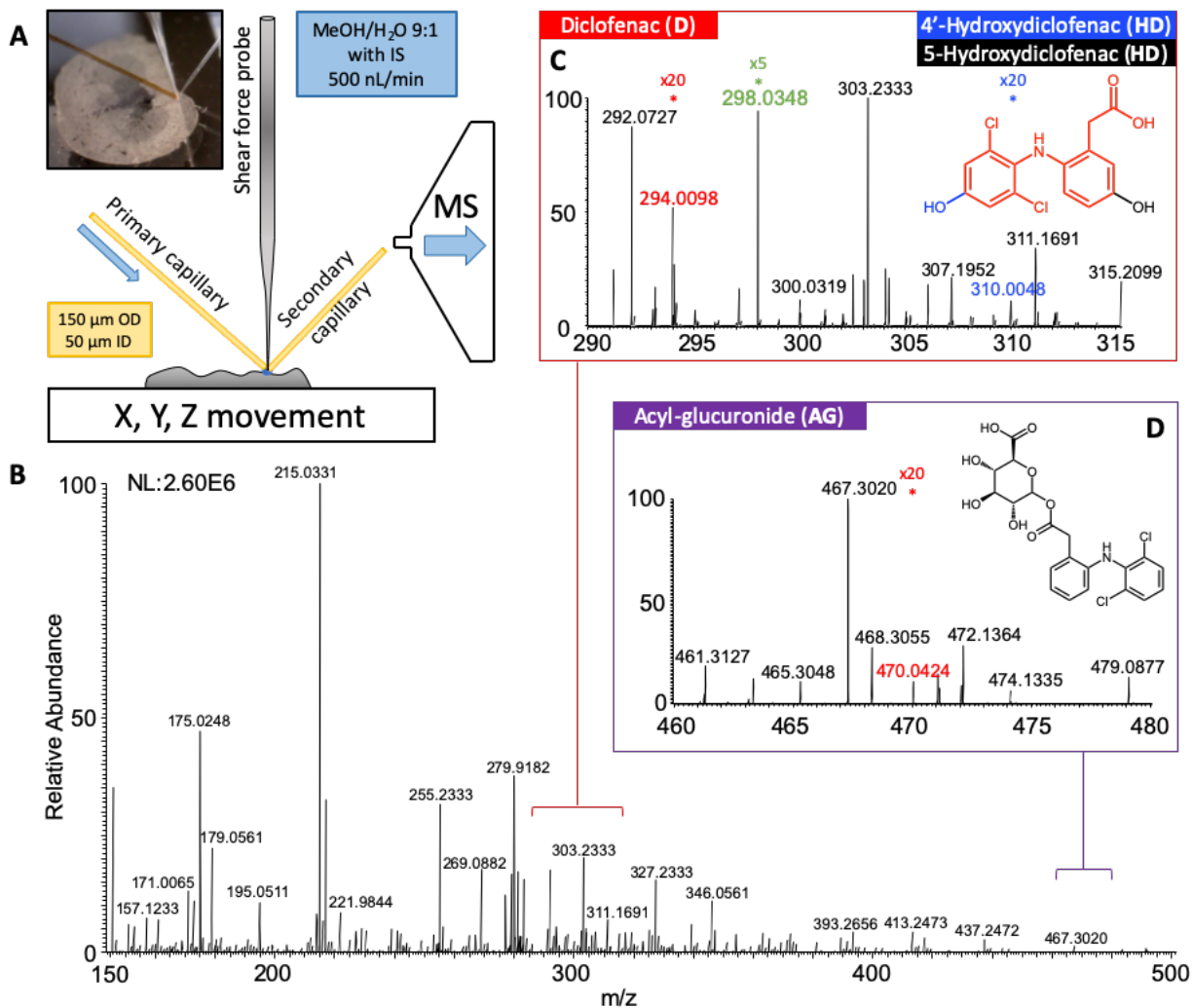


Figure 4.1 (A) Schematic drawing of the nano-DESI system positioned in front of a mass spectrometer inlet showing the nano-DESI probe comprised of two fused silica capillaries for solvent delivery and ESI, and a shear force capillary for maintaining constant distance between the sample and probe. (B) Negative ion mode mass spectrum of diclofenac dosed mouse kidney tissue in the m/z 150-500 range. (C) Expanded view of the m/z 290-315 range. Diclofenac (red, m/z 294), diclofenac-d4 (green, m/z 298), 4'- and 5-hydroxydiclofenac (blue, m/z 310) are present. The inset structure corresponds to diclofenac (red) with additional modifications for 4'-hydroxydiclofenac (blue, 4' carbon -OH group) and 5-hydroxydiclofenac (black, 5 carbon -OH group). (D) Expanded view of the m/z 460-480 range. The structure of the acyl glucuronide metabolite (red, m/z 470) is shown in inset

Although nano-DESI is a soft ionization technique, in our initial experiments, we observed substantial fragmentation of diclofenac-d4. Similar fragmentation was observed in direct infusion experiments and attributed to in-source fragmentation of the analyte. Upon further investigation of the instrument conditions we found that in-source fragmentation could be minimized by

adjusting the funnel RF level of the Q-Exactive HF-X system. Using the default funnel RF setting of 100, we observed predominately the decarboxylated fragment of diclofenac-d4 (m/z 254.0440) (Figure B1A). When the funnel RF was adjusted to 0, very little fragmentation occurs and the intact $[M-H]^-$ peak (m/z 298.0337) for diclofenac-d4 is observed with high intensity (Figure B1B). However, ion transmission at $RF=0$ is fairly low. The funnel RF level was further optimized by monitoring the signal-to-noise ratio of diclofenac-d4 and its fragment while varying the funnel RF from 0 to 100 (Figure B1C). We found that the funnel RF level of 20 provided the best signal of diclofenac-d4 without any measurable in-source fragmentation.

Diclofenac dosed kidney tissue was imaged using nano-DESI MSI. The resulting ion images as well as H&E and optical images are shown in Figure 4.2. The H&E stained image was annotated to highlight important anatomical regions. For both left and right kidney sections, diclofenac has an even distribution throughout the tissue. The acyl glucuronide metabolite is tightly localized to the inner medulla of the kidney, but some signal can be seen in the cortex region. UGT enzymes that catalyze glucuronidation are present in both the medulla and cortex of the kidney.¹¹⁴⁻¹¹⁶ Due to their polar nature and increased solubility, glucuronides are excreted through urine or bile.¹¹⁶ Therefore, the enhanced abundance of the acyl glucuronide in medulla most likely indicates that the metabolite is concentrated in this region preparation for removal. In contrast, hydroxydiclofenac is localized to the cortex of the kidney. Cytochrome P-450 enzymes catalyze oxidative reactions including aromatic hydroxylation.⁸⁸ This class of enzymes is responsible for the metabolism of diclofenac to form 4'- and 5-hydroxydiclofenac. In a study conducted with rabbit kidney, the highest level of cytochrome P-450 was present in the kidney cortex and not detected in the medulla.^{88,117} The localization pattern of hydroxydiclofenac in mouse kidney observed in this study is consistent with the enhanced abundance of cytochrome P-450 in this region reported in the literature. The localization patterns for diclofenac and its metabolites are consistent across the left and right kidney and across replicate tissue sections as seen in Figure B2.

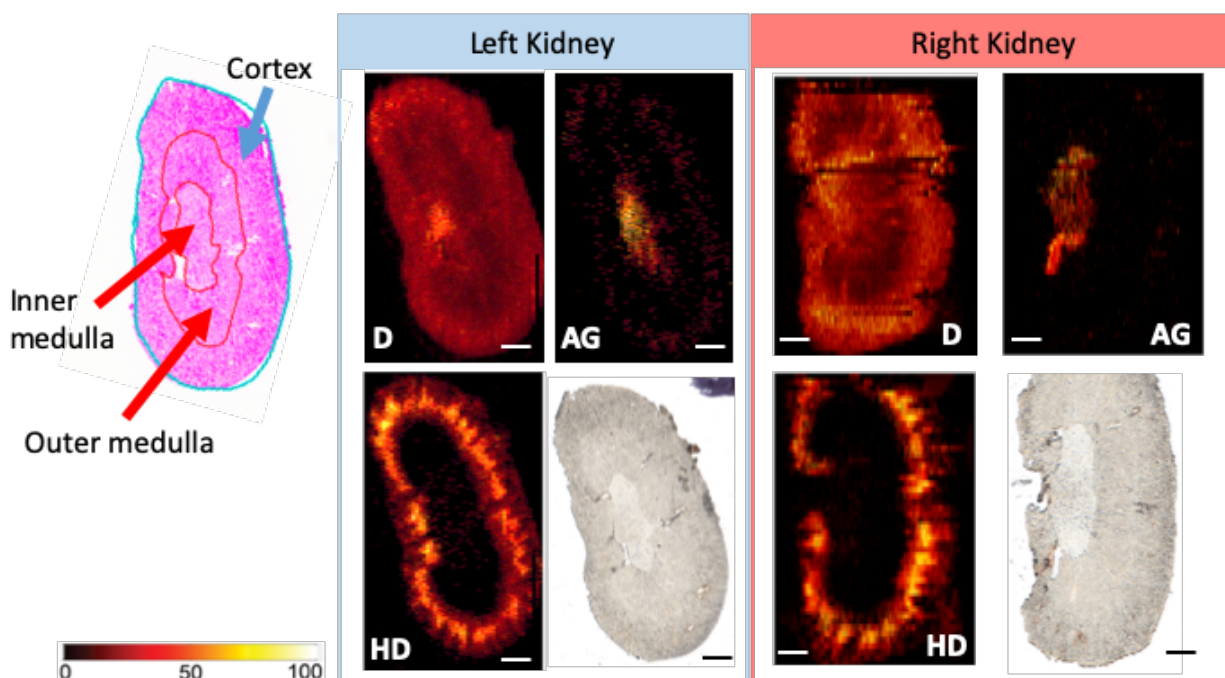


Figure 4.2 H&E, optical, and nano-DESI ion images of diclofenac dosed mouse kidney tissue. Relevant regions of H&E stained kidney section are annotated for comparison with ion images. Ion images of diclofenac (D), acyl glucuronide (AG), and hydroxydiclofenac (HD) are shown for both left and right kidney to demonstrate the reproducibility of nano-DESI MSI. Ion images are self-normalized to the internal standard, diclofenac-d4. Scale bar represents 1 mm. Intensity scale ranges from 0% intensity (black) to 100% (white).

Dosed mouse liver tissue was also imaged. The resulting ion images as well as corresponding optical images are shown in Figure 4.3. Similar to the kidney tissue, diclofenac is uniformly distributed across the liver tissue section. Liver is the main location for drug metabolism and both cytochrome P-450 and UGT enzymes are present in liver cells.^{118,119} However, ion images of both hydroxydiclofenac and acyl glucuronide metabolites show very low signal. These images are consistent across multiple tissue section replicates (Figure B3). Based on previous literature, hydroxydiclofenac and acyl glucuronide metabolites were expected in liver. Since very little signal intensity was seen in the ion images, LC-MS/MS quantitation was performed to determine if the concentration of these metabolites was below the limit of detection. Table 4.1 shows the concentration of diclofenac and its metabolites in both kidney and liver tissue determined by LC-MS/MS quantitation. The concentration of the acyl glucuronide metabolite in liver (avg. 2.5 μM) and kidney (avg. 3.27 μM) are similar. Hydroxydiclofenac was not stable in kidney tissue homogenate and could not be accurately quantified. In the liver, the average concentration of hydroxydiclofenac was 0.95 μM .

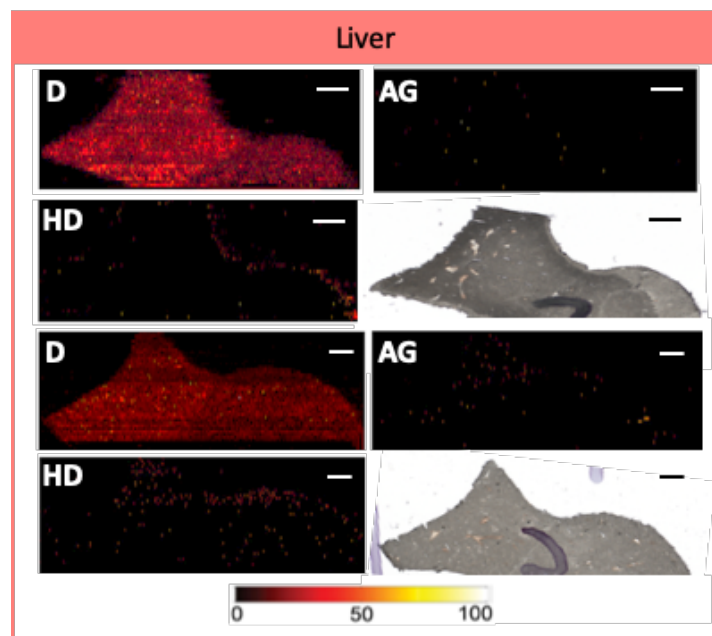


Figure 4.3 Optical and nano-DESI ion images of diclofenac dosed mouse liver tissue. Ion images of diclofenac (D), acyl glucuronide (AG), and hydroxydiclofenac (HD) are shown for two different liver sections. Ion images are self-normalized to internal standard, diclofenac-d4. Scale bar represents 1 mm. Intensity scale ranges from 0% intensity (black) to 100% (white)

Table 4.1 Concentrations of diclofenac and its major metabolites in kidney (DK) and liver (DL) tissue from LC-MS/MS quantitative method. Dosed tissue samples (DK 4-6, DL 4-6) and control tissues (DL 1-3, DK 1-3) were ran in triplicate. Hydroxydiclofenac was not stable in kidney tissue homogenate and could not be accurately quantified but significant amount was observed (N/A). BLQ: Below limit of quantitation.

C57/BL6 Mouse Kidney Tissue				
Label	Tissue (mg)	Diclofenac concentration (μM)	Hydroxydiclofenac concentration (μM)	Diclofenac-acyl- β -D-glucuronide concentration (μM)
DK 4	2.36	12.25	N/A	2.71
DK 5	2.43	14.38	N/A	3.43
DK 6	2.55	16.14	N/A	3.67
DL 1	1.8	BLQ	N/A	BLQ
DL 2	1.77	BLQ	N/A	BLQ
DL 3	1.14	BLQ	N/A	BLQ

C57/BL6 Mouse Liver Tissue				
Label	Tissue (mg)	Diclofenac concentration (μM)	Hydroxydiclofenac concentration (μM)	Diclofenac-acyl- β -D-glucuronide concentration (μM)
DL 4	2.64	22.54	1.35	2.41
DL 5	2.75	18.08	0.55	2.42
DL 6	2.91	24.38	0.95	2.67
DK 1	4.15	BLQ	BLQ	BLQ
DK 2	3.76	BLQ	BLQ	BLQ
DK 3	3.84	BLQ	BLQ	BLQ

The concentrations determined from LC quantitation for acyl glucuronide for both kidney and liver were on the same order of magnitude, so it is unlikely that the low signal in the liver ion images is below the limit of detection. Based on the full MS spectrum of dosed liver tissue, the low signal intensity for the metabolites is likely due to signal suppression from biological species that ionize more readily in the same m/z range, such as fatty acids and bile acids. To increase signal-to-noise for diclofenac and its metabolites a selected ion monitoring (SIM) instrument method was developed. This method applies three scan filters that narrow the m/z range around diclofenac and the two metabolites to specifically monitor their m/z value and remove other signals. The SIM method was used during the imaging experiment for kidney and liver tissue (**Figure 4**). Kidney tissue was imaged to confirm the distribution of metabolites obtained using the full m/z range for imaging. SIM ion images obtained for hydroxydiclofenac and acyl glucuronide are comparable to full MS images, but the signal intensity has improved. For liver tissue sections, the ion images reveal both hydroxydiclofenac and acyl-glucuronide metabolites are present. Both metabolites are mostly distributed evenly but have several bright spots colocalized with hepatic veins.

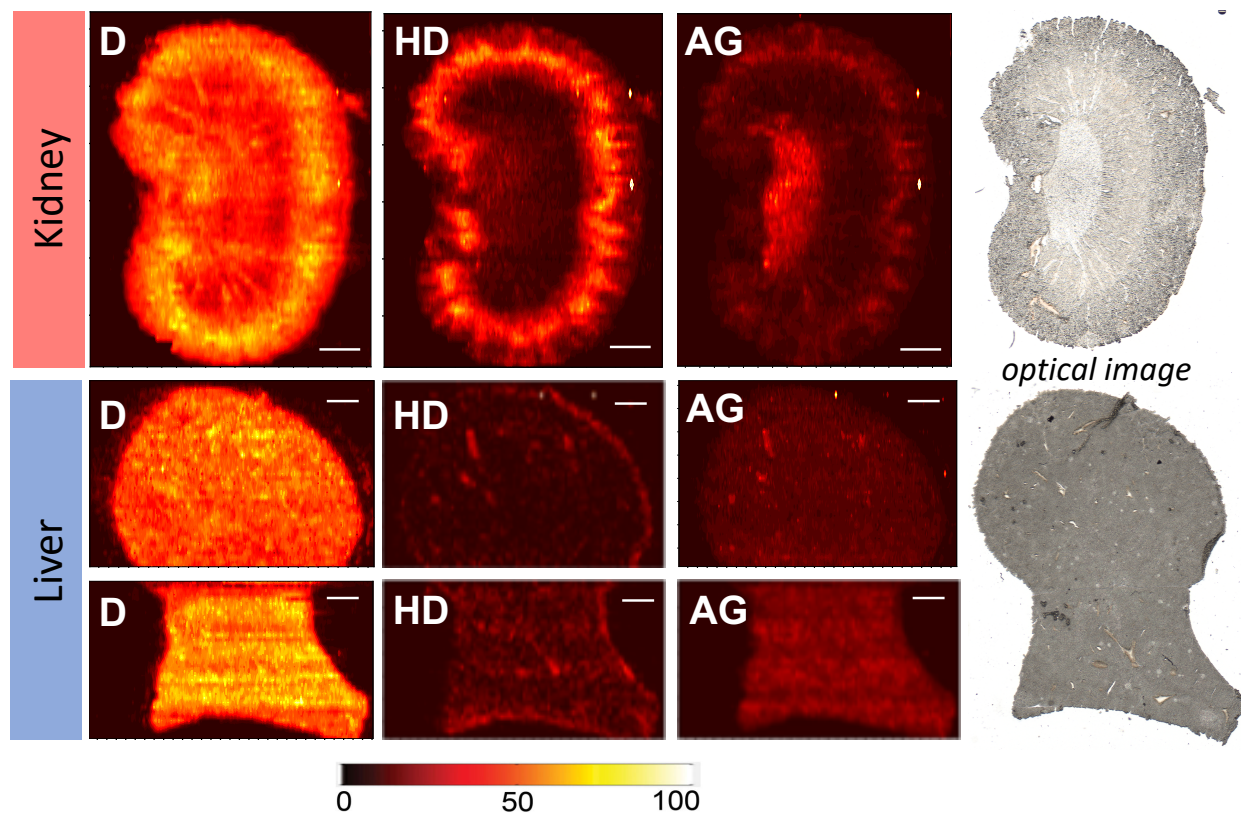


Figure 4.4 Optical and nano-DESI SIM mode ion images of dosed kidney and liver tissue. Ion images of diclofenac (D; center m/z 294, width 10), acyl glucuronide (AG; center m/z 470, width 10), and hydroxydiclofenac (HD; center m/z 310, width 10) were collected using SIM windows centered on respective m/z values. Ion images are self-normalized. Scale bar represents 1 mm. Intensity scale ranges from 0% intensity (black) to 100% (white).

4.5 Conclusion

Nano-DESI MSI was used to image diclofenac dosed liver and kidney tissues from mice. These experiments were to evaluate this technique for drug and metabolite imaging. Diclofenac and its three major metabolites were successfully imaged in kidney tissue, however in liver only diclofenac was able to be imaged. In the kidney, diclofenac is evenly distributed throughout the tissue. Hydroxydiclofenac is localized to the cortex of the kidney where the majority of cytochrome P450 enzymes are that metabolize diclofenac into hydroxydiclofenac. The acyl-glucuronide metabolite is localized to the inner medulla of the kidney which is the area of the kidney where xenobiotics are excreted after metabolism. Acyl-glucuronide is more polar compared to hydroxydiclofenac, therefore, it is likely localized here for rapid excretion. These distributions are reproducible across the left and right kidney and across multiple tissue sections. In liver tissue,

diclofenac was also evenly distributed throughout the tissue. However, hydroxydiclofenac and acyl-glucuronide metabolites were not observed in full MS imaging. SIM m/z filters were applied to help reduce ion suppression from other ions and narrow the mass range around the metabolites of interest. SIM images revealed that the acyl-glucuronide metabolite is present and evenly distributed throughout the liver tissue. The hydroxy-metabolite was not observed. Nano-DESI MSI can be applied to determine the distribution of drugs and metabolites in dosed tissues.

APPENDIX A. CHAPTER 3 SUPPLEMENTAL

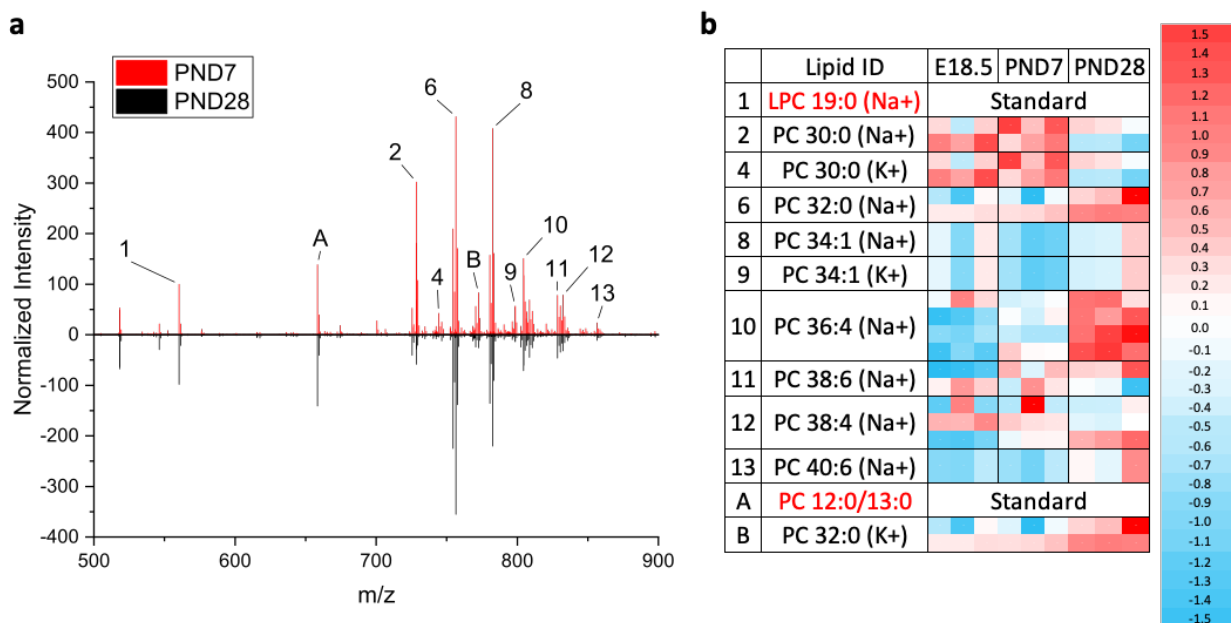


Figure A1. a) Mass spectra of lipid profiles from PND7 and PND28 samples in positive mode. Profile represents average spectrum over whole tissue section with signal intensity normalized to the internal standard LPC 19:0. b) Lipids are identified in the table along with z-scores calculated from acquired lipidomics data. Enriched lipid species are represented by a positive z-score (red).

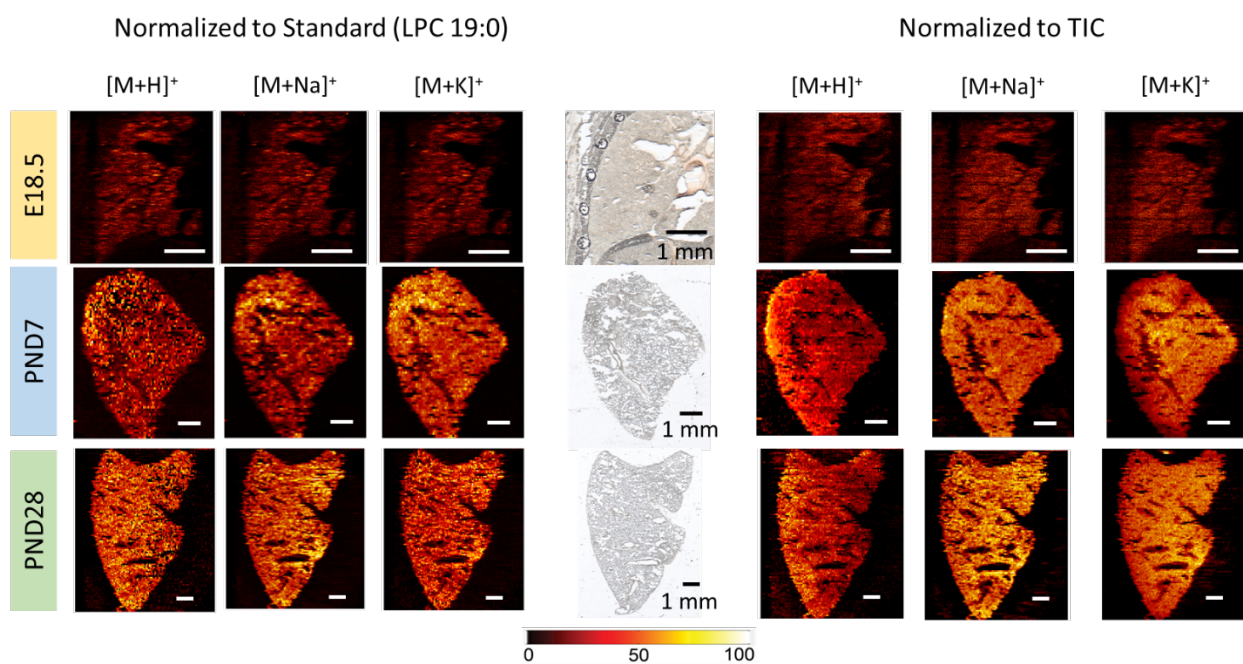
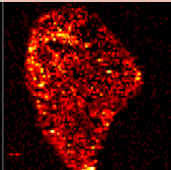
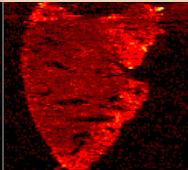
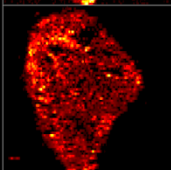
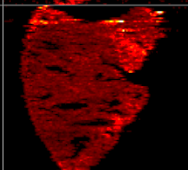
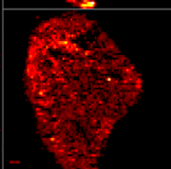
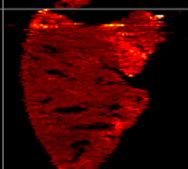
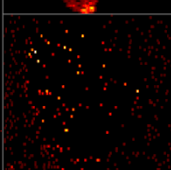
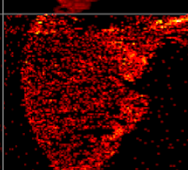
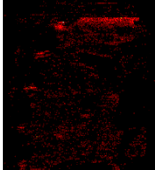
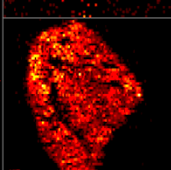
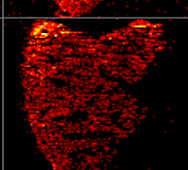
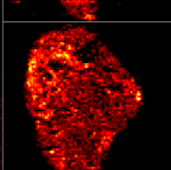
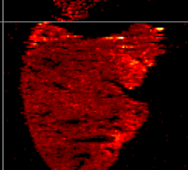
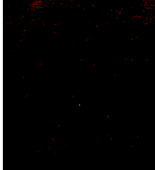
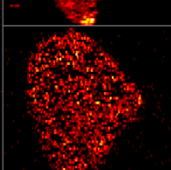
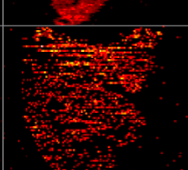
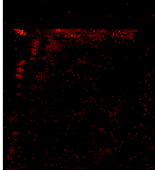
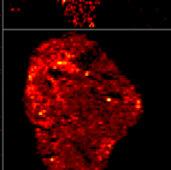
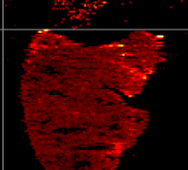
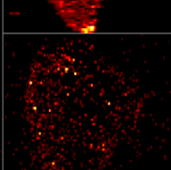
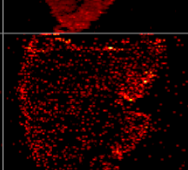
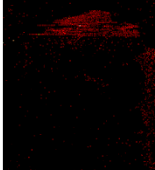
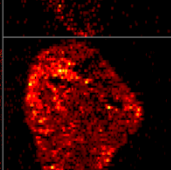
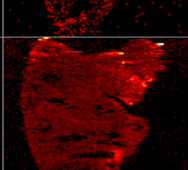


Figure A2. MS ion images for the major surfactant lipid PC 16:0/16:0 are shown for different adducts including $[M+H]^+$, $[M+Na]^+$, and $[M+K]^+$. The optical images are also shown for each sample. Across each adduct the ionization is unaffected by matrix effects. Therefore, for future ion images only the sodiated ion was chosen.

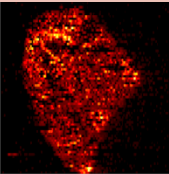
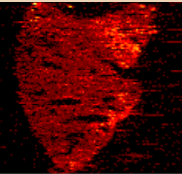
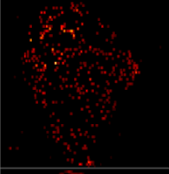
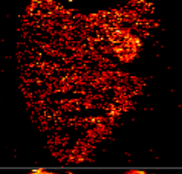
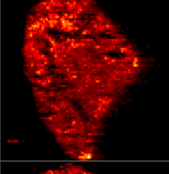
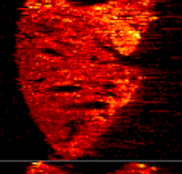
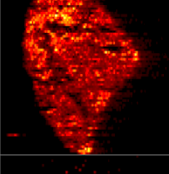
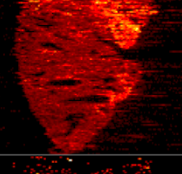
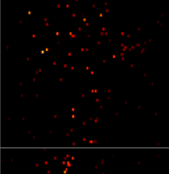
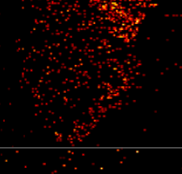
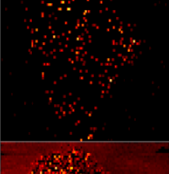
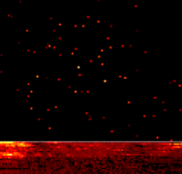
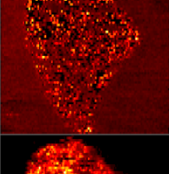
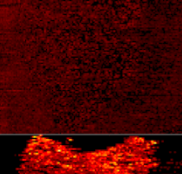
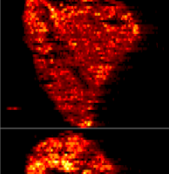
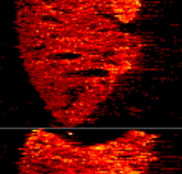
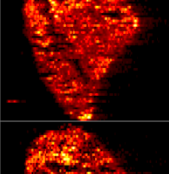
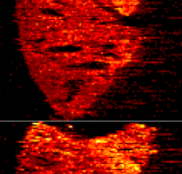
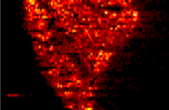
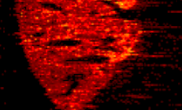
Table A1. Positive mode MS ion images from E18.5, PND7 and PND28. For each ion image, m/z and identification is listed in the table. For replicates of nano-DESI images, see <https://lungmap.net>

E18.5	PND7	PND28	Exact m/z	Name (Sum)	Identification 1
			148.0044	MB	Taurine ; [M+Na] ⁺
			159.0283	MB	Hypoxanthine ; [M+Na] ⁺
			203.0532	MB	Glucose; [M+Na] ⁺
			280.0928	MB	sn-glycero-3-Phosphocholine; [M+Na] ⁺
			291.0706	MB	Inosine; [M+Na] ⁺
			303.2303	FA(18:3)	Linoleic acid; [M+Na] ⁺
			305.2460	FA(18:1)	Oleic Acid; [M+Na] ⁺
			351.2308	FA	Docosahexaenoic acid (DHA); [M+Na] ⁺
			351.2516	MG(16:1)	MG 16:1 ; [M+Na] ⁺
			353.2465	FA(22:5)	FA 22:5; [M+Na] ⁺

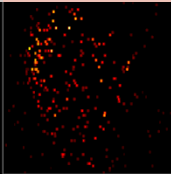
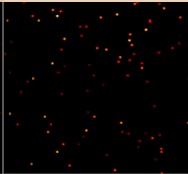
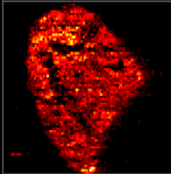
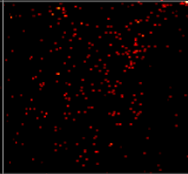
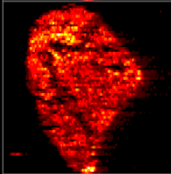
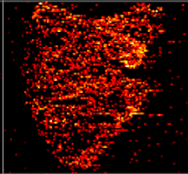
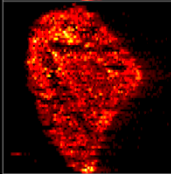
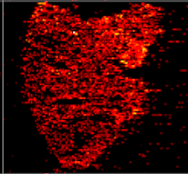
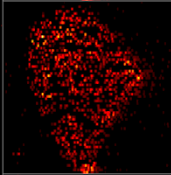
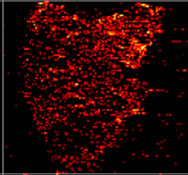
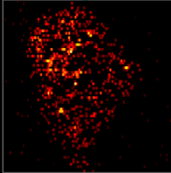
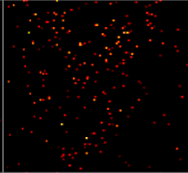
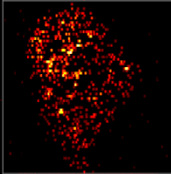
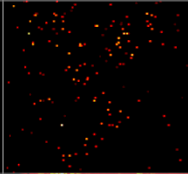
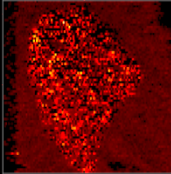
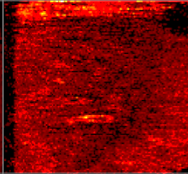
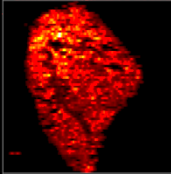
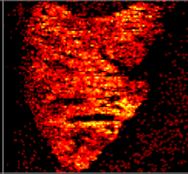
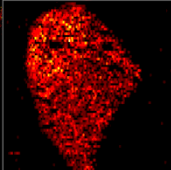
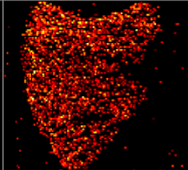
E18.5	PND7	PND28			
			353.2674	MG(16:0)	MG 16:0; [M+Na] ⁺
			377.2674	MG(18:2)	MG 18:2; [M+Na] ⁺
			379.2831	MG(18:1)	MG 18:1; [M+Na] ⁺
			381.2986	MG(18:0)	MG 18:0; [M+Na] ⁺
			400.3436	FA	Palmitoylcarnitine; [M+H] ⁺
			401.2675	MG(20:4)	MG 20:4; [M+Na] ⁺
			409.3454	FA	Tetracosanediol; [M+K] ⁺
			425.2676	MG(22:6)	MG 22:6; [M+Na] ⁺
			427.2679	FA	2-glyceryl-PGD2; [M+H] ⁺
			427.2833	MG(22:5)	MG 22:5; [M+Na] ⁺

E18.5	PND7	PND28			
			429.2990	MG(22:4)	MG 22:4; [M+Na] ⁺
			449.3617	FA	Hexacosanedioic acid; [M+Na] ⁺
			476.2764	PC(13:0)	PC(13:0/0:0); [M+Na] ⁺
			490.2910	PC(14:0)	PC(0:0/14:0); [M+Na] ⁺ PC(16:3/0:0); [M+H] ⁺
			504.3067	PC(15:0)	PC(15:0/0:0); [M+Na] ⁺
			516.3067	PC(16:1)	PC(16:1/0:0); [M+Na] ⁺
			518.3223	PC(16:0)	PC(0:0/16:0); [M+Na] ⁺
			535.4363	DG(30:3)	DG(12:0/18:3/0:0); [M+H] ⁺
			540.3067	PC(18:3)	PC(18:3/0:0); [M+Na] ⁺
			542.3223	PC(18:2)	PC(18:2/0:0); [M+Na] ⁺ PC(20:5/0:0); [M+H] ⁺

E18.5	PND7	PND28			
			544.3377	PC(18:1)	PC(0:0/18:1); [M+Na] ⁺
			546.3536	PC(18:0)	PC(0:0/18:0); [M+Na] ⁺
			548.2755	PE(22:6)	PE(22:6/0:0); [M+Na] ⁺
			548.3716	PC(20:2)	PC(20:2/0:0); [M+H] ⁺
			563.4652	DG(30:0)	DG(14:0/16:0/0:0); [M+Na] ⁺
			566.3223	PC(20:4)	PC(0:0/20:4); [M+Na] ⁺
			568.3380	PC(20:3)	PC(20:3/0:0); [M+Na] ⁺
			587.4652	DG(32:2)	DG(14:0/18:2/0:0); [M+Na] ⁺
			589.4809	DG(32:1)	DG(14:0/18:1/0:0); [M+Na] ⁺ DG(14:0/20:4/0:0); [M+H] ⁺ DG(16:0/16:1/0:0); [M+Na] ⁺
			590.3223	PC(22:6)	PC(22:6/0:0); [M+Na] ⁺

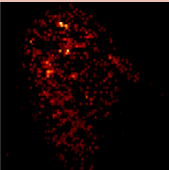
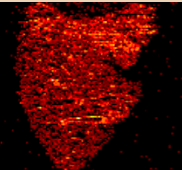
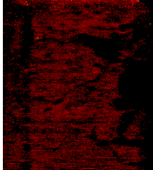
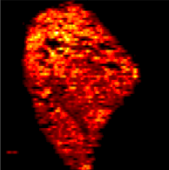
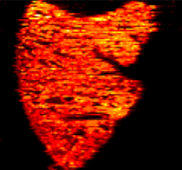
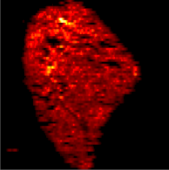
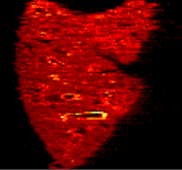
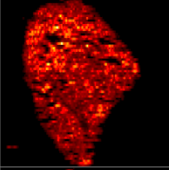
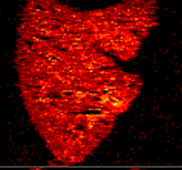
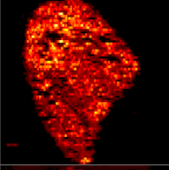
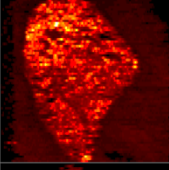
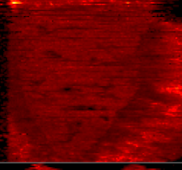
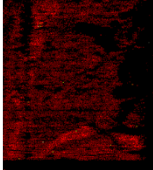
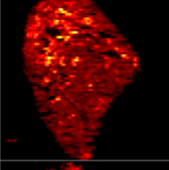
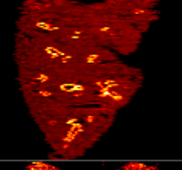
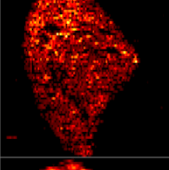
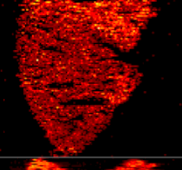
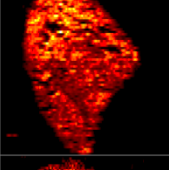
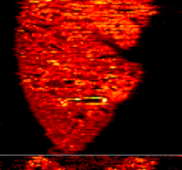
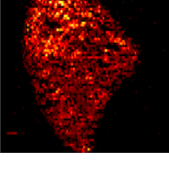
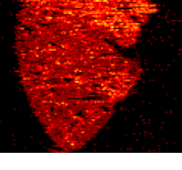
E18.5	PND7	PND28			
			591.4965	DG(32:0)	DG(16:0/0:0/16:0); [M+Na]+
			613.4809	DG(34:3)	DG(16:0/18:3/0:0); [M+Na]+ DG(16:1/18:2/0:0); [M+Na]+
			615.4965	DG(34:2)	DG(16:0/18:2/0:0); [M+Na]+
			617.5122	DG(34:1)	DG(16:0/18:1/0:0); [M+Na]+
			619.5278	DG(34:0)	DG(16:0/18:0/0:0); [M+Na]+
			635.4652	DG(36:6)	DG(14:0/22:6/0:0); [M+Na]+
			637.4809	DG(36:5)	DG(16:0/20:5/0:0); [M+Na]+ DG(18:2/18:3/0:0); [M+Na]+
			639.4965	DG(36:4)	DG(14:0/22:4/0:0); [M+Na]+ DG(18:2/0:0/18:2); [M+Na]+ DG(18:1/18:3/0:0); [M+Na]+ DG(16:0/20:4/0:0); [M+Na]+
			641.5122	DG(36:3)	DG(16:0/20:3/0:0); [M+Na]+ DG(18:1/18:2/0:0); [M+Na]+
			643.5278	DG(36:2)	DG(18:1/0:0/18:1); [M+Na]+

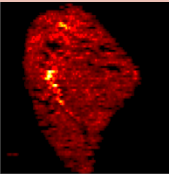
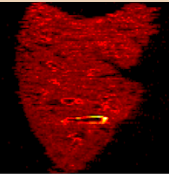
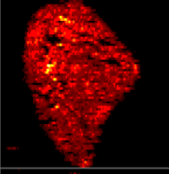
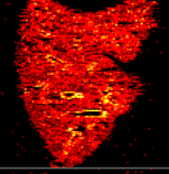
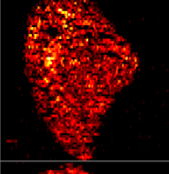
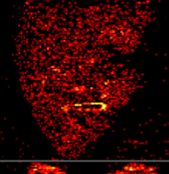
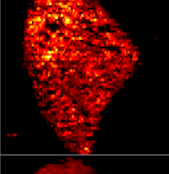
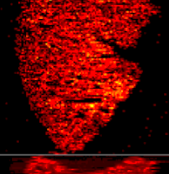
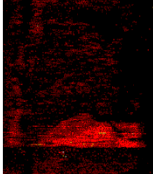
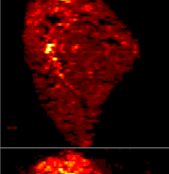
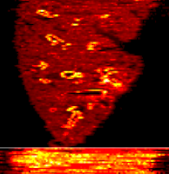
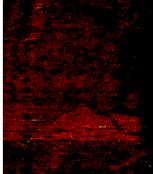
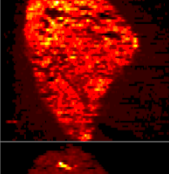
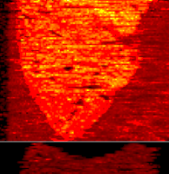
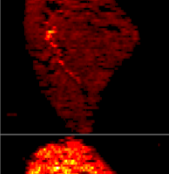
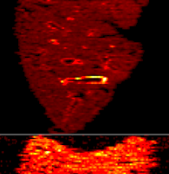
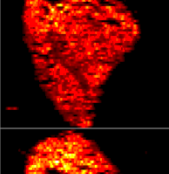
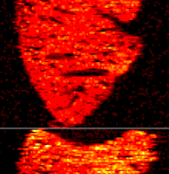
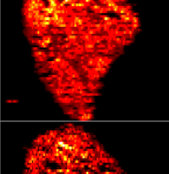
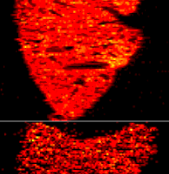
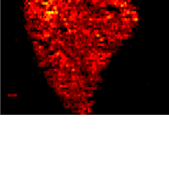
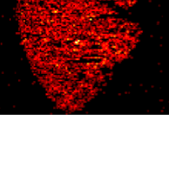
E18.5	PND7	PND28			
			645.4861	DG(35:2)	DG(15:0/20:2/0:0); [M+K]+ DG(17:1/18:1/0:0); [M+K]+ DG(17:0/18:2/0:0); [M+K]+
			645.5435	DG(36:1)	DG(16:0/20:1/0:0); [M+Na]+ DG(18:0/18:1/0:0); [M+Na]+
			647.5017	DG(35:1)	DG(17:0/18:1/0:0); [M+K]+ DG(19:1/16:0/0:0); [M+K]+
			661.4809	DG(38:7)	DG(16:1/22:6/0:0); [M+Na]+
			663.4965	DG(38:6)	DG(16:0/22:6/0:0); [M+Na]+ DG(18:2/20:4/0:0); [M+Na]+ DG(16:1/22:5/0:0); [M+Na]+
			665.5122	DG(38:5)	DG(16:0/22:5/0:0); [M+Na]+ DG(18:1/20:4/0:0); [M+Na]+ DG(18:0/20:5/0:0); [M+Na]+
			667.5278	DG(38:4)	DG(16:0/22:4/0:0); [M+Na]+ DG(18:2/20:2/0:0); [M+Na]+ DG(18:0/20:4/0:0); [M+Na]+
			669.5435	DG(38:3)	DG(18:0/20:3/0:0); [M+Na]+
			670.6115	Cer(42:2)	Cer(d18:1/24:1); [M+Na]+
			672.4217	PC(25:0-CHO)	PC(16:0/9:0(CHO)); [M+Na]+

E18.5	PND7	PND28			
			679.5278	DG(39:5)	DG(17:0/22:5/0:0); [M+Na] ⁺ DG(19:1/20:4/0:0); [M+Na] ⁺
			687.4965	DG(40:8)	DG(18:2/22:6/0:0); [M+Na] ⁺
			689.5122	DG(40:7)	DG(18:1/22:6/0:0); [M+Na] ⁺ DG(18:2/22:5/0:0); [M+Na] ⁺
			691.5278	DG(40:6)	DG(18:1/22:5/0:0); [M+Na] ⁺ DG(20:3/22:6/0:0); [M+H] ⁺ DG(18:2/22:4/0:0); [M+Na] ⁺
			693.5435	DG(40:5)	DG(18:0/22:5/0:0); [M+Na] ⁺ DG(20:3/22:5/0:0); [M+H] ⁺ DG(20:2/22:6/0:0); [M+H] ⁺
			697.5174	DG(39:4)	DG(19:0/20:4/0:0); [M+K] ⁺
			697.5261	SM(32:1)	SM(d16:1/16:0); [M+Na] ⁺ SM(d18:1/14:0); [M+Na] ⁺
			700.4553	PR	adenosylhopane; [M+K] ⁺
			700.4894	PC(28:0)	PC(14:0/14:0); [M+Na] ⁺ PC(16:3/14:0); [M+H] ⁺
			704.5959	Cer(42:1)	Cer(d18:1/24:0(2OH)); [M+K] ⁺

E18.5	PND7	PND28			
			713.5487	DG(40:3)	DG(18:1/22:2/0:0); [M+K]+ DG(20:1/20:2/0:0); [M+K]+ DG(18:2/22:1/0:0); [M+K]+ DG(18:2/22:1/0:0); [M+K]+
			714.5050	PC(29:0)	PC(14:0/15:0); [M+Na]+
			715.5644	DG(40:2)	DG(18:1/22:1/0:0); [M+K]+ DG(20:0/20:2/0:0); [M+K]+
			723.5418	SM(34:2)	SM(d18:2/16:0); [M+Na]+
			725.5574	SM(34:1)	SM(d18:1/16:0); [M+Na]+
			726.5050	PC(30:1)	PC(14:0/16:1); [M+Na]+ PC(16:3/16:1); [M+H]+ PC(16:0/16:4); [M+H]+ PC(12:0/20:4); [M+H]+
			728.5207	PC(30:0)	PC(14:0/16:0); [M+Na]+ PC(16:3/16:0); [M+H]+ PC(14:0/18:3); [M+H]+
			740.5207	PC(31:1)	PC(14:0/17:1); [M+Na]+ PC(15:1/16:0); [M+Na]+ PC(15:0/16:1); [M+Na]+
			742.5363	PC(31:0)	PC(15:0/16:0); [M+Na]+
			752.5207	PC(32:2)	PC(14:0/18:2); [M+Na]+ PC(16:1/16:1); [M+Na]+ PC(16:2/16:0); [M+Na]+ PC(14:0/20:5); [M+H]+ PC(16:1/18:4); [M+H]+

E18.5	PND7	PND28			
			753.5887	SM(36:1)	SM(d18:1/18:0); [M+Na] ⁺
			754.5363	PC(32:1)	PC(14:0/18:1); [M+Na] ⁺ PC(16:0/16:1); [M+Na] ⁺
			756.5520	PC(32:0)	PC(16:0/16:0); [M+Na] ⁺ PC(16:0/18:3); [M+H] ⁺ PC(16:1/18:2); [M+H] ⁺
			758.6471	HexCer(38:0)	HexCer(d18:0/20:0); [M+H] ⁺
			762.4911	PR	bacteriohopane-31,32,33,34-tetrol-35-cyclitol; [M+K] ⁺
			766.5363	PC(33:2)	PC(15:0/18:2); [M+Na] ⁺ PC(15:1/18:1); [M+Na] ⁺
			770.5676	PC(33:0)	PC(16:0/17:0); [M+Na] ⁺
			776.5207	PC(34:4)	PC(14:0/20:4); [M+Na] ⁺
			778.5387	PC(36:6)	PC(14:0/22:6); [M+H] ⁺ PC(16:1/20:5); [M+H] ⁺ PC(18:2/18:4); [M+H] ⁺
			780.5520	PC(34:2)	PC(16:0/18:2); [M+Na] ⁺

E18.5	PND7	PND28			
			781.6200	SM(38:1)	SM(d18:1/20:0); [M+Na] ⁺
			782.5676	PC(34:1)	PC(16:0/18:1); [M+Na] ⁺
			790.5363	PC(35:4)	PC(15:0/20:4); [M+Na] ⁺
			794.5676	PC(35:2)	PC(17:0/18:2); [M+Na] ⁺ PC(17:1/18:1); [M+Na] ⁺
			796.5833	PC(35:1)	PC(17:0/18:1); [M+Na] ⁺
			802.5363	PC(36:5)	PC(14:0/22:5); [M+Na] ⁺ PC(16:0/20:5); [M+Na] ⁺ PC(16:1/20:4); [M+Na] ⁺ PC(18:2/18:3); [M+Na] ⁺
			804.5520	PC(36:4)	PC(14:0/22:4); [M+Na] ⁺ PC(16:0/20:4); [M+Na] ⁺ PC(18:2/18:2); [M+Na] ⁺
			807.6357	SM(40:2)	SM(d18:1/22:1); [M+Na] ⁺ SM(d18:2/22:0); [M+Na] ⁺
			808.5833	PC(36:2)	PC(18:0/18:2); [M+Na] ⁺
			809.6513	SM(40:1)	SM(d18:1/22:0); [M+Na] ⁺

E18.5	PND7	PND28			
			814.5363	PC(37:6)	PC(15:0/22:6); [M+Na] ⁺
			818.5700	PC(39:7)	PC(17:1/22:6); [M+H] ⁺
			820.5856	PC(39:6)	PC(17:0/22:6); [M+H] ⁺
			826.5363	PC(38:7)	PC(16:1/22:6); [M+Na] ⁺ PC(18:2/20:5); [M+Na] ⁺ PC(18:3/20:4); [M+Na] ⁺
			828.5520	PC(38:6)	PC(16:0/22:6); [M+Na] ⁺ PC(16:1/22:5); [M+Na] ⁺ PC(18:1/20:5); [M+Na] ⁺ PC(18:2/20:4); [M+Na] ⁺ PC(18:3/22:6); [M+H] ⁺ PC(20:4/20:5); [M+H] ⁺
			830.5676	PC(38:5)	PC(16:0/22:5); [M+Na] ⁺ PC(18:0/20:5); [M+Na] ⁺ PC(18:1/20:4); [M+Na] ⁺
			832.5833	PC(38:4)	PC(16:0/22:4); [M+Na] ⁺ PC(18:0/20:4); [M+Na] ⁺ PC(18:1/20:3); [M+Na] ⁺
			833.6513	SM(42:3)	SM(d18:2/24:1); [M+Na] ⁺
			835.6670	SM(42:2)	SM(d18:1/24:1); [M+Na] ⁺
			836.6169	PC(40:5)	PC(18:0/22:5); [M+H] ⁺ PC(20:0/20:5); [M+H] ⁺ PC(20:1/20:4); [M+H] ⁺

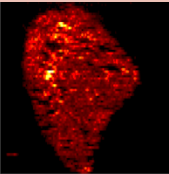
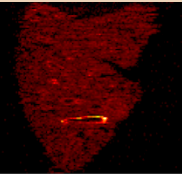
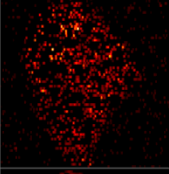
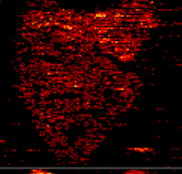
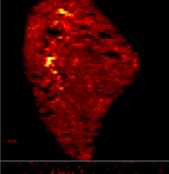
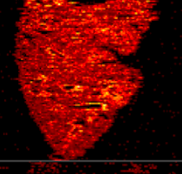
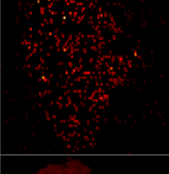
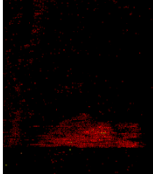
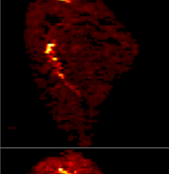
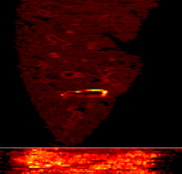
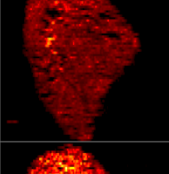
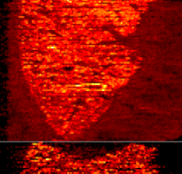
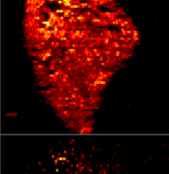
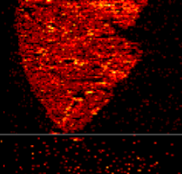
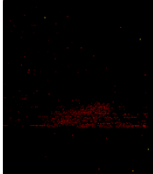
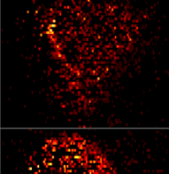
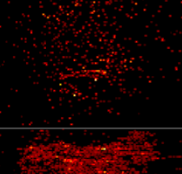
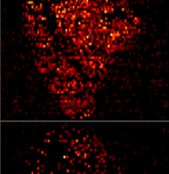
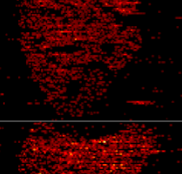
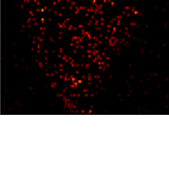
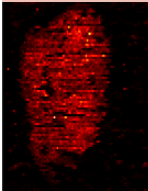
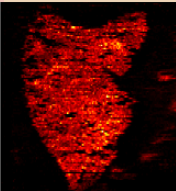
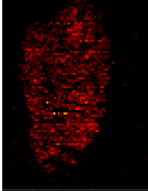
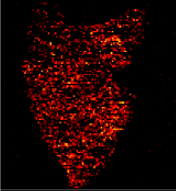
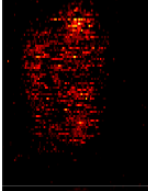
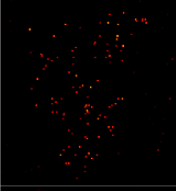
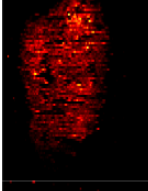
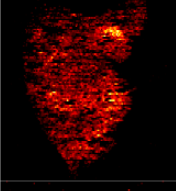
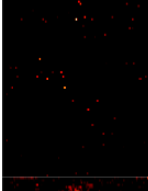
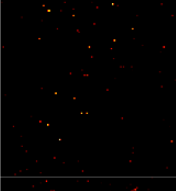
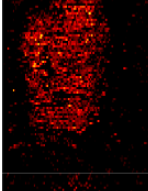
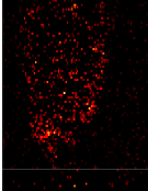
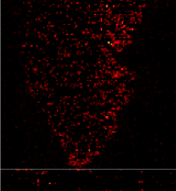
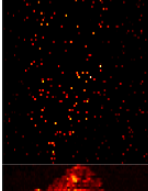
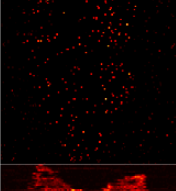
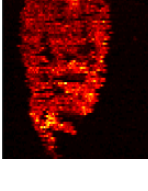
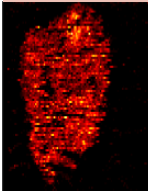
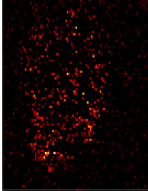
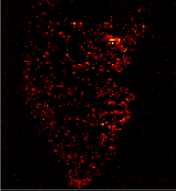
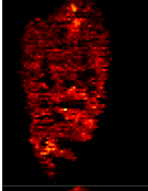
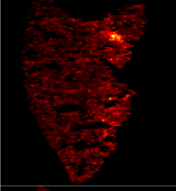
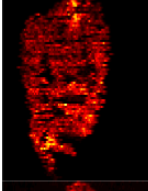
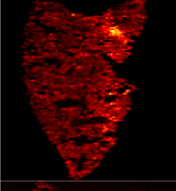
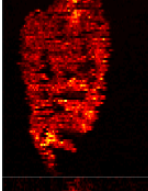
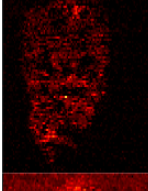
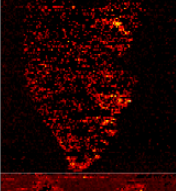
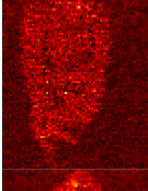
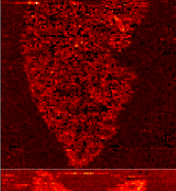
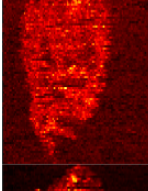
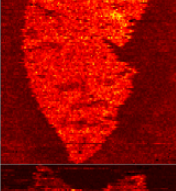
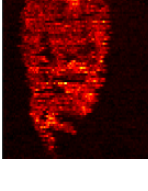
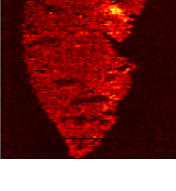
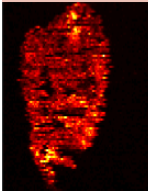
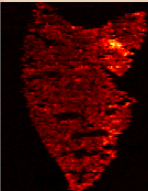
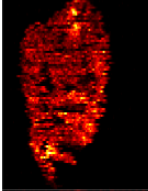
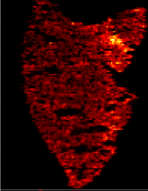
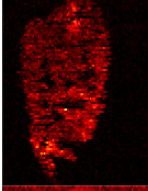
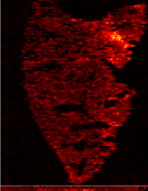
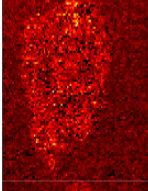
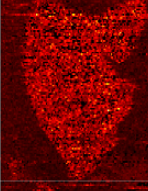
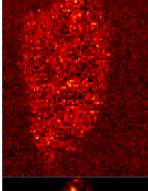
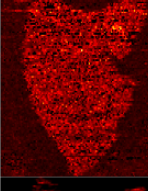
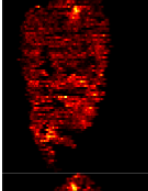
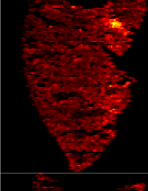
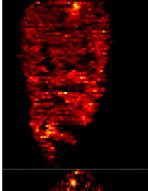
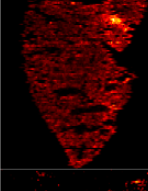
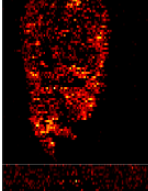
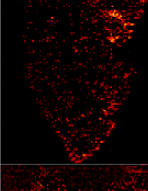
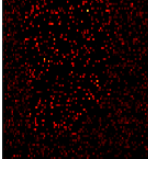
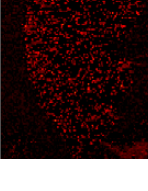
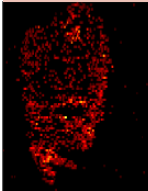
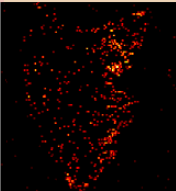
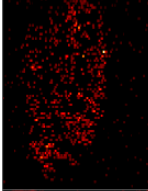
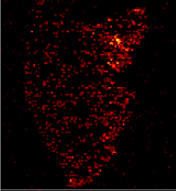
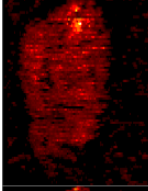
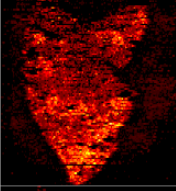
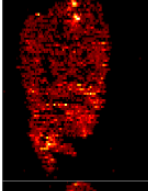
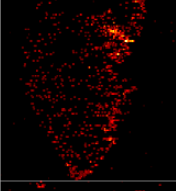
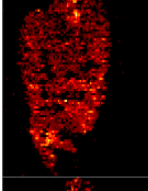
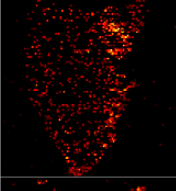
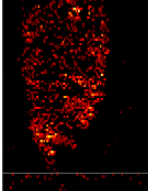
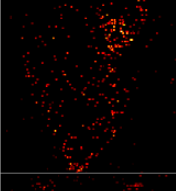
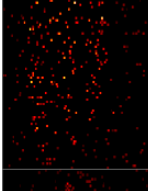
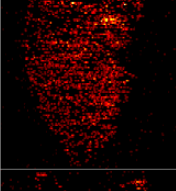
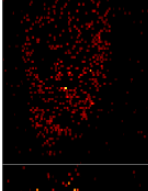
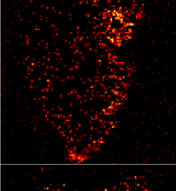
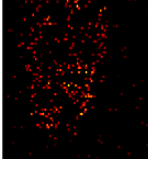
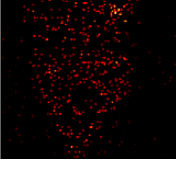
E18.5	PND7	PND28			
			852.5520	PC(40:8)	PC(18:2/22:6); [M+Na] ⁺ PC(20:4/20:4); [M+Na] ⁺
			853.7262	TG(50:2)	TG(16:0/16:0/18:2); [M+Na] ⁺ TG(16:0/16:1/18:1); [M+Na] ⁺ TG(14:0/16:0/22:5); [M+H] ⁺ TG(14:0/18:1/20:4); [M+H] ⁺ TG(16:0/16:0/20:5); [M+H] ⁺ TG(16:0/16:1/20:4); [M+H] ⁺
			854.5676	PC(40:7)	PC(18:1/22:6); [M+Na] ⁺ PC(18:2/22:5); [M+Na] ⁺ PC(20:3/20:4); [M+Na] ⁺ PC(20:4/22:6); [M+H] ⁺ PC(20:5/22:5); [M+H] ⁺
			855.7419	TG(50:1)	TG(16:0/16:0/18:1); [M+Na] ⁺ TG(16:0/18:2/18:2); [M+H] ⁺ TG(16:1/18:1/18:2); [M+H] ⁺
			856.5833	PC(40:6)	PC(18:0/22:6); [M+Na] ⁺ PC(18:1/22:5); [M+Na] ⁺ PC(18:2/22:4); [M+Na] ⁺ PC(20:2/20:4); [M+Na] ⁺ PC(20:3/22:6); [M+H] ⁺
			858.6013	PC(42:8)	PC(20:2/22:6); [M+H] ⁺ PC(20:4/22:4); [M+H] ⁺
			860.6169	PC(42:7)	PC(20:1/22:6); [M+H] ⁺
			874.5363	PC(42:11)	PC(20:5/22:6); [M+Na] ⁺
			879.7419	TG(52:3)	TG(16:0/16:0/20:3); [M+Na] ⁺ TG(16:0/18:1/18:2); [M+Na] ⁺ TG(16:0/16:0/22:6); [M+H] ⁺ TG(18:2/18:2/18:2); [M+H] ⁺
			881.7575	TG(52:2)	TG(16:0/18:0/18:2); [M+Na] ⁺ TG(16:0/18:1/18:1); [M+Na] ⁺ TG(18:1/18:2/18:2); [M+H] ⁺

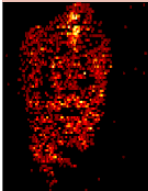
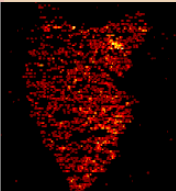
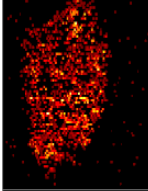
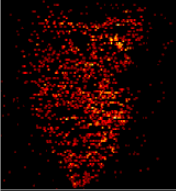
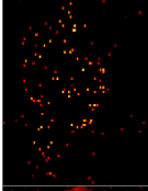
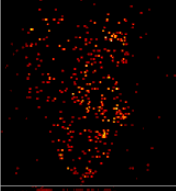
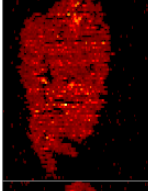
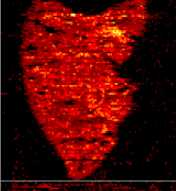
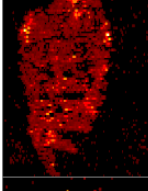
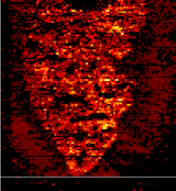
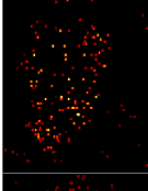
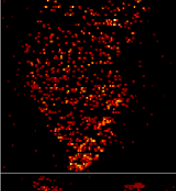
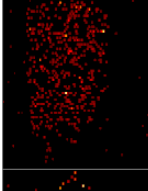
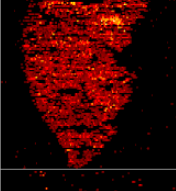
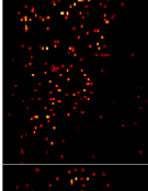
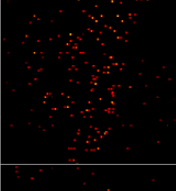
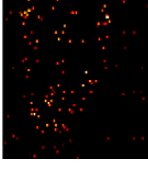
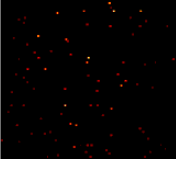
Table A2. Negative mode MS ion images from PND7 and PND28. For each ion image, m/z and identification is listed in the table. For replicates of nano-DESI images, see <https://lungmap.net>.

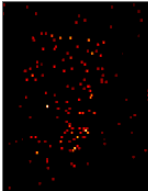
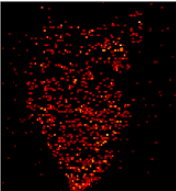
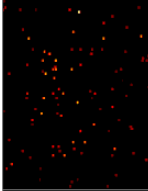
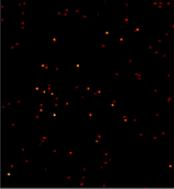
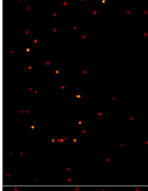
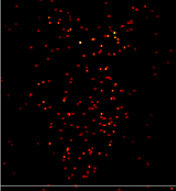
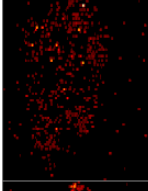
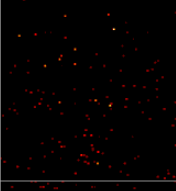
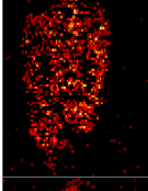
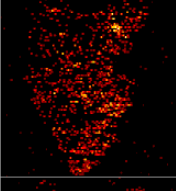
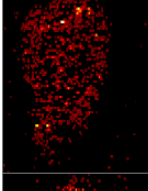
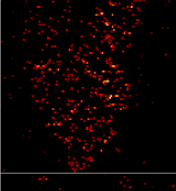
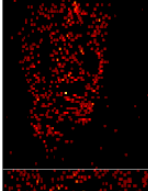
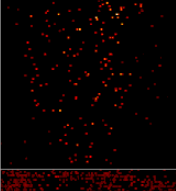
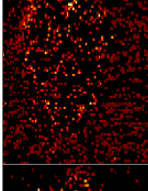
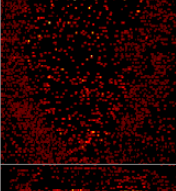
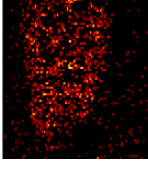
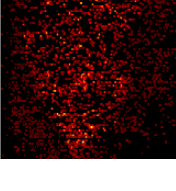
PND7	PND28	Exact m/z	Name (Sum)	Identification 1
		124.0068	MB	Taurine
		135.0307	MB	Hypoxanthine
		146.0452	MB	Glutamate
		175.024	MB	L-Ascorbic acid
		204.0312	MB	Xanthurenic acid
		215.0318	MB	D-Glucose
		237.2212	FA	cis-11-Hexadecenal
		255.1606	MB	5-Nonyltetrahydro-2-oxo-3-furancarboxylic acid
		255.2317	FA(16:0)	Isopalmitic acid

PND7	PND28			
		267.0723	FA	3-Deoxy-D-glycero-D-galacto-2-nonulosonic acid
		275.2003	FA(18:4)	Stearidonic acid
		277.2161	FA(18:3)	octadecatrienoic acid
		279.2317	FA(18:2)	octadecadienoic acid
		281.2472	FA(18:1)	oleic acid
		295.2265	FA	Dimorphecolic acid
		297.2422	FA	Ricinoleic acid
		301.2158	FA(20:5)	eicosapentaenoic acid
		303.2316	FA(20:4)	Eicosadiynoic acid

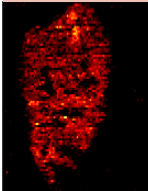
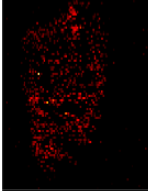
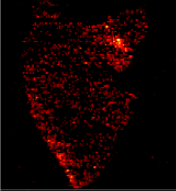
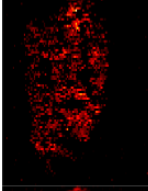
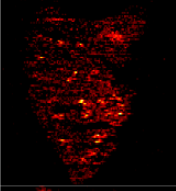
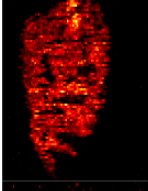
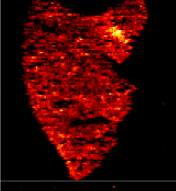
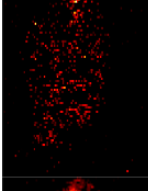
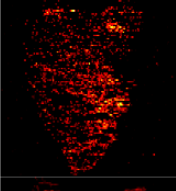
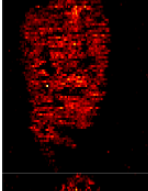
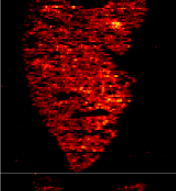
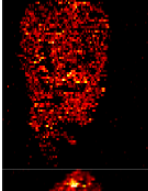
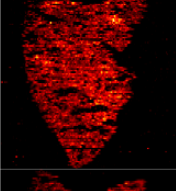
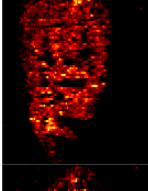
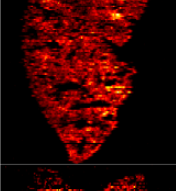
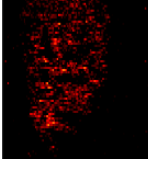
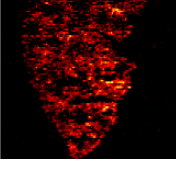
PND7	PND28			
		305.2473	FA(20:3)	eicosatrienoic acid
		307.2629	FA(20:2)	FA(20:2)
		309.2784	FA(20:1)	eicosenoic acid
		315.1951	FA	preclavulone lactone
		317.2107	FA	12-oxo-ETE
		327.2315	FA(22:6)	docosahexaenoic acid (DHA)
		329.2471	FA(22:5)	docosapentaenoic acid
		333.2785	FA(22:3)	FA(22:3)
		335.2215	FA	15-epi-PGA1

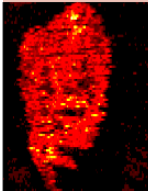
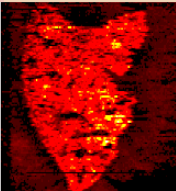
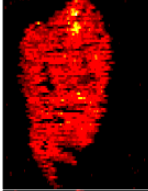
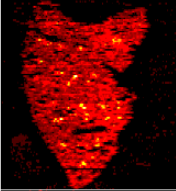
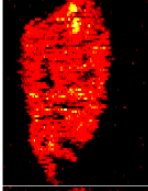
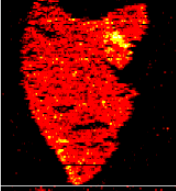
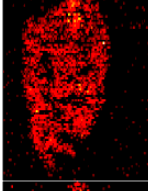
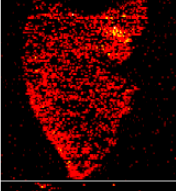
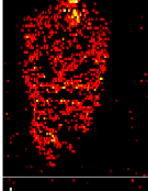
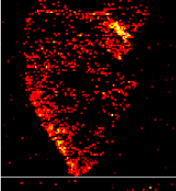
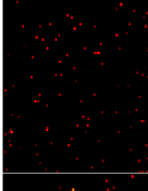
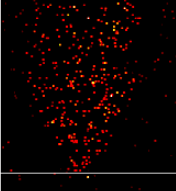
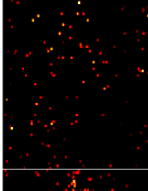
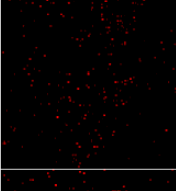
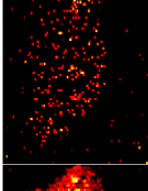
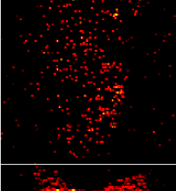
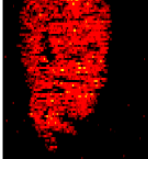
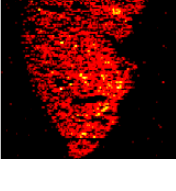
PND7	PND28			
		335.294	FA(22:2)	FA(22:2)
		337.3097	FA(22:1)	FA(22:1)
		346.0545	MB	Adenosine monophosphate
		355.2628	FA(24:6)	tetracosahexaenoic acid (THA)
		357.2782	ST	5 β -Chol-9(11)-en-24-oic Acid
		359.2939	FA(24:4)	tetracosatetraenoic acid
		361.19	MB	Lys Ile Cys
		365.3407	FA(24:1)	Tetracosenoic acid
		369.2268	MB	Val Arg Pro

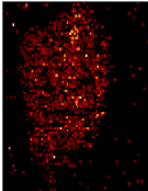
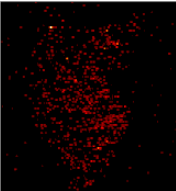
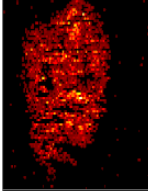
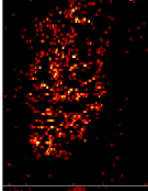
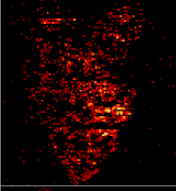
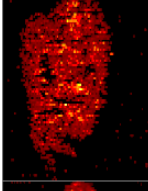
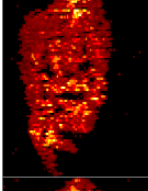
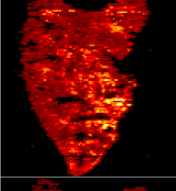
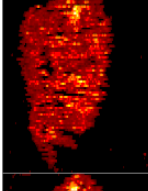
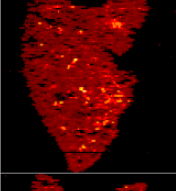
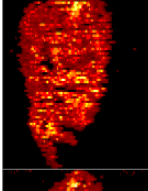
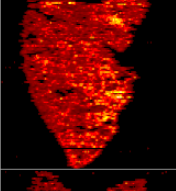
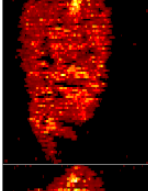
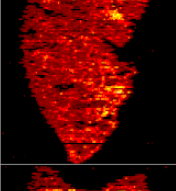
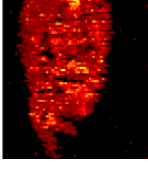
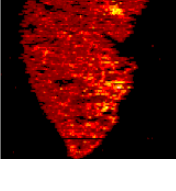
PND7	PND28			
		436.2835	PE(P-16:0)	PE(P-16:0/0:0)
		452.278	PE(16:0)	PE(16:0/0:0)
		478.2937	PE(18:1)	PE(18:1/0:0)
		480.3094	PE(18:0)	PE(18:0/0:0)
		483.2735	PG(16:0)	PG(16:0/0:0)
		500.2791	PE(20:4)	PE(20:4/0:0)
		508.3386	PE(20:0)	PE(20:0)
		509.2882	PG(18:1)	PG(18:1/0:0)
		511.3044	PG(18:0)	PG(18:0/0:0)

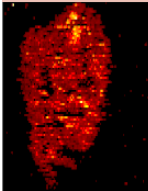
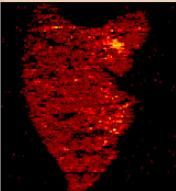
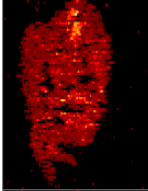
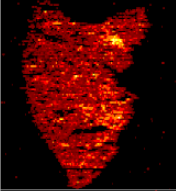
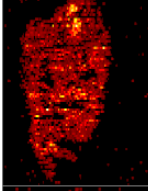
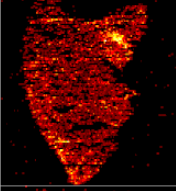
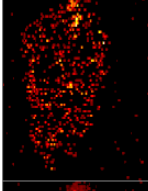
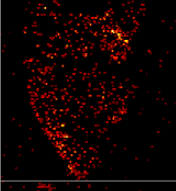
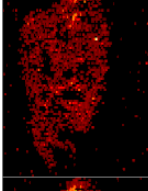
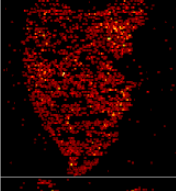
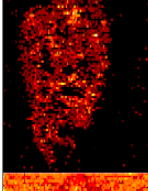
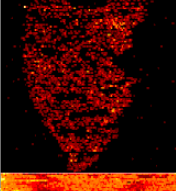
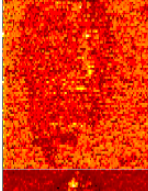
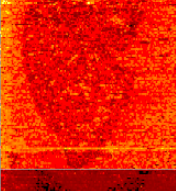
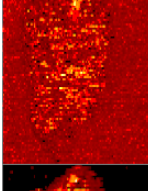
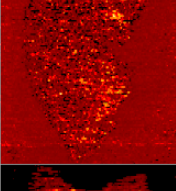
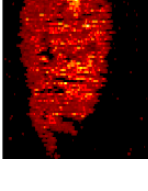
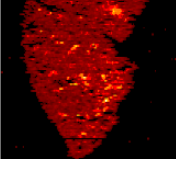
PND7	PND28			
		524.2783	PE(22:6)	PE(22:6/0:0)
		524.2988	PS(18:0)	PS(18:0/0:0)
		528.3095	PE(22:4)	PE(22:4/0:0)
		529.2584	PG(20:5)	PG(20:5/0:0)
		536.5042	Cer(34:1)	Cer(d18:1/16:0)
		555.2734	PG(22:6)	PG(22:6/0:0)
		556.3015	MB	Pro Val Glu Thr Leu
		571.2891	PI(16:0)	PI(16:0/0:0)
		599.3199	PI(18:0)	PI(18:0/0:0)

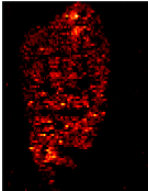
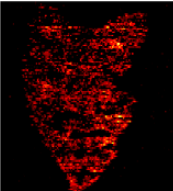
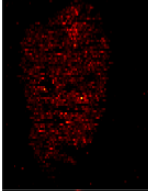
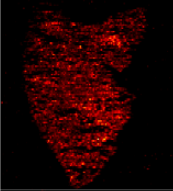
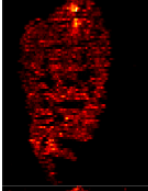
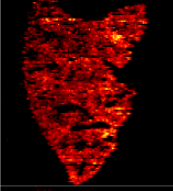
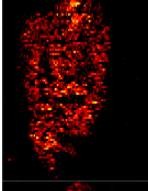
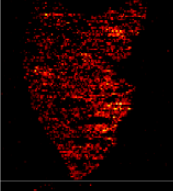
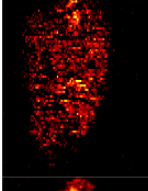
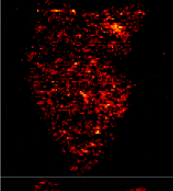
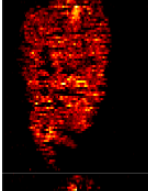
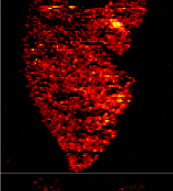
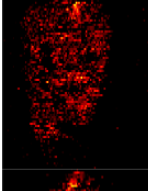
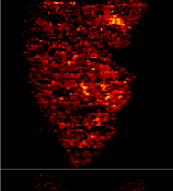
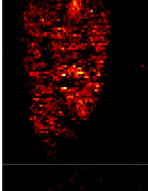
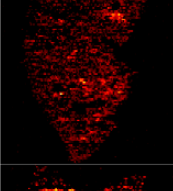
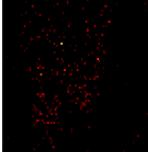
PND7	PND28			
		619.2893	PI(20:4)	PI(20:4/0:0)
		646.6145	Cer(42:2)	Cer(d18:1/24:1)
		648.6294	Cer(42:1)	Cer(d18:1/24:0)
		665.4397	PG(28:0)	PG(12:0/16:0) PG(14:0/14:0)
		671.4624	PA(34:2)	PA(34:2)
		673.4782	PA(34:1)	PA(34:1)
		675.5305	PA(O-35:0)	PA(O-35:0)
		687.5430	SM(d16:1/17:0)	SM(d16:1/17:0)
		690.5080	PE(32:0)	PE(16:0/16:0)

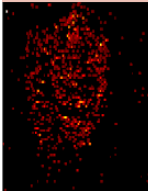
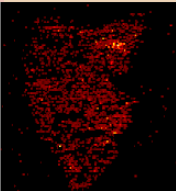
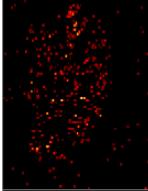
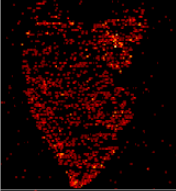
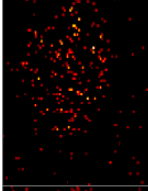
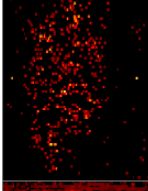
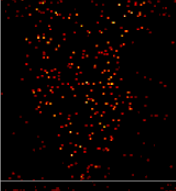
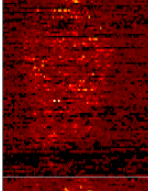
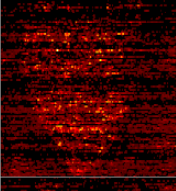
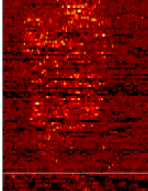
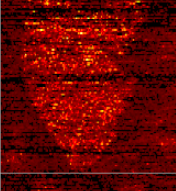
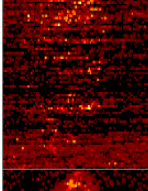
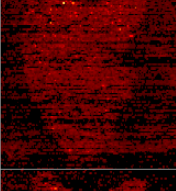
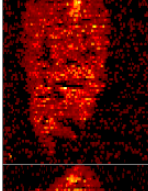
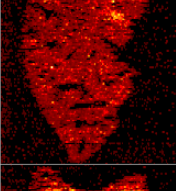
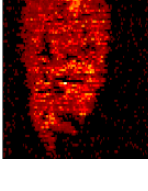
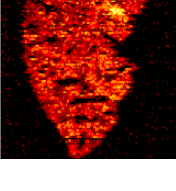
PND7	PND28			
		699.4944	PA(36:2)	PA(36:2)
		700.4927	PE(33:2)	PE(15:0/18:2)
		700.5277	PE(P-34:1)	PE(P-16:0/18:1)
		701.5100	PA(36:1)	PA(36:1)
		714.5089	PE(34:2)	PE(16:0/18:2) PE(16:1/18:1)
		716.5235	PE(34:1)	PE(16:1/18:0) PE(16:0/18:1)
		718.5393	PE(34:0)	PE(16:0/18:0)
		719.4863	PG(32:1)	PG(14:0/18:1) PG(16:0/16:1)
		720.4975	PE(P-36:5)	PE(P-16:0/20:5)

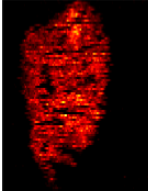
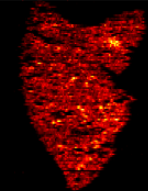
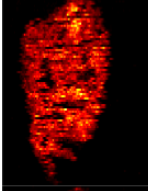
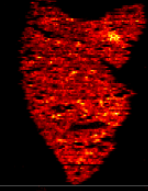
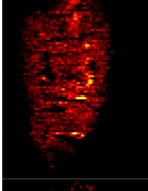
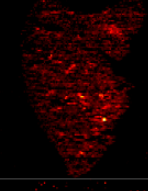
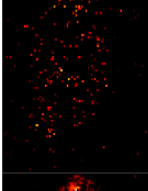
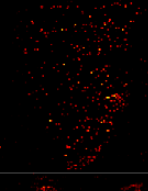
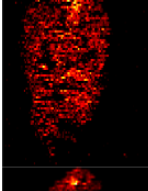
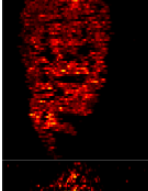
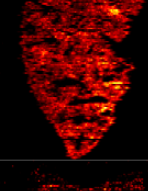
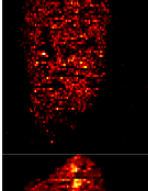
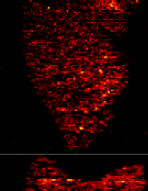
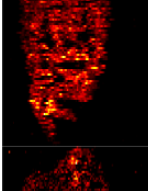
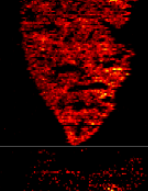
PND7	PND28			
		721.5034	PG(32:0)	PG(16:0/16:0)
		722.5124	PE(P-36:4)	PE(P-16:0/20:4)
		723.4943	PA(38:4)	PA(38:4)
		725.5101	PA(38:3)	PA(38:3)
		727.5249	PA(38:2)	PA(38:2)
		732.4810	PS(32:1)	PS(16:0/16:1)
		735.5173	PG(33:0)	PG(16:0/17:0)
		736.4916	PE(36:5)	PE(16:1/20:4) PE(16:0/20:5)
		738.5078	PE(36:4)	PE(18:1/18:3) PE(16:0/20:4)

PND7	PND28			
		740.5242	PE(36:3)	PE(16:0/20:3) PE(18:1/18:2)
		742.5402	PE(36:2)	PE(18:0/18:2) PE(18:1/18:1)
		743.4853	PG(34:3)	PG(16:0/18:3) PG(16:1/18:2)
		744.5553	PE(36:1)	PE(14:0/22:1) PE(16:0/20:1) PE(18:0/18:1)
		745.5018	PG(34:2)	PG(16:0/18:2) PG(16:1/18:1)
		746.5130	PE(P-38:6)	PE(P-16:0/22:6)
		747.5168	PG(34:1)	PG(16:0/18:1) PG(16:1/18:0)
		748.5161	PS(33:0)	PS(33:0)
		748.5284	PE(P-38:5)	PE(P-38:5)

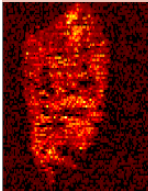
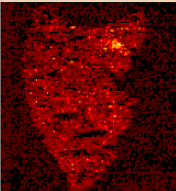
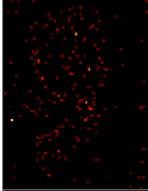
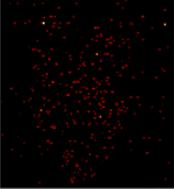
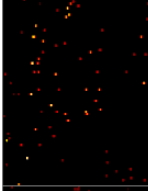
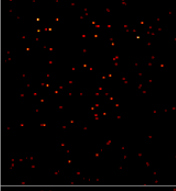
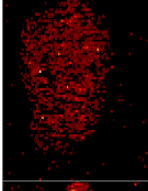
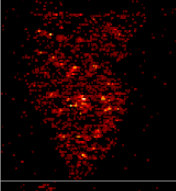
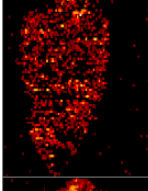
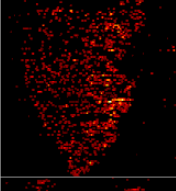
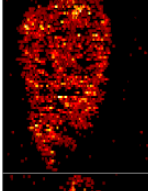
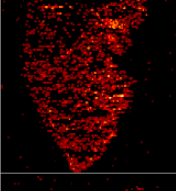
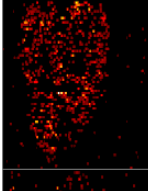
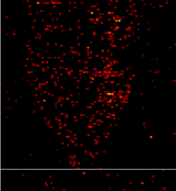
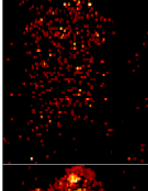
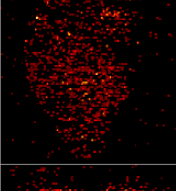
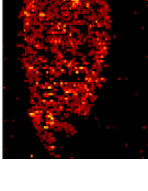
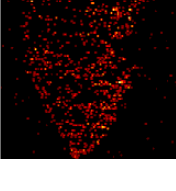
PND7	PND28			
		749.5336	PG(34:0)	PG(16:0/18:0)
		750.5451	PE(P-38:4)	PE(P-16:0/22:4) PE(P-18:0/20:4)
		751.5251	PA(40:4)	PA(40:4)
		752.5230	PE(37:4)	PE(17:0/20:4)
		760.4920	PE(38:7)	PE(16:1/22:6)
		760.5121	PS(34:1)	PS(16:1/18:0) PS(16:0/18:1)
		762.5092	PE(38:6)	PE(16:0/22:6)
		764.5224	PE(38:5)	PE(18:1/20:4)
		766.5394	PE(38:4)	PE(16:0/22:4) PE(18:0/20:4) PE(18:1/20:3)

PND7	PND28			
		767.4867	PG(36:5)	PG(16:0/20:5) PG(18:2/18:3)
		768.5553	PE(38:3)	PE(18:0/20:3)
		769.5015	PG(36:4)	PG(16:0/20:4) PG(18:2/18:2)
		771.5161	PG(36:3)	PG(16:0/20:3) PG(18:1/18:2)
		772.5285	PE(P-40:7)	PE(P-18:1/22:6)
		773.5325	PG(36:2)	PG(16:0/20:2) PG(18:0/18:2) PG(18:1/18:1)
		774.5439	PE(P-40:6)	PE(P-18:0/22:6)
		775.5487	PG(36:1)	PG(18:0/18:1)
		776.5249	PE(39:6)	PE(17:0/22:6)

PND7	PND28			
		776.5782	PS(O-36:0)	PS(O-36:0)
		777.5364	PS(34:1)	PS(34:1)
		778.5752	PE(P-40:4)	PE(P-20:0/20:4) PE(P-18:0/22:4)
		782.4967	PS(36:4)	PS(16:0/20:4)
		783.4081	MB	Fumonisin FP2
		783.4571	MB	Hoduloside VI
		783.5182	PG(37:4)	PG(17:0/20:4)
		786.5067	PE(40:8)	PE(18:2/22:6)
		786.5276	PS(36:2)	PS(18:1/18:1) PS(18:0/18:2)

PND7	PND28			
		788.5237	PE(40:7)	PE(18:1/22:6)
		788.5445	PS(36:1)	PS(18:0/18:1)
		790.5390	PE(40:6)	PE(18:0/22:6)
		791.4858	PG(38:7)	PG(16:1/22:6) PG(18:2/20:5)
		792.5526	PE(40:5)	PE(40:5)
		793.5008	PG(38:6)	PG(16:0/22:6) PG(18:2/20:4) PG(18:1/20:5)
		794.5704	PE(40:4)	PE(18:0/22:4) PE(20:0/20:4)
		795.5190	PG(38:5)	PG(18:0/20:5)
		797.5327	PG(38:4)	PG(16:0/22:4) PG(18:1/20:3) PG(18:0/20:4)

PND7	PND28			
		800.6185	PE(40:1)	PE(18:1/22:0)
		801.5652	PG(38:2)	PG(18:0/20:2)
		802.5742	PE(P-42:6)	PE(P-20:0/22:6)
		806.4980	PS(38:6)	PS(16:0/22:6) PS(18:2/20:4)
		807.5019	PI(32:1)	PI(16:0/16:1)
		807.5159	PG(39:6)	PG(17:0/22:6)
		808.5139	PS(38:5)	PS(18:1/20:4) PS(18:0/20:5)
		808.5859	PE(41:4)	PE(19:0/22:4)
		810.5291	PS(38:4)	PS(18:0/20:4)

PND7	PND28			
		812.5430	PS(38:3)	PS(18:0/20:3)
		814.5379	PE(42:8)	PE(20:2/22:6)
		815.4875	PG(40:9)	PG(18:3/22:6) PG(20:4/20:5)
		816.5535	PE(42:7)	PE(20:1/22:6)
		817.5022	PG(40:8)	PG(18:2/22:6)_A
		819.5167	PG(40:7)	PG(18:1/22:6)_C
		820.5133	PS(39:6)	PS(17:0/22:6)
		820.5849	PE(42:5)	PE(20:4/22:1)
		821.5319	PG(40:6)	PG(18:0/22:6)_A

PND7	PND28			
		822.6006	PE(42:4)	PE(20:4/22:0)
		832.5134	PS(40:7)	PS(18:1/22:6)
		833.5172	PI(34:2)	PI(16:0/18:2) PI(16:1/18:1)
		834.5294	PS(40:6)	PS(18:0/22:6)
		835.5321	PI(34:1)	PI(16:0/18:1)
		836.5430	PS(40:5)	PS(40:5)
		838.5612	PS(40:4)	PS(18:0/22:4)
		839.4879	PG(42:11)	PG(20:5/22:6)
		841.5012	PG(42:10)	PG(20:4/22:6)

PND7	PND28			
		843.5178	PG(42:9)	PG(20:3/22:6)_A
		845.5331	PG(42:8)	PG(20:4/22:4) PG(20:2/22:6)
		855.5017	PI(36:5)	PI(16:0/20:5) PI(16:1/20:4)
		856.5144	PS(42:9)	PS(20:3/22:6)
		857.5189	PI(36:4)	PI(16:0/20:4) PI(18:2/18:2)
		859.5348	PI(36:3)	PI(16:0/20:3) PI(18:1/18:2)
		861.5479	PI(36:2)	PI(18:0/18:2)
		863.5630	PI(36:1)	PI(18:0/18:1)
		865.5033	PG(44:12)	PG(22:6/22:6)_B

PND7	PND28			
		869.5342	PG(44:10)	PG(22:4/22:6)
		881.5176	PI(38:6)	PI(18:2/20:4) PI(18:1/20:5) PI(16:0/22:6)
		883.5338	PI(38:5)	PI(18:1/20:4) PI(18:0/20:5)
		885.5471	PI(38:4)	PI(16:0/22:4) PI(18:1/20:3) PI(18:0/20:4)
		887.5640	PI(38:3)	PI(18:0/20:3)
		907.5338	PI(40:7)	PI(20:3/20:4) PI(18:1/22:6)
		909.5466	PI(40:6)	PI(20:2/20:4) PI(18:0/22:6)
		911.5635	PI(40:5)	PI(40:5)
		913.5802	PI(40:4)	PI(18:0/22:4)

APPENDIX B. CHAPTER 4 SUPPLEMENTAL

Table B1. Dilution scheme for calibration standards. Standard curve ranging from 5 μ M to 1 nM.

ID	Standard Solution Concentration (nM)	Volume of Intermediate working Standard Solution (mL)	Volume of Diluent (mL)	Final tissue Concentration following addition of 30 μ L of standard solution to 150 μ L of extracted tissue supernatant
A	25,000	0.4 mL of 50 μ M	0.4 mL	5000 nM
B	10,000	0.3 mL of A	0.45 mL	2000 nM
C	5,000	0.4 mL of B	0.4 mL	1000 nM
D	2,500	0.4 mL of C	0.4 mL	500 nM
E	1,000	0.3 mL of D	0.45 mL	200 nM
F	500	0.4 mL of E	0.4 mL	100 nM
G	250	0.4 mL of F	0.4 mL	50 nM
H	100	0.3 mL of G	0.45 mL	20 nM
I	50	0.4 mL of H	0.4 mL	10 nM
J	25	0.4 mL of I	0.4 mL	5 nM
K	10	0.3 mL of J	0.45 mL	2 nM
L	5	0.4 mL of K	0.4 mL	1 nM

Table B2. Mass spectrometric parameters.

	Precursor ion <i>m/z</i>	Collision energy (eV)	Product ion (<i>m/z</i>)
Diclofenac	296.1	30	215.1
Diclofenac-d4	300.1	30	219.1
Hydroxy metabolite	312.1	30	231.1
Acyl glucuronide metabolite	472.1	30	215.1

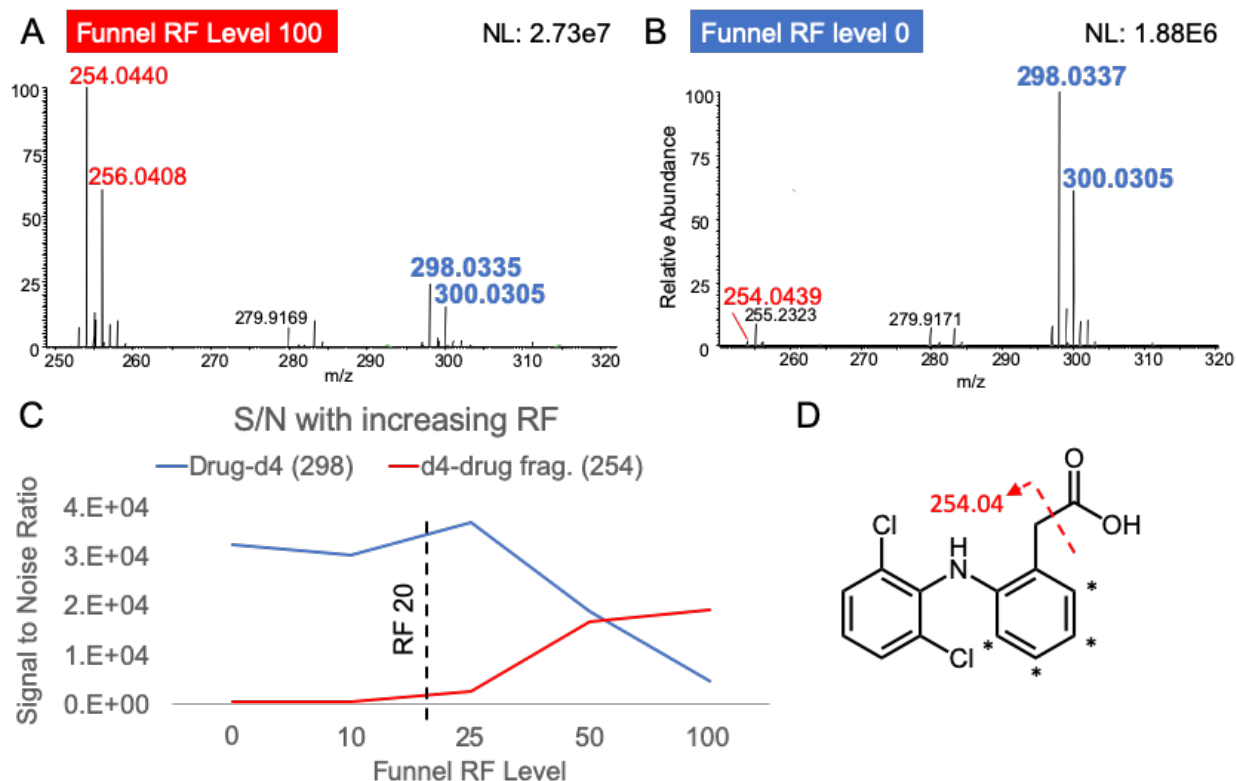


Figure B1. Direct infusion of 10 μ M solution of diclofenac-d4 (m/z 298.033) standard for instrument method optimization. (A) Negative ion mode spectrum with funnel RF level on Q-Exactive HF-X set to 100, decarboxylated fragment (m/z 254.044) of diclofenac-d4 is observed with high intensity. (B) Negative ion mode spectrum with funnel RF level on Q-Exactive HF-X set to 0, very little fragmentation is observed. (C) Signal to noise ratio of diclofenac-d4 (blue) and diclofenac-d4 fragment (red) with increasing funnel RF level. Optimized funnel RF level was 20. (D) Diclofenac-d4 structure, * indicates which carbon has deuterated hydrogens attached, red line indicates where fragmentation occurs to create m/z 254.04 fragment.

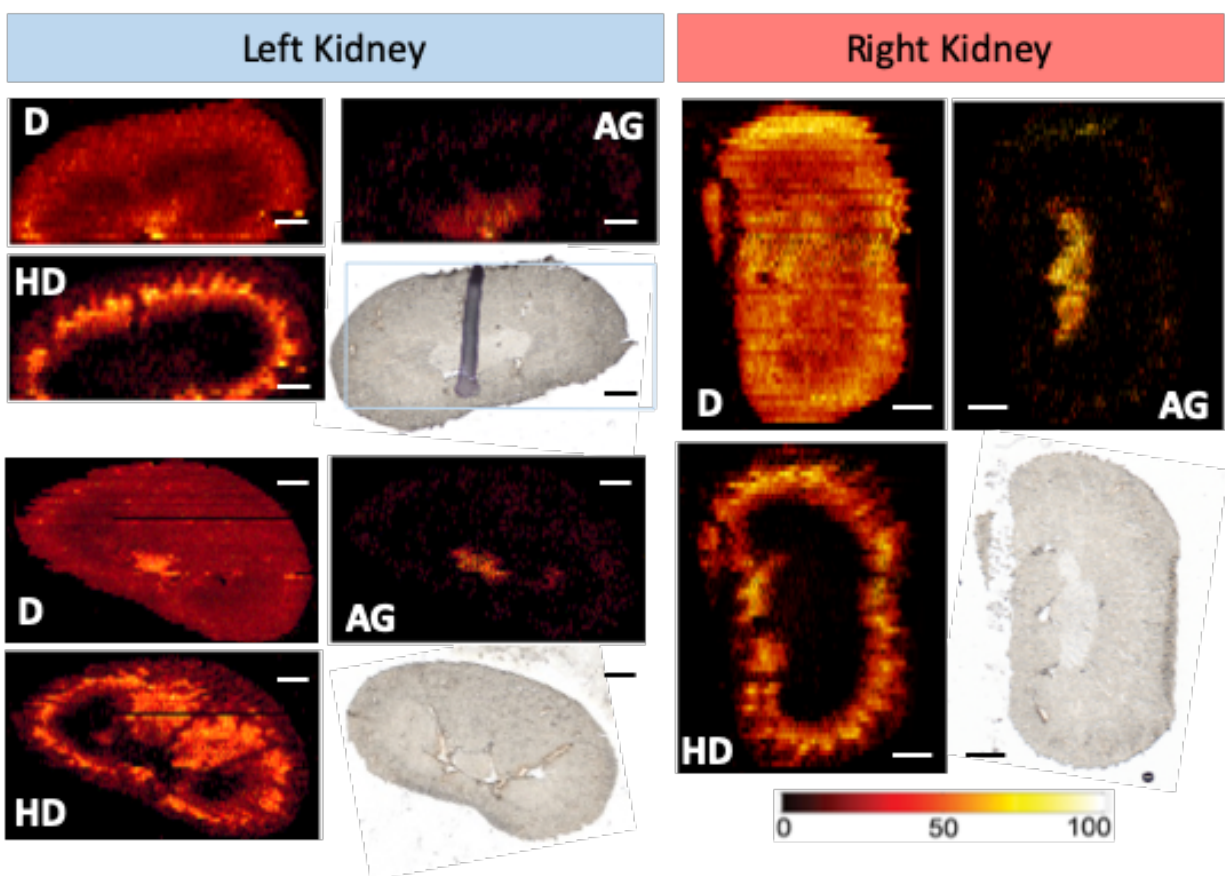


Figure B2. Optical and nano-DESI ion images of diclofenac dosed mouse kidney replicate tissue sections. Ion images of diclofenac (D), acyl glucuronide (AG), and hydroxydiclofenac (HD) are shown. Ion images are self-normalized to internal standard, diclofenac-d4. Scale bar represents 1 mm. Intensity scale ranges from 0% intensity (black) to 100% (white).

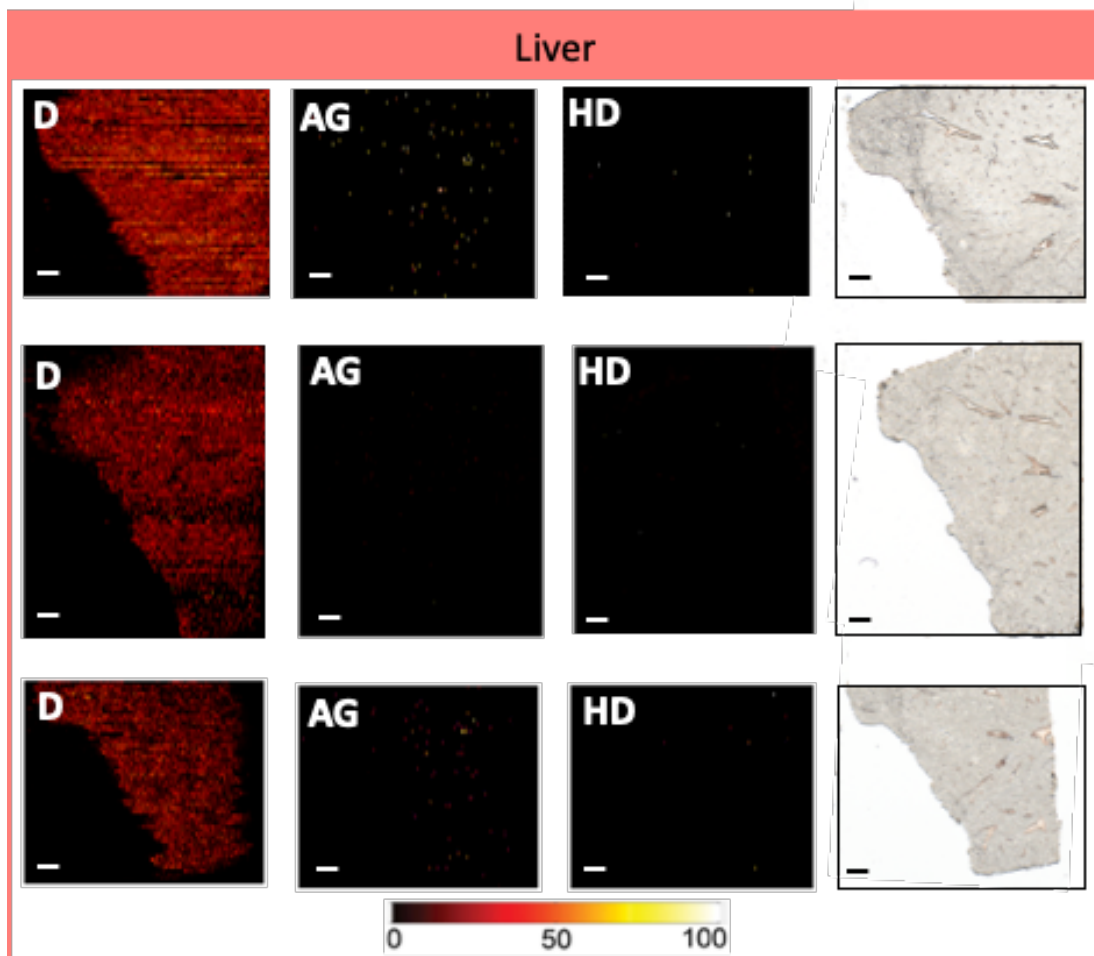


Figure B3. Optical and nano-DESI ion images of diclofenac dosed mouse liver replicate tissue sections. Ion images of diclofenac (D), acyl glucuronide (AG), and hydroxydiclofenac (HD) are shown. Ion images are self-normalized to internal standard, diclofenac-d4. Scale bar represents 1 mm. Intensity scale ranges from 0% intensity (black) to 100% (white).

REFERENCES

- (1) Badu-Tawiah, A. K.; Eberlin, L. S.; Ouyang, Z.; Cooks, R. G. Chemical Aspects of the Extractive Methods of Ambient Ionization Mass Spectrometry. *Annu. Rev. Phys. Chem.* **2013**, *64* (1), 481–505.
- (2) Ifa, D. R.; Wu, C.; Ouyang, Z.; Cooks, R. G. Desorption Electrospray Ionization and Other Ambient Ionization Methods: Current Progress and Preview. *Analyst* **2010**, *135* (4), 669.
- (3) Javanshad, R.; Venter, A. R. Ambient Ionization Mass Spectrometry: Real-Time, Proximal Sample Processing and Ionization. *Anal. Methods* **2017**, *9* (34), 4896–4907.
- (4) Huang, M.-Z.; Yuan, C.-H.; Cheng, S.-C.; Cho, Y.-T.; Shiea, J. Ambient Ionization Mass Spectrometry. *Annu. Rev. Anal. Chem.* **2010**, *3* (1), 43–65.
- (5) Monge, M. E.; Harris, G. A.; Dwivedi, P.; Fernández, F. M. Mass Spectrometry: Recent Advances in Direct Open Air Surface Sampling/Ionization. *Chem. Rev.* **2013**, *113* (4), 2269–2308.
- (6) Harris, G. A.; Galhena, A. S.; Fernández, F. M. Ambient Sampling/Ionization Mass Spectrometry: Applications and Current Trends. *Anal. Chem.* **2011**, *83* (12), 4508–4538.
- (7) Feider, C. L.; Krieger, A.; DeHoog, R. J.; Eberlin, L. S. Ambient Ionization Mass Spectrometry: Recent Developments and Applications. *Anal. Chem.* **2019**, *91* (7), 4266–4290.
- (8) Venter, A. R.; Douglass, K. A.; Shelley, J. T.; Hasman, G.; Honarvar, E. Mechanisms of Real-Time, Proximal Sample Processing during Ambient Ionization Mass Spectrometry. *Anal. Chem.* **2014**, *86* (1), 233–249.
- (9) El-Faramawy, A.; Siu, K. W. M.; Thomson, B. A. Efficiency of Nano-Electrospray Ionization. *J. Am. Soc. Mass Spectrom.* **2005**, *16* (10), 1702–1707.
- (10) Karas, M.; Bahr, U.; Dülcks, T. Nano-Electrospray Ionization Mass Spectrometry: Addressing Analytical Problems beyond Routine. *Fresenius. J. Anal. Chem.* **2000**, *366* (6–7), 669–676.
- (11) Laskin, J.; Lanekoff, I. Ambient Mass Spectrometry Imaging Using Direct Liquid Extraction Techniques. *Analytical Chemistry*. 2016, pp 52–73.
- (12) Roach, P. J.; Laskin, J.; Laskin, A. Nanospray Desorption Electrospray Ionization: An Ambient Method for Liquid-Extraction Surface Sampling in Mass Spectrometry. *Analyst* **2010**, *135* (9), 2233.

- (13) Lanekoff, I.; Thomas, M.; Carson, J. P.; Smith, J. N.; Timchalk, C.; Laskin, J. Imaging Nicotine in Rat Brain Tissue by Use of Nanospray Desorption Electrospray Ionization Mass Spectrometry. *Anal. Chem.* **2013**, *85* (2), 882–889.
- (14) Lanekoff, I.; Thomas, M.; Laskin, J. Shotgun Approach for Quantitative Imaging of Phospholipids Using Nanospray Desorption Electrospray Ionization Mass Spectrometry. *Anal. Chem.* **2014**, *86* (3), 1872–1880.
- (15) Laskin, J.; Heath, B. S.; Roach, P. J.; Cazares, L.; Semmes, O. J. Tissue Imaging Using Nanospray Desorption Electrospray Ionization Mass Spectrometry. *Anal. Chem.* **2012**, *84* (1), 141–148.
- (16) Nguyen, S. N.; Liyu, A. V.; Chu, R. K.; Anderton, C. R.; Laskin, J. Constant-Distance Mode Nanospray Desorption Electrospray Ionization Mass Spectrometry Imaging of Biological Samples with Complex Topography. *Anal. Chem.* **2017**, *89* (2), 1131–1137.
- (17) Nguyen, S. N.; Sontag, R. L.; Carson, J. P.; Corley, R. A.; Ansong, C.; Laskin, J. Towards High-Resolution Tissue Imaging Using Nanospray Desorption Electrospray Ionization Mass Spectrometry Coupled to Shear Force Microscopy. *J. Am. Soc. Mass Spectrom.* **2018**, *29* (2), 316–322.
- (18) Wang, Z. Paternò-Büchi Reaction. In *Comprehensive Organic Name Reactions and Reagents*; John Wiley & Sons, Inc., 2010; pp 2126–2130.
- (19) Ma, X.; Xia, Y. Pinpointing Double Bonds in Lipids by Paternò-Büchi Reactions and Mass Spectrometry. *Angew. Chemie - Int. Ed.* **2014**, *53* (10), 2592–2596.
- (20) Ma, X.; Chong, L.; Tian, R.; Shi, R.; Hu, T. Y.; Ouyang, Z.; Xia, Y. Identification and Quantitation of Lipid C=C Location Isomers: A Shotgun Lipidomics Approach Enabled by Photochemical Reaction. *Proc. Natl. Acad. Sci. U. S. A.* **2016**, *113* (10), 2573–2578.
- (21) Wang, M.; Wang, C.; Han, R. H.; Han, X. Novel Advances in Shotgun Lipidomics for Biology and Medicine. *Prog. Lipid Res.* **2016**, *61*, 83–108.
- (22) Pati, S.; Nie, B.; Arnold, R. D.; Cummings, B. S. Extraction, Chromatographic and Mass Spectrometric Methods for Lipid Analysis. *Biomed. Chromatogr.* **2016**, *30* (5), 695–709.
- (23) Li, L.; Han, J.; Wang, Z.; Liu, J.; Wei, J.; Xiong, S.; Zhao, Z. Mass Spectrometry Methodology in Lipid Analysis. *Int. J. Mol. Sci.* **2014**, *15* (6), 10492–10507.
- (24) Bou Khalil, M.; Hou, W.; Zhou, H.; Elisma, F.; Swayne, L. A.; Blanchard, A. P.; Yao, Z.; Bennett, S. A. L.; Figeys, D. Lipidomics Era: Accomplishments and Challenges. *Mass Spectrom. Rev.* **2010**, *29* (6), 877–929.
- (25) Wang, C.; Wang, M.; Han, X. Applications of Mass Spectrometry for Cellular Lipid Analysis. *Mol. Biosyst.* **2015**, *11* (3), 698–713.

- (26) McAnoy, A. M.; Wu, C. C.; Murphy, R. C. Direct Qualitative Analysis of Triacylglycerols by Electrospray Mass Spectrometry Using a Linear Ion Trap. *J. Am. Soc. Mass Spectrom.* **2005**, *16* (9), 1498–1509.
- (27) Cheng, C.; Gross, M. L.; Pittenauer, E. Complete Structural Elucidation of Triacylglycerols by Tandem Sector Mass Spectrometry. *Anal. Chem.* **1998**, *70* (20), 4417–4426.
- (28) Coleman, R. A.; Lee, D. P. Enzymes of Triacylglycerol Synthesis and Their Regulation. *Prog. Lipid Res.* **2004**, *43* (2), 134–176.
- (29) Murphy, R. C.; Leiker, T. J.; Barkley, R. M. Glycerolipid and Cholesterol Ester Analyses in Biological Samples by Mass Spectrometry. *Biochim. Biophys. Acta - Mol. Cell Biol. Lipids* **2011**, *1811* (11), 776–783.
- (30) Quehenberger, O.; Armando, A. M.; Brown, A. H.; Milne, S. B.; Myers, D. S.; Merrill, A. H.; Bandyopadhyay, S.; Jones, K. N.; Kelly, S.; Shaner, R. L.; et al. Lipidomics Reveals a Remarkable Diversity of Lipids in Human Plasma. *J. Lipid Res.* **2010**, *51* (11), 3299–3305.
- (31) Murphy, R. C. Glycerol Esters. *New Dev. Mass Spectrom.* **2015**, *2015-Janua* (4), 105–129.
- (32) Hsu, F.-F.; Turk, J. Structural Characterization of Triacylglycerols as Lithiated Adducts by Electrospray Ionization Mass Spectrometry Using Low-Energy Collisionally Activated Dissociation on a Triple Stage Quadrupole Instrument. *J. Am. Soc. Mass Spectrom.* **1999**, *10* (7), 587–599.
- (33) Ham, B. M.; Cole, R. B. Determination of Apparent Decomposition Threshold Energies of Lithium Adducts of Acylglycerols Using Tandem Mass Spectrometry and a Novel Derived Effective Reaction Path Length Approach. *J. Mass Spectrom.* **2008**, *43* (11), 1482–1493.
- (34) Hsu, F. F.; Turk, J. Electrospray Ionization Multiple-Stage Linear Ion-Trap Mass Spectrometry for Structural Elucidation of Triacylglycerols: Assignment of Fatty Acyl Groups on the Glycerol Backbone and Location of Double Bonds. *J. Am. Soc. Mass Spectrom.* **2010**, *21* (4), 657–669.
- (35) Kalo, P. J.; Ollilainen, V.; Rocha, J. M.; Malcata, F. X. Identification of Molecular Species of Simple Lipids by Normal Phase Liquid Chromatography–Positive Electrospray Tandem Mass Spectrometry, and Application of Developed Methods in Comprehensive Analysis of Low Erucic Acid Rapeseed Oil Lipids. *Int. J. Mass Spectrom.* **2006**, *254* (1–2), 106–121.
- (36) Marzilli, L. A.; Fay, L. B.; Dionisi, F.; Vouros, P. Structural Characterization of Triacylglycerols Using Electrospray Ionization-MSn Ion-Trap MS. *JAOCs, J. Am. Oil Chem. Soc.* **2003**, *80* (3), 195–202.
- (37) Thomas, M. C.; Mitchell, T. W.; Harman, D. G.; Deeley, J. M.; Murphy, R. C.; Blanksby, S. J. Elucidation of Double Bond Position in Unsaturated Lipids by Ozone Electrospray Ionization Mass Spectrometry. *Anal. Chem.* **2007**, *79* (13), 5013–5022.

- (38) Poad, B. L. J.; Pham, H. T.; Thomas, M. C.; Nealon, J. R.; Campbell, J. L.; Mitchell, T. W.; Blanksby, S. J. Ozone-Induced Dissociation on a Modified Tandem Linear Ion-Trap: Observations of Different Reactivity for Isomeric Lipids. *J. Am. Soc. Mass Spectrom.* **2010**, *21* (12), 1989–1999.
- (39) Marshall, D. L.; Pham, H. T.; Bhujel, M.; Chin, J. S. R.; Yew, J. Y.; Mori, K.; Mitchell, T. W.; Blanksby, S. J. Sequential Collision- and Ozone-Induced Dissociation Enables Assignment of Relative Acyl Chain Position in Triacylglycerols. *Anal. Chem.* **2016**, *88* (5), 2685–2692.
- (40) Ren, J.; Franklin, E. T.; Xia, Y. Uncovering Structural Diversity of Unsaturated Fatty Acyls in Cholesteryl Esters via Photochemical Reaction and Tandem Mass Spectrometry. *J. Am. Soc. Mass Spectrom.* **2017**, *28* (7), 1432–1441.
- (41) Han, X. *Lipidomics*; John Wiley & Sons, Inc: Hoboken, NJ, USA, 2016.
- (42) Liebisch, G.; Vizcaíno, J. A.; Köfeler, H.; Trötz Müller, M.; Griffiths, W. J.; Schmitz, G.; Spener, F.; Wakelam, M. J. O. Shorthand Notation for Lipid Structures Derived from Mass Spectrometry. *J. Lipid Res.* **2013**, *54* (6), 1523–1530.
- (43) Agren, J. J.; Julkunen, A.; Penttila, I. Rapid Separation of Serum Lipids for Fatty Acid Analysis by a Single Aminopropyl Column. *J. Lipid Res.* **1992**, *33* (12), 1871–1876.
- (44) Ardini-Poleske, M. E.; Clark, R. F.; Ansong, C.; Carson, J. P.; Corley, R. A.; Deutsch, G. H.; Hagood, J. S.; Kaminski, N.; Mariani, T. J.; Potter, S. S.; et al. LungMAP: The Molecular Atlas of Lung Development Program. *Am. J. Physiol. Cell. Mol. Physiol.* **2017**, *313* (5), L733–L740.
- (45) Moghieb, A.; Clair, G.; Mitchell, H. D.; Kitzmiller, J.; Zink, E. M.; Kim, Y.-M.; Petyuk, V.; Shukla, A.; Moore, R. J.; Metz, T. O.; et al. Time-Resolved Proteome Profiling of Normal Lung Development. *Am. J. Physiol. Cell. Mol. Physiol.* **2018**, *315* (1), L11–L24.
- (46) Clair, G.; Piehowski, P. D.; Nicola, T.; Kitzmiller, J. A.; Huang, E. L.; Zink, E. M.; Sontag, R. L.; Orton, D. J.; Moore, R. J.; Carson, J. P.; et al. Spatially-Resolved Proteomics: Rapid Quantitative Analysis of Laser Capture Microdissected Alveolar Tissue Samples. *Sci. Rep.* **2016**, *6* (1), 39223.
- (47) Dautel, S. E.; Kyle, J. E.; Clair, G.; Sontag, R. L.; Weitz, K. K.; Shukla, A. K.; Nguyen, S. N.; Kim, Y.-M.; Zink, E. M.; Luders, T.; et al. Lipidomics Reveals Dramatic Lipid Compositional Changes in the Maturing Postnatal Lung. *Sci. Rep.* **2017**, *7* (1), 40555.
- (48) Kyle, J. E.; Clair, G.; Bandyopadhyay, G.; Misra, R. S.; Zink, E. M.; Bloodsworth, K. J.; Shukla, A. K.; Du, Y.; Lillis, J.; Myers, J. R.; et al. Cell Type-Resolved Human Lung Lipidome Reveals Cellular Cooperation in Lung Function. *Sci. Rep.* **2018**, *8* (1), 13455.
- (49) Schittny, J. C. Development of the Lung. *Cell and Tissue Research.* 2017, pp 427–444.

- (50) Warburton, D.; Schwarz, M.; Tefft, D.; Flores-Delgado, G.; Anderson, K. D.; Cardoso, W. V. The Molecular Basis of Lung Morphogenesis. *Mechanisms of Development*. 2000, pp 55–81.
- (51) Chao, C.-M.; El Agha, E.; Tiozzo, C.; Minoo, P.; Bellusci, S. A Breath of Fresh Air on the Mesenchyme: Impact of Impaired Mesenchymal Development on the Pathogenesis of Bronchopulmonary Dysplasia. *Front. Med.* **2015**, *2*.
- (52) Creuwels, L. a; van Golde, L. M.; Haagsman, H. P. The Pulmonary Surfactant System: Biochemical and Clinical Aspects. *Lung* **1997**, *175* (1), 1–39.
- (53) Veldhuizen, R.; Nag, K.; Orgeig, S.; Possmayer, F. The Role of Lipids in Pulmonary Surfactant. *Biochim. Biophys. Acta* **1998**, *1408* (2–3), 90–108.
- (54) Akella, A.; Deshpande, S. B. Pulmonary Surfactants and Their Role in Pathophysiology of Lung Disorders. *Indian Journal of Experimental Biology*. 2013, pp 5–22.
- (55) Orgeig, S.; Morrison, J. L.; Sullivan, L. C.; Daniels, C. B. *Development of the Pulmonary Surfactant System*; 2014.
- (56) McGowan, S. E. The Formation of Pulmonary Alveoli. In *The Lung: Development, Aging and the Environment: Second Edition*; 2014; pp 65–84.
- (57) Postle, A. D.; Heeley, E. L.; Wilton, D. C. A Comparison of the Molecular Species Compositions of Mammalian Lung Surfactant Phospholipids. In *Comparative Biochemistry and Physiology - A Molecular and Integrative Physiology*; 2001; Vol. 129, pp 65–73.
- (58) Karnati, S.; Garikapati, V.; Liebisch, G.; Van Veldhoven, P. P.; Spengler, B.; Schmitz, G.; Baumgart-Vogt, E. Quantitative Lipidomic Analysis of Mouse Lung during Postnatal Development by Electrospray Ionization Tandem Mass Spectrometry. *PLoS One* **2018**, *13* (9), e0203464.
- (59) Bodzon-Kulakowska, A.; Suder, P. Imaging Mass Spectrometry: Instrumentation, Applications, and Combination with Other Visualization Techniques. *Mass Spectrom. Rev.* **2016**, *35* (1), 147–169.
- (60) Lanekoff, I.; Stevens, S. L.; Stenzel-Poore, M. P.; Laskin, J. Matrix Effects in Biological Mass Spectrometry Imaging: Identification and Compensation. *Analyst* **2014**, *139* (14), 3528.
- (61) Amstalden van Hove, E. R.; Smith, D. F.; Heeren, R. M. A. A Concise Review of Mass Spectrometry Imaging. *J. Chromatogr. A* **2010**, *1217* (25), 3946–3954.
- (62) Pól, J.; Strohalm, M.; Havlíček, V.; Volný, M. Molecular Mass Spectrometry Imaging in Biomedical and Life Science Research. *Histochemistry and Cell Biology*. 2010, pp 423–443.

- (63) Spengler, B. Mass Spectrometry Imaging of Biomolecular Information. *Analytical Chemistry*. 2015, pp 64–82.
- (64) Wu, C.; Dill, A.; Eberlin, L.; Cooks, R.; Ifa, D. Mass Spectrometry Imaging under Ambient Conditions. *Mass Spectrom. Rev.* **2013**, *32* (12), 218–243.
- (65) Li, L.-H.; Hsieh, H.-Y.; Hsu, C.-C. Clinical Application of Ambient Ionization Mass Spectrometry. *Mass Spectrom. (Tokyo, Japan)* **2017**, *6* (Spec Iss), S0060.
- (66) Addie, R. D.; Balluff, B.; Bovée, J. V. M. G.; Morreau, H.; McDonnell, L. A. Current State and Future Challenges of Mass Spectrometry Imaging for Clinical Research. *Anal. Chem.* **2015**, *87* (13), 6426–6433.
- (67) Lebedev, A. T. Ambient Ionization Mass Spectrometry. *Russ. Chem. Rev.* **2015**, *84* (7), 665–692.
- (68) Lanekoff, I.; Heath, B. S.; Liyu, A.; Thomas, M.; Carson, J. P.; Laskin, J. Automated Platform for High-Resolution Tissue Imaging Using Nanospray Desorption Electrospray Ionization Mass Spectrometry. *Anal. Chem.* **2012**, *84* (19), 8351–8356.
- (69) Nguyen, S. N.; Kyle, J. E.; Dautel, S. E.; Sontag, R.; Luders, T.; Corley, R.; Ansong, C.; Carson, J.; Laskin, J. Lipid Coverage in Nanospray Desorption Electrospray Ionization Mass Spectrometry Imaging of Mouse Lung Tissues. *Anal. Chem.* **2019**, *91* (18), 11629–11635.
- (70) Nakayasu, E. S.; Nicora, C. D.; Sims, A. C.; Burnum-Johnson, K. E.; Kim, Y.-M.; Kyle, J. E.; Matzke, M. M.; Shukla, A. K.; Chu, R. K.; Schepmoes, A. A.; et al. MPLEx: A Robust and Universal Protocol for Single-Sample Integrative Proteomic, Metabolomic, and Lipidomic Analyses. *mSystems* **2016**, *1* (3).
- (71) Berry, K. A. Z.; Li, B.; Reynolds, S. D.; Barkley, R. M.; Gijón, M. A.; Hankin, J. A.; Henson, P. M.; Murphy, R. C. MALDI Imaging MS of Phospholipids in the Mouse Lung. *J. Lipid Res.* **2011**, *52* (8), 1551–1560.
- (72) Dennis, E. A. *Handbook of Cell Signaling*; Elsevier, 2003.
- (73) Eichmann, T. O.; Lass, A. DAG Tales: The Multiple Faces of Diacylglycerol—Stereochemistry, Metabolism, and Signaling. *Cell. Mol. Life Sci.* **2015**, *72* (20), 3931–3952.
- (74) Weinberger, B.; Hirsch, D.; Yin, K.; Spur, B. W. Chapter 21 – Lipid Mediators and Lung Function. In *Comparative Biology of the Normal Lung*; 2015; pp 403–421.
- (75) Lundström, S. L.; Balgoma, D.; Wheelock, Å. M.; Haeggström, J. Z.; Dahlén, S.-E.; Wheelock, C. E. Lipid Mediator Profiling in Pulmonary Disease. *Curr. Pharm. Biotechnol.* **2011**, *12* (7), 1026–1052.

- (76) Stierlin, H.; Faigle, J. W.; Sallmann, A.; Kung, W.; Richter, W. J.; Kriemler, H.-P.; Alt, K. O.; Winkler, T. Biotransformation of Diclofenac Sodium (Voltaren®) in Animals and in Man. *Xenobiotica* **1979**, *9* (10), 601–610.
- (77) Kenny, J. R.; Maggs, J. L.; Meng, X.; Sinnott, D.; Clarke, S. E.; Park, B. K.; Stachulski, A. V. Syntheses and Characterization of the Acyl Glucuronide and Hydroxy Metabolites of Diclofenac. *J. Med. Chem.* **2004**, *47* (11), 2816–2825.
- (78) Daly, A. K.; Aithal, G. P.; Leathart, J. B. S.; Swainsbury, R. A.; Dang, T. S.; Day, C. P. Genetic Susceptibility to Diclofenac-Induced Hepatotoxicity: Contribution of UGT2B7, CYP2C8, and ABCC2 Genotypes. *Gastroenterology* **2007**, *132* (1), 272–281.
- (79) Sparidans, R. W.; Lagas, J. S.; Schinkel, A. H.; Schellens, J. H. M.; Beijnen, J. H. Liquid Chromatography–Tandem Mass Spectrometric Assay for Diclofenac and Three Primary Metabolites in Mouse Plasma. *J. Chromatogr. B* **2008**, *872* (1–2), 77–82.
- (80) Liang, Z.; Zhang, Z.; Wolff, J. J.; Thompson, C. J.; Zhong, W. Implementation of Electron-Induced Dissociation Mass Spectrometry Technique for Differentiation of Isomeric Metabolites of Diclofenac. *Rapid Commun. Mass Spectrom.* **2017**, *31* (17), 1471–1475.
- (81) Schweitzer, A.; Hasler-Nguyen, N.; Zijlstra, J. Preferential Uptake of the Non Steroid Anti-Inflammatory Drug Diclofenac into Inflamed Tissues after a Single Oral Dose in Rats. *BMC Pharmacol.* **2009**, *9* (1), 5.
- (82) Sarda, S.; Page, C.; Pickup, K.; Schulz-Utermoehl, T.; Wilson, I. Diclofenac Metabolism in the Mouse: Novel in Vivo Metabolites Identified by High Performance Liquid Chromatography Coupled to Linear Ion Trap Mass Spectrometry. *Xenobiotica* **2012**, *42* (2), 179–194.
- (83) Shen, S.; Marchick, M. R.; Davis, M. R.; Doss, G. A.; Pohl, L. R. Metabolic Activation of Diclofenac by Human Cytochrome P450 3A4: Role of 5-Hydroxydiclofenac. *Chem. Res. Toxicol.* **1999**, *12* (2), 214–222.
- (84) Thorne, C. Diclofenac Pathway, Pharmacokinetics <https://www.pharmgkb.org/pathway/PA166163705> (accessed Oct 10, 2019).
- (85) Whirl-Carrillo, M.; McDonagh, E. M.; Hebert, J. M.; Gong, L.; Sangkuhl, K.; Thorn, C. F.; Altman, R. B.; Klein, T. E. Pharmacogenomics Knowledge for Personalized Medicine. *Clin. Pharmacol. Ther.* **2012**, *92* (4), 414–417.
- (86) Bort, R.; Macé, K.; Boobis, A.; Gómez-Lechón, M.-J.; Pfeifer, A.; Castell, J. Hepatic Metabolism of Diclofenac: Role of Human CYP in the Minor Oxidative Pathways. *Biochem. Pharmacol.* **1999**, *58* (5), 787–796.

- (87) Niyonsaba, E.; Easton, M. W.; Feng, E.; Yu, Z.; Zhang, Z.; Sheng, H.; Kong, J.; Easterling, L. F.; Milton, J.; Chobanian, H. R.; et al. Differentiation of Deprotonated Acyl-, N -, and O -Glucuronide Drug Metabolites by Using Tandem Mass Spectrometry Based on Gas-Phase Ion–Molecule Reactions Followed by Collision-Activated Dissociation. *Anal. Chem.* **2019**, *91* (17), 11388–11396.
- (88) Anders, M. W. Metabolism of Drugs by the Kidney. *Kidney Int.* **1980**, *18* (5), 636–647.
- (89) Vaz, A. D. N.; Wang, W. W.; Bessire, A. J.; Sharma, R.; Hagen, A. E. A Rapid and Specific Derivatization Procedure to Identify Acyl-Glucuronides by Mass Spectrometry. *Rapid Commun. Mass Spectrom.* **2010**, *24* (14), 2109–2121.
- (90) Alam, M. A.; Al-Jenoobi, F. I.; Al-Mohizea, A. M. High-Throughput Ultra-Performance LC-MS-MS Method for Analysis of Diclofenac Sodium in Rabbit Plasma. *J. Chromatogr. Sci.* **2015**, *53* (1), 47–53.
- (91) Zhang, Y.; Han, Y.-H.; Putluru, S. P.; Matta, M. K.; Kole, P.; Mandlekar, S.; Furlong, M. T.; Liu, T.; Iyer, R. A.; Marathe, P.; et al. Diclofenac and Its Acyl Glucuronide: Determination of In Vivo Exposure in Human Subjects and Characterization as Human Drug Transporter Substrates In Vitro. *Drug Metab. Dispos.* **2016**, *44* (3), 320–328.
- (92) Dorado, P.; Berecz, R.; Cáceres, M. C.; LLerena, A. Analysis of Diclofenac and Its Metabolites by High-Performance Liquid Chromatography: Relevance of CYP2C9 Genotypes in Diclofenac Urinary Metabolic Ratios. *J. Chromatogr. B* **2003**, *789* (2), 437–442.
- (93) Keski-Hynnälä, H.; Luukkanen, L.; Taskinen, J.; Kostianen, R. Mass Spectrometric and Tandem Mass Spectrometric Behavior of Nitrocatechol Glucuronides: A Comparison of Atmospheric Pressure Chemical Ionization and Electrospray Ionization. *J. Am. Soc. Mass Spectrom.* **1999**, *10* (6), 537–545.
- (94) Drexler, D. M.; Tannehill-Gregg, S. H.; Wang, L.; Brock, B. J. Utility of Quantitative Whole-Body Autoradiography (QWBA) and Imaging Mass Spectrometry (IMS) by Matrix-Assisted Laser Desorption/Ionization (MALDI) in the Assessment of Ocular Distribution of Drugs. *J. Pharmacol. Toxicol. Methods* **2011**, *63* (2), 205–208.
- (95) Solon, E. G. Autoradiography Techniques and Quantification of Drug Distribution. *Cell Tissue Res.* **2015**, *360* (1), 87–107.
- (96) Solon, E. G.; Schweitzer, A.; Stoeckli, M.; Prideaux, B. Autoradiography, MALDI-MS, and SIMS-MS Imaging in Pharmaceutical Discovery and Development. *AAPS J.* **2010**, *12* (1), 11–26.
- (97) Solon, E. G.; Kraus, L. Quantitative Whole-Body Autoradiography in the Pharmaceutical Industry. *J. Pharmacol. Toxicol. Methods* **2001**, *46* (2), 73–81.

- (98) Kertesz, V.; Van Berkel, G. J.; Vavrek, M.; Koeplinger, K. A.; Schneider, B. B.; Covey, T. R. Comparison of Drug Distribution Images from Whole-Body Thin Tissue Sections Obtained Using Desorption Electrospray Ionization Tandem Mass Spectrometry and Autoradiography. *Anal. Chem.* **2008**, *80* (13), 5168–5177.
- (99) Norris, J. L.; Caprioli, R. M. Analysis of Tissue Specimens by Matrix-Assisted Laser Desorption/Ionization Imaging Mass Spectrometry in Biological and Clinical Research. *Chem. Rev.* **2013**, *113* (4), 2309–2342.
- (100) Greer, T.; Sturm, R.; Li, L. Mass Spectrometry Imaging for Drugs and Metabolites. *J. Proteomics* **2011**, *74* (12), 2617–2631.
- (101) Prideaux, B.; Lenaerts, A.; Dartois, V. Imaging and Spatially Resolved Quantification of Drug Distribution in Tissues by Mass Spectrometry. *Curr. Opin. Chem. Biol.* **2018**, *44*, 93–100.
- (102) Schulz, S.; Becker, M.; Groseclose, M. R.; Schadt, S.; Hopf, C. Advanced MALDI Mass Spectrometry Imaging in Pharmaceutical Research and Drug Development. *Curr. Opin. Biotechnol.* **2019**, *55*, 51–59.
- (103) Karlsson, O.; Hanrieder, J. Imaging Mass Spectrometry in Drug Development and Toxicology. *Arch. Toxicol.* **2017**, *91* (6), 2283–2294.
- (104) Buchberger, A. R.; DeLaney, K.; Johnson, J.; Li, L. Mass Spectrometry Imaging: A Review of Emerging Advancements and Future Insights. *Anal. Chem.* **2018**, *90* (1), 240–265.
- (105) Cornett, D. S.; Reyzer, M. L.; Chaurand, P.; Caprioli, R. M. MALDI Imaging Mass Spectrometry: Molecular Snapshots of Biochemical Systems. *Nat. Methods* **2007**, *4* (10), 828–833.
- (106) Sugiura, Y.; Setou, M. Imaging Mass Spectrometry for Visualization of Drug and Endogenous Metabolite Distribution: Toward In Situ Pharmacometabolomes. *J. Neuroimmune Pharmacol.* **2010**, *5* (1), 31–43.
- (107) Cornett, D. S.; Frappier, S. L.; Caprioli, R. M. MALDI-FTICR Imaging Mass Spectrometry of Drugs and Metabolites in Tissue. *Anal. Chem.* **2008**, *80* (14), 5648–5653.
- (108) Takyi-Williams, J.; Liu, C.-F.; Tang, K. Ambient Ionization MS for Bioanalysis: Recent Developments and Challenges. *Bioanalysis* **2015**, *7* (15), 1901–1923.
- (109) Castellino, S.; Groseclose, M. R.; Wagner, D. MALDI Imaging Mass Spectrometry: Bridging Biology and Chemistry in Drug Development. *Bioanalysis* **2011**, *3* (21), 2427–2441.
- (110) Swales, J. G.; Hamm, G.; Clench, M. R.; Goodwin, R. J. A. Mass Spectrometry Imaging and Its Application in Pharmaceutical Research and Development: A Concise Review. *Int. J. Mass Spectrom.* **2019**, *437*, 99–112.

- (111) Korfmacher, W.; Yagnik, G.; Luo, Y.; Ho, S.; Shen, L.; Wilper, T.; Norton, K.; Solon, E.; Liu, H.; Savage, S.; et al. *Comparison of LESA-MS to MALDI-MS for Mouse Whole Body Tissue Profiling: Diclofenac and Major Metabolites*; 2016.
- (112) Lanekoff, I.; Laskin, J. Imaging of Lipids and Metabolites Using Nanospray Desorption Electrospray Ionization Mass Spectrometry. In *Mass spectrometry imaging of small molecules: Methods in molecular biology*; Humana Press, 2015; pp 99–106.
- (113) Yin, R.; Kyle, J.; Burnum-Johnson, K.; Bloodsworth, K. J.; Sussel, L.; Ansong, C.; Laskin, J. High Spatial Resolution Imaging of Mouse Pancreatic Islets Using Nanospray Desorption Electrospray Ionization Mass Spectrometry. *Anal. Chem.* **2018**, *90* (11), 6548–6555.
- (114) Gaganis, P.; Miners, J. O.; Brennan, J. S.; Thomas, A.; Knights, K. M. Human Renal Cortical and Medullary UDP-Glucuronosyltransferases (UGTs): Immunohistochemical Localization of UGT2B7 and UGT1A Enzymes and Kinetic Characterization of S - Naproxen Glucuronidation. *J. Pharmacol. Exp. Ther.* **2007**, *323* (2), 422–430.
- (115) Margailan, G.; Rouleau, M.; Fallon, J. K.; Caron, P.; Villeneuve, L.; Turcotte, V.; Smith, P. C.; Joy, M. S.; Guillemette, C. Quantitative Profiling of Human Renal UDP-Glucuronosyltransferases and Glucuronidation Activity: A Comparison of Normal and Tumoral Kidney Tissues. *Drug Metab. Dispos.* **2015**, *43* (4), 611–619.
- (116) Knights, K. M.; Rowland, A.; Miners, J. O. Renal Drug Metabolism in Humans: The Potential for Drug-Endobiotic Interactions Involving Cytochrome P450 (CYP) and UDP-Glucuronosyltransferase (UGT). *Br. J. Clin. Pharmacol.* **2013**.
- (117) Zenser, T. V.; Mattammal, M. B.; Davis, B. B. Differential Distribution of the Mixed-Function Oxidase Activities in Rabbit Kidney. *J. Pharmacol. Exp. Ther.* **1978**.
- (118) Almazroo, O. A.; Miah, M. K.; Venkataramanan, R. Drug Metabolism in the Liver. *Clin. Liver Dis.* **2017**, *21* (1), 1–20.
- (119) Remmer, H. The Role of the Liver in Drug Metabolism. *Am. J. Med.* **1970**, *49* (5), 617–629.

VITA

EDUCATION

- Present Ph.D. Candidate, Analytical Chemistry, Purdue University, W. Lafayette, IN; Thesis Committee: Julia Laskin, Angeline Lyon, Hilikka Kenttämää
- 2014 B.S. Forensic Science, The University of Tampa, Tampa, FL

IMPORTANT SKILLS

- Vendor trained on multiple instruments: Thermo LTQ XL (linear quadrupole ion trap), Thermo Q Exactive HF-X (orbitrap), Agilent 6560 IM-QToF (ion mobility quadrupole time of flight)
- Instrument experience on Agilent 1260 Infinity II HPLC, Thermo Vanquish UHPLC, and Perkin Elmer Clarus 580 GC
- Experience with multiple ambient ionization techniques (nanoDESI, nanospray, DESI, DART, ESI)
- Sciex 4000QTrap instrument manager; instrument maintenance, troubleshooting and scheduling
- Inventory manager; order and keep track of incoming chemicals and solvents, schedule and oversee lab cleanup
- Strengths Finder: Empathy, Harmony, Relator, Adaptability, Input

RESEARCH EXPERIENCE

- Present Graduate Research with Dr. Julia Laskin; Utilization of Mass Spectrometry to Characterize, Image, and Quantify Small Molecules
- nanoDESI imaging of lipids, drugs and metabolites
 - operation and troubleshooting of Thermo Q Exactive HF-X and Agilent 6560 IM-QToF
 - collaborations with Merck & Co., Inc and LungMap Consortium
 - experience using imaging software: MSI Quickview (PNNL), Peak by Peak (Spectroswiss)
- 2017 Prep Lab Assistant with Jeanne Meyer

- redeveloped gas chromatography (GC) instrument methods for undergraduate organic labs
- 2014 Graduate Research with Dr. Yu Xia
 - determining double bond location in lipid samples with the Paternò-Büchi reaction
 - operation and troubleshooting of Sciex 4000QTrap
 - sample preparation techniques including lipid extraction protocols (Bligh Dyer, Folch, Bond Elut SPE, QuEChERS EMR-lipid)
- 2014 Summer Research with Dr. Julia Pearson
 - analysis of LSD-laced food samples for an investigative study following an unusual case report of LSD poisoning from the Tampa Police Department
- 2013 Undergraduate Research with Dr. Kenyon Evans-Nguyen
 - analysis of organic and inorganic compounds related to gunshot residue and radiological dispersive devices through ambient ionization techniques

TEACHING AND MENTORING EXPERIENCE

- 2018 Mentored REU undergraduate student, Harley Davidson (Summer 2018) – “Using IM-qTOF to find CCS of nicotine and nicotine related compounds in e-cigarette liquids”
- 2016-2017 General Chemistry Teaching Assistant (Spring 2016, Fall 2017); supervise lab experiments and mentor students, general chemistry for non-majors CHM 112 and engineering majors CHM 115
- 2017-present Chemistry tutor for undergraduate students
- 2015 Analytical Chemistry Lab Supervisor (Fall 2015); Supervise all TA lab sections, prepare reagents and materials for experiments, lead TA staff meetings
- 2014-2015 Analytical Chemistry Teaching Assistant (Fall 2014, Spring 2015); supervise lab experiments and mentor students
- 2014 Forensic Chemistry Lab Assistant (Fall 2014, Spring 2014); Setup GC, GC-MS and LC-MS instruments, supervise lab experiments and mentor students

2012 Analytical Chemistry Lab Assistant (Fall 2012); supervise lab experiments and mentor students

PUBLICATIONS AND PRESENTATIONS

Published Papers and Manuscripts

- 1) Brown, H., Chen, B., Vavrek, M., Cancilla, M., Pierson, E., Zhong, W., Laskin, J. Mass spectrometry imaging of diclofenac and its metabolites in tissues using nanospray desorption electrospray ionization. *In progress*.
- 2) Brown, H., Nguyen, S.N., Clair, G., Dautel, S.E., Sontag, R., Luders, T., Ansong, C., Carson, J., Laskin, J. Understanding lipid localization in the developing lung using nano-DESI mass spectrometry imaging. *In progress*.
- 3) Brown, H., Xia, Y. Utilizing the Paternò-Büchi reaction to analyze neutral lipids by Mass Spectrometry. *In progress*.
- 4) Wang, H., Lin, H., Zheng, Y., Ng, S., Brown, H., & Xia, Y. (2018). Kaolin-based catalyst as a triglyceride FCC upgrading catalyst with high deoxygenation, mild cracking, and low dehydrogenation performances. *Catalysis Today*. <https://doi.org/10.1016/j.cattod.2018.04.055>
- 5) Brown, H., Oktem, B., Windom, A., Doroshenko, V., & Evans-Nguyen, K. (2016). Direct analysis in real time (DART) and a portable mass spectrometer for rapid identification of common and designer drugs on-site. *Forensic Chemistry, 1*, 66-73. <https://doi.org/10.1016/j.forc.2016.07.002>
- 6) Evan-Nguyen, K. M., Gerling, J., Brown, H., Miranda, M., Windom, A., & Speer, J. (2016). Towards universal ambient ionization: Direct elemental analysis of solid substrates using microwave plasma ionization. *Analyst, 141*, 3811-3820. [doi:10.1039/c6an00176a](https://doi.org/10.1039/c6an00176a)
- 7) Evans-Nguyen, K. M., Quinto, A., Hargraves, T., Brown, H., Speer, J., & Glatter, D. (2013). Transmission Mode Desorption Electrospray Ionization (TM-DESI) for Simultaneous Analysis of Potential Inorganic and Organic Components of Radiological Dispersion Devices (RDDs). *Analytical Chemistry, 85*(24), 11826-11834. [doi:10.1021/ac402386m](https://doi.org/10.1021/ac402386m)

Research Presentations

- 1) “Quantitative mass spectrometry imaging of diclofenac and its metabolites in tissues using nanospray desorption electrospray ionization mass spectrometry” Poster presented at ASMS Annual Conference, Atlanta, GA (June 2019)
- 2) “Evaluation of nanoDESI system for quantitative mass spectrometry imaging and on tissue metabolite identification” Oral presentation at Merck Purdue Symposium, West Point, PA (November 2018)
- 3) “Understanding lipid localization in the developing lung using nano-DESI mass spectrometry imaging” Poster presented at ASMS Annual Conference, San Diego, CA (June 2018)
- 4) “Identification and quantitation of unsaturated glycerolipids from human plasma using the Paterno-Buchi reaction and tandem MS” Poster presented at ASMS Annual Conference, San Antonio, TX (June 2016)
- 5) “Utilization of photochemical reactions and tandem mass spectrometry to analyze neutral lipids” Poster presented at ASMS Annual Conference, St. Louis, MO (June 2015)
- 6) “An Unusual case of LSD poisoning” Poster presented at SOFT Annual Meeting, Grand Rapids, MI (Oct. 2014)
- 7) “A mass spectrometer for elemental analysis based on fieldable technologies” Poster presented at CNHS Undergraduate Research Symposium at the University of Tampa, Tampa, FL (April 2014)
- 8) “A mass spectrometer for elemental analysis based on fieldable technologies” Poster presented at IFRI Forensic Science Symposium at FIU, Miami, FL (April 2014)
- 9) “A mass spectrometer for elemental analysis based on fieldable technologies” Poster presented at Raymond N Castle Student Research Conference at USF, Tampa, FL (April 2014)
- 10) “A mass spectrometer for elemental analysis based on fieldable technologies” Poster presented at The University of Tampa Board of Trustees Poster Session, Tampa, FL (March 2014)
- 11) “A mass spectrometer for elemental analysis based on fieldable technologies” Poster presented at Pittcon, Chicago, IL (March 2014)

- 12) “Ambient ionization mass spectrometry for simultaneous analysis of organic and inorganic radiological dispersion device (RDD) components” Poster presented at DTRA Technical Review, Springfield, VA (July 2013)

HONORS AND AWARDS

- 2018 Women in Science Programs (WISP) travel grant recipient
2014 Raymond N. Castle Student Research Conference Undergraduate Poster Session Winner
2014 Outstanding Forensic Science Student
2010-2014 Presidential Scholarship

PROFESSIONAL MEMBERSHIPS, CLUBS, AND ORGANIZATIONS

- 2018-2019 Purdue Graduate Student Government (PGSG); Senator for the chemistry Department
2018-2019 Member of Life Team for PGSG; volunteer for organizing social events
2018-2019 Graduate Student Advisory Board; PGSG representative
2016-present Iota Sigma Pi (ISP) - Women in chemistry honors society; President (2018), Treasurer (2016), Member since 2016
2014-present Women in Science Programs (WISP); member since 2014
2014-present Member of the American Society for Mass Spectrometry
2010-2014 Criminology club; Secretary (2010-2013), Vice President (2013-2014)

VOLUNTEER AND COMMUNITY SERVICE

- 2018 Big Ten Graduate School Exposition (September); Chemistry department tour guide and graduate student representative at Q&A session for undergraduate students interested in pursuing graduate school
2018 Organized and coordinated help session for younger graduate students working on their original proposals (August); Professors and upper level graduate students provide tips and answer questions about the process
2018 Judge for the College of Science at the Purdue Undergraduate Research Conference (April)
2018 Volunteer at Columbian Park Zoo for the Big Grad Event (March); Spring break volunteer event hosted by Purdue graduate school to help local non-profit organizations

- 2017 Chemistry department tour guide for Next Generation Scholars (November);
Outreach event for Purdue students to introduce local youth to research opportunities
- 2016-2019 Girl Scout Day (April); science demonstrations for girl scouts to earn science badge
- 2015-2018 Purdue graduate recruitment poster session (March); Share research with incoming chemistry graduate students who have applied to Purdue
- 2014-2018 ACS National Chemistry Week (October); Volunteer to lead science experiments in multiple classrooms at local elementary schools